

Politecnico di Torino

Corso di Laurea Magistrale in Ingegneria Energetica e Nucleare

Tesi di Laurea Magistrale

A Harmonic Balance simulation framework for the ISWEC wave energy device



Relatori

Prof. Giuliana Mattiazzo

Prof. John Ringwood

Dott. Giovanni Bracco

Dott. Alexis Méri­gaud

Candidato

Riccardo Novo

Aprile 2018

- Vous aimez la mer, capitaine?

*- Oui ! Je l'aime ! La mer est tout ! Elle couvre les sept dixièmes du globe terrestre. Son souffle est pur et sain.
C'est l'immense désert où l'homme n'est jamais seul, car il sent frémir la vie à ses côtés. [...]*

Jules Verne, 'Vingt mille lieues sous les mers'

Acknowledgements

I would like to thank Professor John Ringwood for having hosted me at the Centre for Ocean Energy Research, for the valuable discussions and the careful supervision; the PhD student Alexis Mérigaud for having guided me step by step through the project and for the work we did, as well as for great the moments spent together; Giuseppe Giorgi for his helpful tips and explanations and his really precious friendship; Christian Windt and Nicolás Faedo for their scientific and moral support along the research work; all the people from the COER group for their friendliness and for the great experience I had in Maynooth. I am grateful to Professor Giuliana Mattiazzo, Doctor Giovanni Bracco and Antonello Sirigu for the opportunity they've given me and for the support I've received from them.

I would also like to thank my parents for their affection and for having endlessly upheld me, as well as my whole family; the Gleeson Watts family for their warm welcome; all the friends and the people met over these exciting and challenging last five years.

Abstract

The early phase of development of wave energy technology and its relatively high installation costs imply the need to study computationally-efficient simulation methods for Wave Energy Converters (WECs). There are several different methods for this purpose, each with its own advantages and peculiarities; the task becomes particularly challenging when the WEC model presents non-linearities. Harmonic Balance (HB) uses the Fourier projection of the model inputs and variables and solves for the steady-state motion of a non-linear system, ensuring an appropriate description of the non-linear effects. In previous works, HB has been applied to WECs with one degree of freedom (DoF). Here the same approach is introduced and extended to multi-DoF systems. Then, the 2-DoF model of the ISWEC wave energy device is used as a case study.

The research work presented here begins with a framing of the resources and technology related to wave energy and of the available methods for WECs simulation. The ISWEC device is then studied, with a particular glance at its 2-DoF physical model. HB is presented for one and multi-DoF WECs, and then applied to the ISWEC model. A validation of the developed simulation framework is performed over a wide range of regular and irregular sea conditions, proving the suitability of the HB approach to multi-DoF WECs. All the issues faced during the research work are addressed, from the sensitivity to the starting point of the HB algorithm to the non-convergence of the method for some particular conditions, such as the most energetic sea-states.

Contents	iii
Introduction	1
1 Wave energy: resource and technology	3
1.1 An overview on the wave energy resource	3
1.1.1 Principles of linear wave theory	4
1.1.2 Sea states description	10
1.1.3 Global wave energy potential	18
1.2 Wave Energy Converters	20
1.2.1 Historical notes and technology policies	20
1.2.2 State of the art	24
1.2.3 Numerical modelling of WECs	28
2 ISWEC - Inertial Sea Wave Energy Converter	34
2.1 Structure and working principle	34
2.2 The ISWEC project: goals and timeline	36
2.3 Reference frames	37
2.4 Gyroscope mathematical model	38
2.4.1 Physical equations for the gyroscope	39
2.4.2 Gyroscope equations in hull reference frame	40
2.4.3 Gyroscope supporting frame	41
2.4.4 Equations simplification	42
2.4.5 Linearisation	44
2.5 Hydrodynamical model	44
2.5.1 Assumptions and hydrodynamic actions	45
2.5.2 Frequency-domain equation	45
2.5.3 Time-domain equation	48
2.5.4 Viscous terms	49

2.6	PTO model and constraints	50
2.7	Pitch DoF model	51
2.8	Simulation frameworks	52
2.8.1	Frequency-domain: ISWEC design tool	52
2.8.2	Time-domain: the Simulink model	52
2.8.3	Time-domain: Runge-Kutta 2	54
3	Harmonic balance simulation framework	57
3.1	The HB method for 1-DoF WECs	58
3.1.1	Dynamical equations	58
3.1.2	The HB approach	59
3.1.3	The solution algorithm	62
3.2	From one to multiple DoF	65
3.2.1	Dynamical equations for multi-DoF WECs	65
3.2.2	The HB approach for multi-DoF WECs	66
3.3	HB implementation of the ISWEC model	69
3.3.1	Formulation of the simulation framework	69
3.3.2	Practical issues	71
4	Numerical results and validation	74
4.1	Regular waves	74
4.1.1	Sea conditions and control parameters	74
4.1.2	Required number of harmonics: convergence study	76
4.1.3	Validation results	76
4.1.4	Sensitivity to the algorithm starting point and multiple solutions	79
4.2	Irregular waves	81
4.2.1	Sea conditions and control parameters	81
4.2.2	Required number of harmonics: convergence study	81
4.2.3	Validation results	81
4.2.4	Algorithm convergence: ongoing issues and possible solutions	84
5	Conclusions	86
5.1	Pros and cons of the HB approach	86
5.2	Opportunities and recommendation for future research	87
	Bibliography	88

Research background and motivation

Harvesting large amounts of energy from different and sustainable sources is one of the major challenges facing human society in the 21st century. Newly industrialised countries will increasingly make use of large-scale electricity generation, and they need to be supported in order to make their growth sustainable from an environmental, as well as economic point of view. The world population is expected to be 29% higher in 2050 than in 2017, and this will contribute to the increased demand for energy, as well as food and raw materials [United Nations, 2017]. Although it is difficult to make accurate estimates, the World Energy Outlook 2017 forecasts a 60% increase of electricity demand up to 2040, due both to the increasing demand of primary energy and the progresses in the electrification process [IEA, 2017].

At the same time, the vast majority of the world's countries signed the Paris Agreement in 2015 to hold, quoting [United Nations, 2015], *"the increase in the global average temperature to well below 2°C above pre-industrial levels"*. This requires a great and immediate effort by the signatory parties to the agreement. As a virtuous example of declaration of intent, the low-carbon economy roadmap of the European Union aims at reaching an 80% cut of greenhouse gas emission with respect to 1990 levels by 2050 [European Commission, 2011].

All the above reasons lead public entities and private companies to invest in a sustainable and differentiated mix of energy sources. This involves the improvement of existing technologies, in order to reach the highest levels of efficiency, and the development of technologies able to harvest energy from those renewable sources which have not yet been adequately exploited. Oceans and seas cover over 70% of the Earth's surface, representing a considerable and not yet exploited source of renewable energy. Ocean energy can be divided into six domains depending on its origin: tidal range, tidal current, ocean current, ocean wave, ocean thermal energy, salinity gradient [Uihlein and Magagna, 2016]. In addition, offshore wind should also be mentioned among marine energy sources, although it does not capture energy directly from the force of the sea. It represents one of the energy sectors having the highest development rates in Europe: in 2016 investments on offshore wind farms amounted to €18.2bn [Wind Europe, 2017].

Tidal range technology is considered mature, while ocean wave and tidal current energy represent the most advanced and promising fields of study [Edenhofer et al., 2011]. Many different universities and research centres all around the world are working in particular on the great potential of wave energy and the technology to exploit it. The resource is characterized by complicated theoretical aspects and a great variability, while the technical challenges are many and often shared with other marine engineering sectors. Wave energy has been in the political spotlight since 1991, when the European Commission chose to include wave energy in the R&D program on renewable energies [Falcão, 2010]. Later in the years, large public and private investments have been made in North America and Asia.

WECs are often characterised by a pretty high number of control parameters, if compared to traditional renewable energy harvesting technologies. Furthermore, because of the characteristics of their operating environment, the installation costs of WECs are relatively high. It is therefore essential to be able to rely on tools that allow accurate and computationally efficient simulation of their operation. Numerical simulations applications are multiple, from the optimization of the control parameters to the power assessment in different locations: they are a core-business in the wave energy field.

This thesis, and the work behind it, are positioned in the above-mentioned context. The need to build efficient numerical models for WECs has prompted the author and his colleagues to apply an existing innovative method for WECs simulation, named Harmonic Balance, to one of the most promising devices on the Italian scene, the ISWEC (Inertial Sea Wave Energy Converter).

Structure of the thesis

This research master's thesis starts with a description of the wave energy resource from a qualitative and quantitative point of view. Chapter 1 also gives an overview of the state of the art of the technology, and of the different methods available for the simulation of WECs. Chapter 2 concerns the ISWEC device, and it starts with an in-depth analysis of its internal gyroscopic system. Then, the hydrodynamic interaction is examined, as well as the PTO model. The overall pitch DoF physical model is proposed, trying to highlight the main simplifications introduced. The final section is devoted to a presentation of the available simulation frameworks for the device. Chapter 3 represents the core of research work: the HB approach is first presented for a 1-DoF general case, and then extended to a multi-DoF general case. Successively the HB simulation framework for the pitch DoF ISWEC model is developed, with a precise identification of all the matrices used. Chapter 4 presents the numerical results. A convergence study for the choice of the number of harmonics to be used in the Fourier basis is performed in both regular and irregular waves; a complete validation on a classical time-domain model is performed to prove the accuracy of the results. Also, the main issues encountered are addressed, with the suggestion of possible solutions to overcome them. Finally, Chapter 5 contains the conclusions of the whole thesis. The results obtained are recalled trying to give a wider view; then, some ideas and suggestions for future works are given.

Wave energy: resource and technology

The first chapter starts with a broad look at the main aspects of wave energy. The resource is briefly described from a qualitative point of view, then some basic math is introduced in order to understand the main parameters for its quantitative description. The second part of the chapter will glance at the state of the art of the technology, reporting a classification of the existing devices based on their operating principles. The last section concerns more in detail the numerical modelling of WECs.

1.1 An overview on the wave energy resource

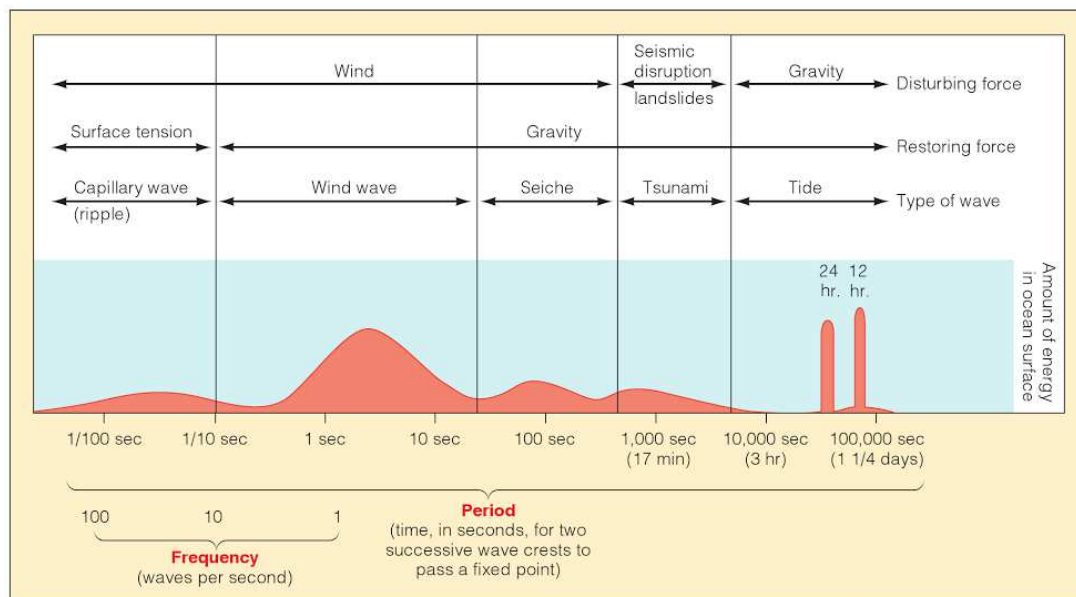
Ocean surface waves are caused by the presence of numerous forces acting on the ocean, first and foremost that exerted by the atmosphere pressure through the winds. Other natural forces affecting the phenomenon are gravity, surface tension, earthquakes, gravitational attraction (interaction of the ocean water mass with Moon and Sun), the Coriolis force and surface tension [WMO, 1998].

Ocean waves are formed by a disturbing force and reduced by a restoring force: while the restoring force is ever present and returns water to flatness, the disturbing force is applied for a finite time interval; oscillations around the resting point are caused by the overcompensation given by the restoring force [Garrison, 2015]. Classification of ocean waves, as well as on disturbing and restoring force, is based on their wavelength, i.e. the horizontal distance between two successive crests (see Table 1.1). The restoring force for waves with wavelength greater than 1.73 cm is gravity: sea waves are able to propagate for thousand of kilometres as the circular trajectory of water particles in waves is almost frictionless. An interesting piece of data is given, qualitatively, in Fig. 1.1. Waves are here reported according to their period, i.e. the time interval between the passage at the same point of consecutive crests; it is evident how wind waves contain a far greater amount of energy with respect to all the other types. Looking more in detail at how wind waves are generated, we can say that their size depends on mainly three variables [Leyva, 2000]:

- Fetch: the area over which wind blows.
- Wind speed: the simplest marker of wind force.

Table 1.1: Disturbing forces, wavelength and restoring forces for ocean waves [Garrison, 2015].

Wave type	Disturbing force	Restoring force	Typical wavelength
Capillary wave	Usually wind	Cohesion of water molecules	Up to 1.72 cm
Wind wave	Wind over ocean	Gravity	60-150 m
Seiche	Change in atmospheric pressure, storm surge, tsunami	Gravity	Large, variable: a function of ocean basin size
Seismic sea wave (tsunami)	Faulting of seafloor, volcanic eruption, landslide	Gravity	200 km
Tide	Gravitational attraction, rotation of Earth	Gravity	Half Earth's circumference

**Figure 1.1:** Wave energy in the ocean as a function of the wave period [Garrison, 2015].

- Duration: the time period for which wind blows.

Energy is transferred from air to water as wind blows in the centre of the ocean: starting from ripples, a storm wave is generated. It can continue growing for long distances (length of fetch), giving rise to swell waves: these waves are the ones that propagate out of their region of generation (See Fig. 1.2). The topography of the seabed can determine the dispersion of the energy of waves. We're mostly interested in swell waves, those most likely to be encountered on the surface of the sea; however, wave dynamics involves a high number of factors and variables. For the purposes of this research, we will limit to report the principles of the *linear wave theory* published by Airy in the first part of the 19th century [Airy, 1841]: they are the bases on which the formulas used for the wave modelling and the wave-body interaction description are built.

1.1.1 Principles of linear wave theory

Linear wave theory owes its relative simplicity to the strict validity domain on which it can be applied, representing, however, an approximation of reality sufficient for many applications. Its assumptions are reported as follows [USACE, 2002]:

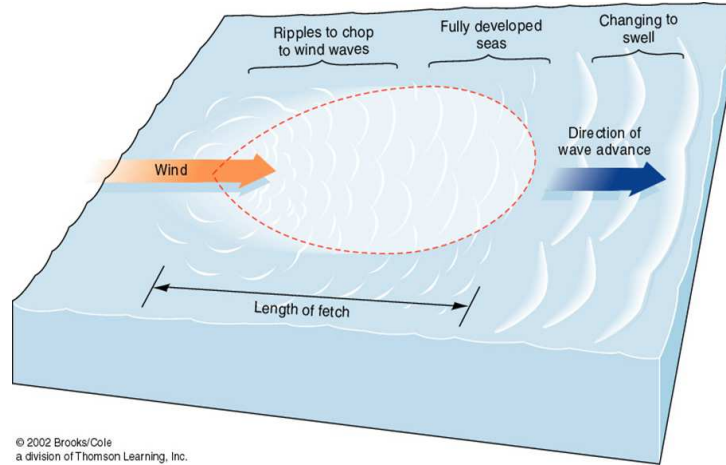


Figure 1.2: Wind blows over the sea over the length of fetch, generating a storm wave. Swell waves propagate then out of the fetch area [Raffero, 2014].

- (i) Waves are plane, i.e. their wavefronts are infinite parallel planes.
- (ii) The wave amplitude is small with respect to its wavelength, and its waveform is time-invariant and space-invariant.
- (iii) The fluid is homogeneous and incompressible.
- (iv) The fluid is inviscid and irrotational.
- (v) Surface tension can be neglected.
- (vi) Coriolis effect can be neglected.
- (vii) The sea bed is horizontal, motionless and impermeable.
- (viii) Fluid particles on the wave surface remain on the surface during all the wave motion.
- (ix) Pressure at the free surface is uniform and constant (i.e. we're considering a swell wave, as wind is not blowing over the sea surface).

The following mathematical treatment was taken over and elaborated from [Krogstad and Arntsen, 2000]. Let's consider waves in a channel with parallel walls and an horizontal seabed (assumptions (i) and (ii)), as the one reported in Fig. 1.3. At each point (x, z) the fluid has a velocity:

$$\mathbf{v}(x, z, t) = u(x, z, t)\mathbf{i} + w(x, z, t)\mathbf{k} \quad (1.1.1)$$

where t is time from an arbitrary instant, x is the horizontal coordinate from an arbitrary point, z is the vertical coordinate upwards from the resting water level. The two vectors \mathbf{i} and \mathbf{k} are the unit vectors, respectively, on the x -axis and the z -axis, while u and w are the velocity components on the same axes. For the assumption (iii) we'll have that velocity $\mathbf{v} = (u, w)$ satisfies the *continuity equation*:

$$\frac{\partial u}{\partial x} + \frac{\partial w}{\partial z} = 0 \quad (1.1.2)$$

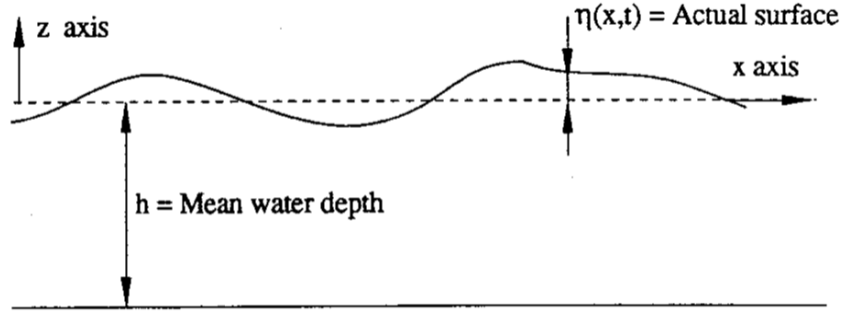


Figure 1.3: Waves along a channel [Krogstad and Arntsen, 2000].

Furthermore, because of assumption (iv), we can describe the velocity field as the gradient of a scalar function, the *velocity potential* Φ :

$$u = \frac{\partial \Phi}{\partial x}, w = \frac{\partial \Phi}{\partial z} \quad (1.1.3)$$

Using the last equation in Eq. (1.1.1), we obtain:

$$\frac{\partial^2 \Phi}{\partial x^2} + \frac{\partial^2 \Phi}{\partial z^2} = 0 \quad (1.1.4)$$

The above equation, called *Laplace equation*, describes completely the water motion. In order to search for its solutions, it is necessary to discuss the boundary conditions of the problem.

Because of assumption (vii) the velocity at the bottom ($z = -h$) must be null at all times:

$$w(x, z = -h, t) = \frac{\partial \Phi}{\partial z}(x, z = -h, t) = 0 \quad (1.1.5)$$

We still need two boundary conditions for the solution of Eq. (1.1.4): they'll be the ones at the free surface from assumption (viii) and (ix). The first one states an experimental observation: the particles of fluid on the surface tend to stay on the surface during all the wave motion. The mathematical implementation of this boundary condition is not very straightforward. Let's consider the surface at two close instants, t_1 and t_2 . Identifying $\eta(x, t) = z$, we'll have that in the time interval $\Delta t = t_2 - t_1$ the fluid particle in $(x_1, \eta(x_1, t_1))$ moves with velocity \mathbf{v} to the point $(x_2, \eta(x_2, t_2))$, as shown in Fig. 1.4. Thus, the two space variables identifying the second point can be expressed as:

$$x_2 = x_1 + u(t_2 - t_1) \quad (1.1.6)$$

$$\eta(x_2, t_2) = \eta(x_1, t_1) + w(t_2 - t_1) \quad (1.1.7)$$

Expanding $\eta(x_2, t_2)$ in Taylor series, we obtain:

$$\eta(x_2, t_2) = \eta(x_1, t_2) + \frac{\partial \eta}{\partial x}(x_1, t_2)(x_2 - x_1) + \dots \quad (1.1.8)$$

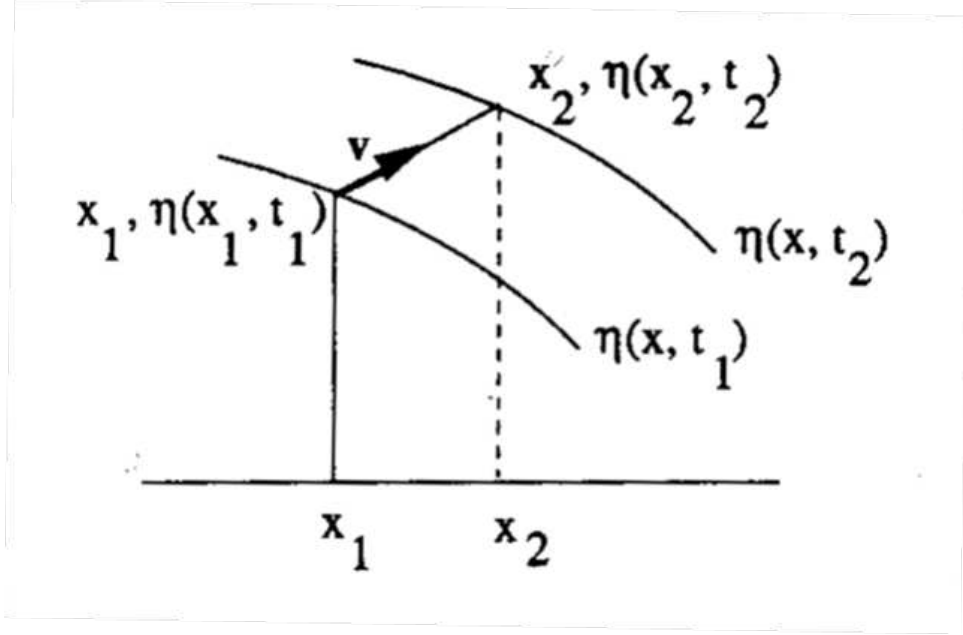


Figure 1.4: Motion of a fluid particle on the free surface [Krogstad and Arntsen, 2000].

Introducing the above equation in Eq. (1.1.7), we obtain:

$$\eta(x_1, t_2) - \eta(x_1, t_1) + \frac{\partial \eta}{\partial x}(x_1, t_2)(x_2 - x_1) = w(t_2 - t_1) \quad (1.1.9)$$

Dividing both the terms by $(t_2 - t_1)$ and letting $t_2 \rightarrow t_1$:

$$\frac{\partial \eta}{\partial t} + u \frac{\partial \eta}{\partial x} = w \quad (1.1.10)$$

that represents the *kinematic boundary condition*. The second boundary condition at the free surface comes from assumption (ix) and is derived through the *Boernoulli's equation*, valid for irrotational flows:

$$\frac{p}{\rho} + \frac{\partial \Phi}{\partial t} + \frac{1}{2}(u^2 + w^2) + gz = C(t) \quad (1.1.11)$$

where p is the pressure in the fluid at the given point, ρ is the fluid density (constant for assumption (iii)), g is the gravity acceleration. $C(t)$ is a function that can be set to any arbitrary constant; fixing $C(t) = \frac{p_{atm}}{\rho}$, the Bernoulli's equation for the points on the free surface will be:

$$\frac{\partial \Phi}{\partial t} + \frac{1}{2}(u^2 + v^2) + g\eta = 0 \quad (1.1.12)$$

This condition is called *dynamic boundary condition* as it deals with the force exerted on the fluid surface.

Our problem is now completely defined, and it can be summarised as follows:

1. Laplace equation must be satisfied within all the fluid:

$$\frac{\partial^2 \Phi}{\partial x^2} + \frac{\partial^2 \Phi}{\partial z^2} = 0 \quad (1.1.13)$$

2. At the bottom of the channel the fluid must have zero velocity:

$$w(x, z = -h, t) = \frac{\partial \Phi}{\partial z}(x, z = -h, t) = 0 \quad (1.1.14)$$

3. The particles on the surface do not move inwardly into the flow, and vice versa (*kinematic boundary condition*):

$$\frac{\partial \eta}{\partial t} + u \frac{\partial \eta}{\partial x} = w \quad (1.1.15)$$

4. The pressure at the three surface is constant and uniform, and it is equal to the atmospheric one (*dynamic boundary condition*):

$$\frac{\partial \Phi}{\partial t} + \frac{1}{2}(u^2 + w^2) + g\eta = 0 \quad (1.1.16)$$

The problem identified by Eqs. (1.1.13) to (1.1.15) is complicated and a general solution is not known. However, making use of assumption (ii), we can move in a special case with a relatively simple solution. Indeed, because of the small amplitude assumption, we can simplify some of the above conditions; for the mathematical steps please refer directly to [Krogstad and Arntsen, 2000], while the result of simplifications is reported as follows. In Eq. (1.1.15) the term $u \frac{\partial \eta}{\partial x}$ is much smaller than $\frac{\partial \eta}{\partial t}$, thus the *kinematic boundary condition* becomes:

$$\frac{\partial \eta}{\partial t} = w \quad (1.1.17)$$

At the same way, also the *dynamic boundary condition* can be simplified, as $\frac{1}{2}(u^2 + w^2)$ is several orders of magnitude lower than the other terms in Eq. (1.1.16). We obtain:

$$\frac{\partial \Phi}{\partial t} + g\eta = 0 \quad (1.1.18)$$

A further simplification comes from the linearisation of the velocity on the z-axis; from the Taylor expansion of w :

$$w(x, \eta, t) = w(x, 0, t) + \frac{\partial w}{\partial z}(x, z = 0, t)\eta + O(\eta^2) \quad (1.1.19)$$

For the same assumption of small amplitude, we can neglect the term $\frac{\partial w}{\partial z}$. We can then rewrite Eq. (1.1.17) as *linearised boundary condition*:

$$\frac{\partial \eta(x, t)}{\partial t} = w(x, 0, t) \quad (1.1.20)$$

Similarly, we can obtain also a *linearised dynamic condition*:

$$\frac{\partial \Phi(x, 0, t)}{\partial t} = -g\eta(x, t) \quad (1.1.21)$$

The previous problem is then re-proposed in its linearised form:

1. Laplace equation:

$$\frac{\partial^2 \Phi(x, z, t)}{\partial x^2} + \frac{\partial^2 \Phi(x, z, t)}{\partial z^2} = 0 \quad (1.1.22)$$

2. The boundary condition at the seabed:

$$\frac{\partial \Phi}{\partial z}(x, z = -h, t) = 0 \quad (1.1.23)$$

3. The kinematic linearised boundary condition:

$$\frac{\partial \eta}{\partial t}(x, t) = w(x, 0, t) \quad (1.1.24)$$

4. The dynamic linearised boundary condition:

$$\frac{\partial \Phi}{\partial t}(x, 0, t) = -g\eta(x, t) \quad (1.1.25)$$

We now have to find a solution for the above mentioned problem, and we'll look at it among the regular plane waves; for a given z , let's write a Φ of the form:

$$\Phi(x, z, t) = A(z) \sin(\omega t - kx + \phi_0) \quad (1.1.26)$$

where $A(z)$ is the wave amplitude, $\omega = \frac{2\pi}{T}$ is the unknown angular speed, $k = \frac{2\pi}{\lambda}$ is the unknown wave number, T is the wave period, λ is the wavelength, and ϕ_0 is the unknown initial phase. Inserting this function in Eq. (1.1.22), we have:

$$[-k^2 A(z) + A''(z)] \sin(\omega t - kx + \phi_0) = 0 \quad (1.1.27)$$

In order for this equation to be respected for every x and t , the term in brackets has to vanish. Thus:

$$A(z) = C_1 \cosh(kz + C_2) \quad (1.1.28)$$

Eq. (1.1.23) requires then:

$$\frac{\partial \Phi}{\partial z}(x, z = -h, t) = \frac{dA}{dz}(z = -h) \sin(\omega t - kx + \phi_0) = 0 \quad (1.1.29)$$

that is satisfied when $A'(z = -h) = 0$. From Eq. (1.1.28) we get

$$A'(z) = kC_1 \sinh(kz + C_2) \quad (1.1.30)$$

which is equal 0 for $C_2 = kh$ at $z = -h$. The first two equations of our linearised problem are then satisfied by a Φ of the form:

$$\Phi(x, z, t) = C_1 \cosh(k(z + h)) \sin(\omega t - kx + \phi_0) \quad (1.1.31)$$

We still have to satisfy the *kinematic and dynamic boundary conditions*. From Eq. (1.1.25) we have:

$$\eta(x, t) = -\frac{1}{g} \frac{\partial \Phi}{\partial t}(x, z = 0, t) = -\frac{\omega}{g} C_1 \cosh(kh) \cos(\omega t - kx + \phi_0) \quad (1.1.32)$$

and its time derivative:

$$\frac{\partial \eta}{\partial t}(x, t) = \frac{\omega^2}{g} C_1 \cosh(kh) \sin(\omega t - kx + \phi_0) \quad (1.1.33)$$

The above equation must respect Eq. (1.1.24), thus:

$$w(x, z = 0, t) = \frac{\partial \Phi}{\partial z}(x, z = 0, t) = kC_1 \sinh(kh) \sin(\omega t - kx + \phi_0) \quad (1.1.34)$$

For this last condition to be respected in every (x, t) , we must have:

$$\frac{\omega^2}{g} \cosh(kh) = k \sinh(kh) \quad (1.1.35)$$

that can be written as

$$\omega^2 = gk \tanh(kh) \quad (1.1.36)$$

The above equation is called *dispersion relation* and relates two of the parameters of Eq. (1.1.26), respectively the angular frequency ω and the wavenumber k . These parameters can't be chosen randomly, but every couple (ω, k) must satisfy the dispersion relation.

If we impose $\phi_0 = -\pi/2$ and we set the parameter $a = \frac{\omega}{g} C_1 \cosh(kh)$, then we get the equation of a regular wave for η :

$$\eta(x, t) = a \sin(\omega t - kx) \quad (1.1.37)$$

The potential, after several trivial steps, can be written in its complete form:

$$\Phi(x, z, t) = \frac{ag}{\omega} \frac{\cosh(k(z+h))}{\cosh(kh)} z \cos(\omega t - kx) \quad (1.1.38)$$

The basics of linear theory have been reported: what follows is an adaptation of the above equations to special cases, in particular according to the depth of the seabed h .

1.1.2 Sea states description

Regular waves

Linear wave theory in Section 1.1.1 has been set in its general form, but the simplest solution with a sinusoidal, long-crested, progressive wave has been proposed. The main characteristics of *regular waves* are reported as follows [WMO, 1998]:

- *Wave elevation* $\eta(x, t)$ [m]: it is the profile of the water surface and it is function of horizontal position and time.

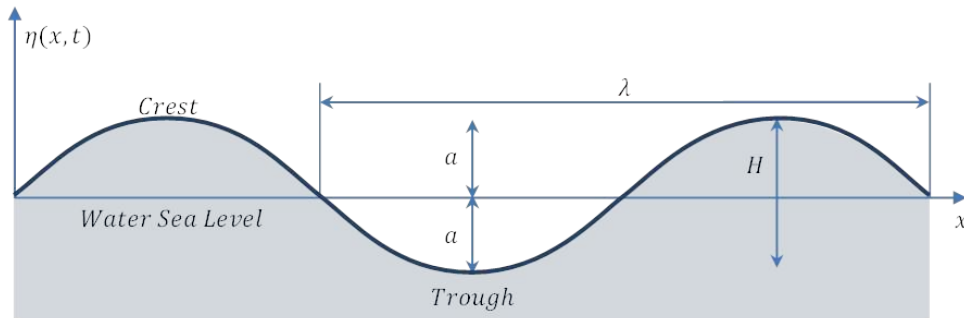


Figure 1.5: Monochromatic wave characteristics.

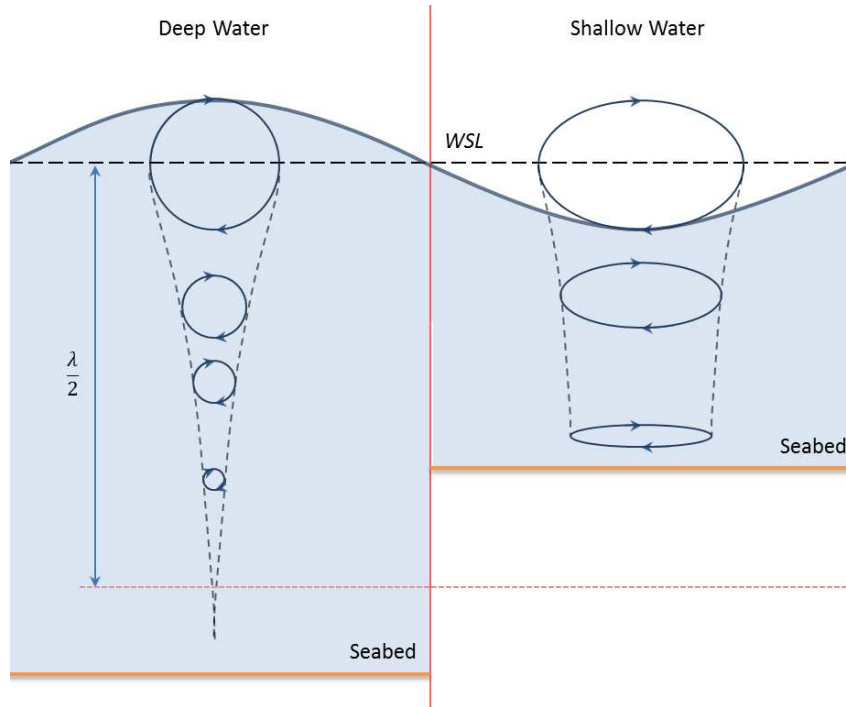


Figure 1.6: Water particles trajectories for deep water and shallow water.

- *Amplitude* a [m]: it is the maximum displacement of the wave elevation from the resting sea level.
- *Height* H [m]: it is the difference in surface elevation from a wave crest and its trough, i.e. for a regular wave $H = 2a$.
- *Period* T [s]: it is the distance in time between two following crests
- *Phase velocity* c [m/s]: it is the speed at which the wave profile travels; for a regular wave $c = \frac{\lambda}{T}$.

The regular wave evolution in space and time can be reported through the equation of its wave profile, corresponding to Eq. (1.1.37):

$$\eta(x, t) = \frac{H}{2} \sin(\omega t - kx) \quad (1.1.39)$$

where:

- $k = \frac{2\pi}{\lambda}$ [rad/m] is the *wavenumber* and defines the periodicity in space.
- $\omega = \frac{2\pi}{T}$ [rad/s] is the *angular frequency* and defines the periodicity in time.

As a result the phase velocity can be rewritten as

$$c = \frac{\lambda}{T} = \frac{\omega}{k}. \quad (1.1.40)$$

As we can see from the dispersion relation, the main wave parameters are affected by the water depth. In deep water particles have a circular path, completing one turn every wave period; the diameter of the trajectories decreases exponentially towards downward. As depth decreases, the sea bed progressively influences the motion, that becomes elliptical.

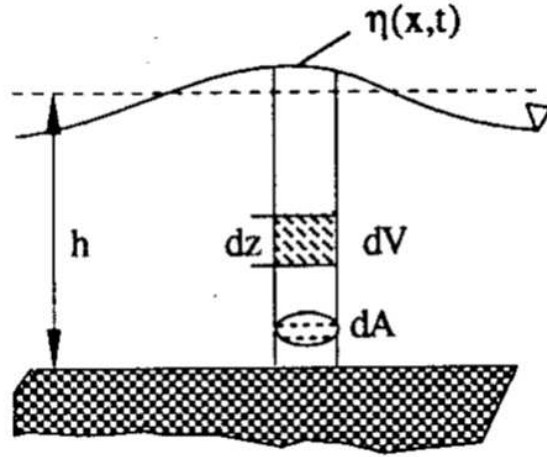


Figure 1.7: Column of water under investigation.

Eq. (1.1.36), for a given k , has two solutions for ω :

$$\omega = \pm \sqrt{gk \tanh(hk)} \quad (1.1.41)$$

where h [m] represents the water depth. If $kh \ll 1$ then $h \ll \lambda$, i.e. the water depth is smaller than the wavelength: it is the *shallow water* case. On the other side, a large kh suggests a *deep water* condition. Starting from this, it is possible to give two different expressions for the dispersion relation.

$$\omega = \pm k\sqrt{gh} \quad \text{for shallow water} \quad (h < \lambda/20) \quad (1.1.42)$$

$$\omega = \pm \sqrt{gk} \quad \text{for deep water} \quad (h > \lambda/2) \quad (1.1.43)$$

As a consequence, also the phase speed can be rewritten:

$$c = \sqrt{gh} \quad \text{for shallow water} \quad (h < \lambda/20) \quad (1.1.44)$$

$$c = \sqrt{g/k} \quad \text{for deep water} \quad (h > \lambda/2) \quad (1.1.45)$$

We will now try to understand how much energy is carried by waves, and in order to do that we will once more refer to [Krogstad and Arntsen, 2000]. As we're dealing with infinite plane waves, we'll try to find out the energy carried per unit area of the surface. The potential energy of a column of water dV having cross section dA as reported in Fig.1.7 is:

$$dE_p = \int_{z=-h}^{\eta} \rho g z dV = dA \int_{z=-h}^{\eta} \rho g z dz = dA \rho g \frac{\eta^2 - h^2}{2} \quad (1.1.46)$$

Only the potential energy in excess is of our interest, thus we have to subtract the potential energy at the resting state:

$$\frac{dE_p - dE_p(\eta = 0)}{dA} = \frac{1}{2} \rho g \eta^2 \quad (1.1.47)$$

Given that the average of η^2 for a sinusoidal wave with amplitude a is $a^2/2$, the *average potential energy*

per unit is given by:

$$\frac{d\overline{E}_p}{dA} = \frac{\rho g a^2}{4} \quad (1.1.48)$$

The kinetic energy is instead derived as

$$dE_k = \int_{z=-h}^{\eta} \frac{1}{2} \rho (u^2 + w^2) dV \quad (1.1.49)$$

Considering deep water and a plane wave as in Eq. (1.1.37), because of the circular trajectory of particles:

$$u^2 + w^2 = (\omega a)^2 e^{2kz} \quad (1.1.50)$$

and therefore:

$$\frac{dE_k}{dA} = \rho \omega^2 a^2 \int_{z=-h}^{\eta} \frac{1}{2} e^{2kz} dz = \frac{1}{2} \rho \omega^2 a^2 \frac{1}{2k} = \frac{1}{4} \rho a^2 g = \frac{d\overline{E}_k}{dA} \quad (1.1.51)$$

We can observe that kinetic energy does not change with time, i.e. its average is equal to the instantaneous value. Furthermore, we observe that potential energy and kinetic energy average values are equal. Summing the two terms of average energy per unit area as functions of the wave height $H = 2a$, we obtain an expression for the *wave energy density*:

$$E_d = \frac{dE_p}{dA} + \frac{dE_k}{dA} = \frac{\rho g H^2}{16} + \frac{\rho g H^2}{16} = \frac{\rho g H^2}{8} \quad (1.1.52)$$

The velocity at which energy propagates is not the phase one, but rather another quantity called *group velocity* [m/s]. For a full explanation of this concept please refer to [Newman, 1977]; here we limit ourselves to report its definition:

$$c_g = \frac{d\omega}{dk} \quad (1.1.53)$$

For deep water, using Eq. (1.1.43) in the group velocity:

$$c_g = \frac{d\omega}{dk} = \frac{g}{2\omega} = \frac{g/\omega}{2} = \frac{c}{2} \quad (1.1.54)$$

while for shallow water, using Eq. (1.1.42), it'll be:

$$c_g = \frac{d\omega}{dk} = \sqrt{gh} = c \quad (1.1.55)$$

Using the concept of group velocity and Eq. (1.1.52), we can write an expression for the *wave power density* [W/m], i.e. the energy per crest unit length:

$$P_d = \frac{\rho g H^2}{8} c_g \quad (1.1.56)$$

Considering Eqs. (1.1.40) and (1.1.43) we can write for deep water:

$$\lambda = \frac{g}{2\pi} T^2 \approx 1.56 T^2 \quad (1.1.57)$$

At the end, considering $\rho = 1025$ [kg/m³] we can derive an approximated but simple form of the power

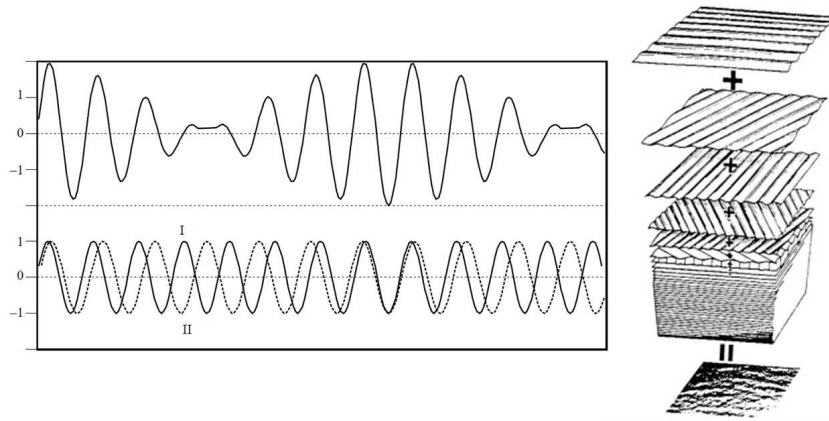


Figure 1.8: Irregular 3D waves as a superposition of regular plane waves [WMO, 1998].

density per unit length in deep water:

$$P_d = \frac{\rho g^2 H^2 T}{32\pi} \cong H^2 T \quad (1.1.58)$$

Irregular waves

Linear wave theory effectively explains regular plane waves, but real seas are often far from that condition. However, real sea states can be described as the superposition of a high number of regular waves having different propagation direction, amplitude, frequency, wavelength and phase. Consider that both (η_1, Φ_1) and (η_2, Φ_2) are solutions of the system of linearised equations of Eqs. (1.1.22) to (1.1.25): also $(\eta_1 + \eta_2, \Phi_1 + \Phi_2)$ will be a solution. Similarly, we can add together an arbitrary number of plane waves. Since we're not anymore acting in a channel but rather in an open 3D sea, there's the need for replacing x with the vector \mathbf{x} identified by coordinates (x, y) and k by the vector \mathbf{k} of coordinates (k_x, k_y) (see [Krogstad and Arntsen, 2000] for further explications). The equations for the wave elevation and the potential of the superposition of regular waves will be respectively:

$$\eta(\mathbf{x}, t) = \sum_{n=1}^N a_n \sin(\omega_n t - \mathbf{k}_n \mathbf{x} + \alpha_n) \quad (1.1.59)$$

$$\Phi(\mathbf{x}, z, t) = \sum_{n=1}^N \frac{a_n g}{\omega_n} \frac{\cosh(k_n(z+h))}{\cosh(k_n h)} \cos(\omega_n t - \mathbf{k}_n \mathbf{x} + \alpha_n) \quad (1.1.60)$$

where each term corresponds to a plane wave with:

- Amplitude a_n .
- Angular frequency ω_n .
- Wavenumber vector \mathbf{k}_n
- Phase α_n at $t=0, \mathbf{x}=0$.

A practical description of real sea states can be performed through *random linear wave theory*, whose basic concepts are presented in the following pages [Krogstad and Arntsen, 2000]. Starting from Eq.

(1.1.59), we know that every component travels at its own speed and contribute to the wave elevation η in every instant of time. For given \mathbf{x} and t , set $\omega t - \mathbf{k}\mathbf{x} = \Phi_0$. The average and the variance of the function $\sin(\Phi + \Phi_0)$, where Φ is uniformly distributed on $[0, 2\pi]$, will be:

$$E(\sin(\Phi + \Phi_0)) = \frac{1}{2\pi} \int_0^{2\pi} \sin(\Phi_0 + \Phi) d\Phi = 0 \quad (1.1.61)$$

$$\text{Var}(\sin(\Phi + \Phi_0)) = \frac{1}{2\pi} \int_0^{2\pi} (\sin(\Phi_0 + \Phi) - 0)^2 d\Phi = \frac{1}{2\pi} \int_0^{2\pi} \frac{1 - \cos(2(\Phi_0 + \Phi))}{2} d\Phi = \frac{1}{2} \quad (1.1.62)$$

As Φ_i are uniformly distributed variables, we'll have:

$$E(\eta(\mathbf{x}, t)) = \sum_{n=1}^N a_n E(\sin(\Phi_0 + \Phi)) = 0 \quad (1.1.63)$$

$$\text{Var}(\eta(\mathbf{x}, t)) = \sum_{n=1}^N a_n^2 E(\sin^2(\Phi_0 + \Phi)) = \sum_{n=1}^N a_n^2 \frac{1}{2} \quad (1.1.64)$$

Considering the surface as composed by an infinite number of waves, we can rewrite $a_n = a(\mathbf{k}_n)$, thus the variance is:

$$\sum_{n=1}^N a(\mathbf{k}_n)^2 \frac{1}{2} = \int_{-\infty}^{+\infty} \int_{-\infty}^{+\infty} \Psi(k_x, k_y) dk_x dk_y \quad (1.1.65)$$

where $\Psi(k_x, k_y) = \Psi(\mathbf{k})$ identifies the density of waves around the wavenumber \mathbf{k} and is called *wavenumber spectrum*. Since we have that:

$$\text{Var}(\eta(x, t)) = E((\eta(\mathbf{x}, t) - 0)^2) = \int_k \Psi(k) dk^2 \quad (1.1.66)$$

the function $\Psi(\mathbf{k})$ is also called *variance density of the wavefield*. Starting from Eq. (1.1.51) and considering that $H = 2a$, the wave energy density in the regular case was:

$$E_d = \rho g \frac{a^2}{2} \quad (1.1.67)$$

that in the irregular case becomes:

$$E_d = \rho g \text{Var}(\eta) = \rho g \int_k \Psi(\mathbf{k}) d^2k \quad (1.1.68)$$

Since $\mathbf{k} = k(\cos(\theta)\mathbf{i} + \sin(\theta)\mathbf{j})$, we can rewrite Eq. (1.1.66) in terms of polar coordinates (k, θ) :

$$\text{Var}(\eta) = \int_k \Psi(\mathbf{k}) d^2k = \int_{k=0}^{\infty} \int_{\theta=0}^{2\pi} \Psi(k, \theta) k dk d\theta \quad (1.1.69)$$

Because of the dispersion relation of Eq. (1.1.41), we can change a variable from k to ω :

$$\text{Var}(\eta) = \int_{k=0}^{\infty} \int_{\theta=0}^{2\pi} \Psi(k, \theta) k dk d\theta = \int_{\omega=0}^{\infty} \int_{\theta=0}^{2\pi} \Psi(k(\omega), \theta) k(\omega) \frac{dk(\omega)}{d\omega} d\omega d\theta = \int_{\omega=0}^{\infty} \int_{\theta=0}^{2\pi} E(k, \theta) d\omega d\theta \quad (1.1.70)$$

where:

$$E(k, \theta) = \Psi(k(\omega), \theta) k(\omega) \frac{dk(\omega)}{d\omega} \quad (1.1.71)$$

is called the *directional wave spectrum*. It can be divided highlighting an angular dependent part and a not angular dependent part:

$$E(k, \theta) = \tilde{S}(\omega)D(\omega, \theta) \quad (1.1.72)$$

where the second term on the right is normalised on all the directions for each frequency. The function $\tilde{S}(\omega)$ is called *wave frequency spectrum*, and it has a corresponding function $S(f)$ defined by:

$$S(f) = \tilde{S}(\omega = 2\pi f) \frac{d\omega}{df} = 2\pi S(2\pi f) \quad (1.1.73)$$

which tells us how much energy is carried by each frequency component of the real sea; its units are [m^2s]. The spectrum introduced so far represents the connection between the linear wave theory and the random one, and permits to consider a continuum of plane regular waves. In particular, we can recall that the integral over k and θ of $E(k, \theta)$ is the variance of the wave elevation, and can thus be inserted in Eq. (1.1.68) for the calculation of the energy density.

Starting from a wave elevation record as the one reported in the upper plot of Fig. 1.8, we can identify the main statistical parameters used for the description of random waves. The most important is the *significant wave height* H_{m0} , that is defined as four times the standard deviation of the wave elevation, i.e. the square root of its variance:

$$H_{m0} = 4\sqrt{m_0} \quad (1.1.74)$$

where:

$$m_k = \int_0^\infty f^k S(f) df \quad (1.1.75)$$

is called *spectral moment* of order k ; m_0 is the most important and it is nothing but the variance of the surface. Another important quantity is the *peak frequency* f_p , defined as the frequency for which:

$$S(f_p) = \max S(f) \quad (1.1.76)$$

The *peak period* is then defined as:

$$T_p = \frac{1}{f_p} \quad (1.1.77)$$

and it corresponds to the wave period with the highest energetic content within the waves that are taking part to the random sea surface. It is also defined a *wave energy period* as

$$T_e = \frac{m_{-1}}{m_0} \quad (1.1.78)$$

There exist several different expressions for the wave frequency spectrum $S(f)$: the most famous is probably the *JONSWAP* (*Joint North Sea Wave Observation Project*), derived from the *Pierson-Moskowitz* one. The expression of the latter is:

$$S_{PM}(f) = A \frac{e^{-B/f^4}}{f^5} \quad (1.1.79)$$

where:

$$A = \frac{5}{16} H_{m0}^2 f_p^4 \quad (1.1.80)$$

$$B = 5 \frac{f_p^4}{4} \quad (1.1.81)$$

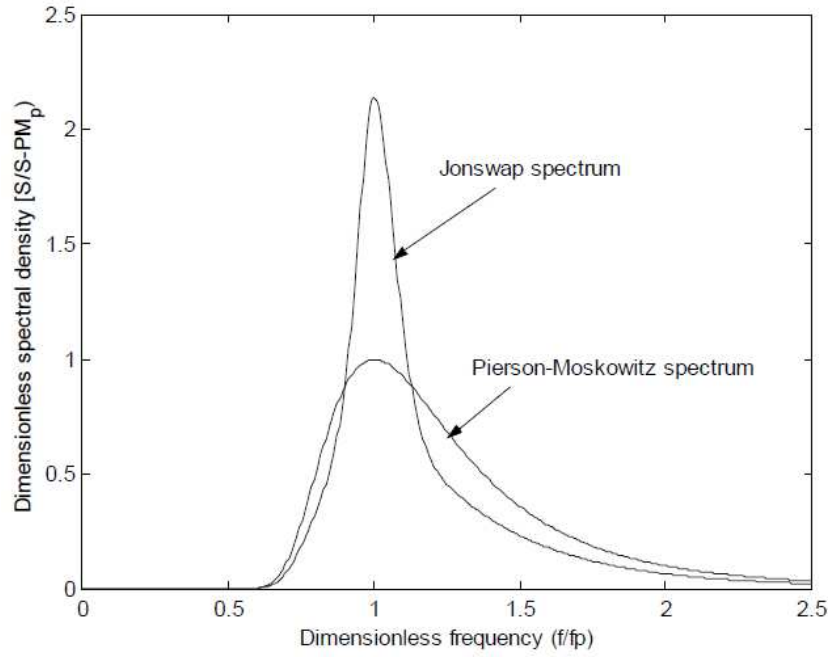


Figure 1.9: The Pierson-Moskowitz spectrum and the JONSWAP spectrum with $\gamma = 3.3$ normalized on the Pierson-Moskowitz peak [Krogstad and Arntsen, 2000].

The JONSWAP spectrum [Hasselmann et al., 1973] is a Pierson-Moskowitz multiplied by a peak enhancement factor that can change from location to location:

$$S_J(f) = S_{PM}(f)\gamma \exp\left(-\frac{(f-f_p)^2}{2\sigma^2 f_p^2}\right) \quad (1.1.82)$$

Starting from Eq. 1.1.52 or Eq. 1.1.67 for regular waves, it is possible to derive an expression for the wave energy density contained in an irregular sea state. For a regular wave the variance of the surface elevation can be written as:

$$m_0 = \sigma_0^2 = \overline{(\eta - \bar{\eta})^2} = \frac{1}{2}a^2 \quad (1.1.83)$$

and the energy density can be written as:

$$E_d = \rho g m_0 \quad (1.1.84)$$

Switching to irregular waves, the above formulation is still valid (see Eq. (1.1.68)). Using H_{m0} from Eq. (1.1.74), we have finally a suitable expression of the energy density for an irregular sea state [Holthuijsen, 2010]:

$$E_d = \frac{\rho g H_{m0}^2}{16} \quad (1.1.85)$$

For the same reasons that led to Eq. (1.1.58), we can write the power density per unit crest length for irregular waves in deep water as:

$$P_d = \frac{\rho g H_{m0}^2}{16} c_g \approx 0.49 H_{m0}^2 T_e \quad (1.1.86)$$

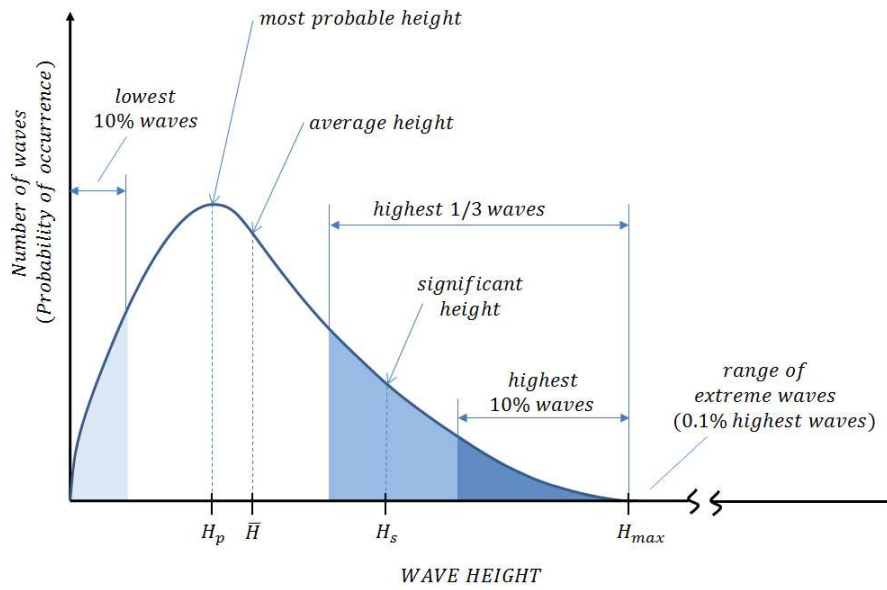


Figure 1.10: Significant wave height from the probability density function diagram [Raffero, 2014].

From a short term point of view, the actual wave heights for a certain significant wave height follow a statistical distribution that can be accurately approximated with a Rayleigh probability curve [Krogstad and Arntsen, 2000]. Its cumulative can be written as:

$$P(H \leq h) = 1 - e^{-2(\frac{h}{H_{m0}})^2} \tag{1.1.87}$$

and its probability density function is represented in Fig. (1.10), with the identification of the H_{m0} . The wave period is instead difficult to be described in simple terms, but especially it does not exist a form of the joint distribution of wave height and period in a defined sea state.

From a long term point of view, sea states statistics is described making use of two of the quantities derived so far: the significant wave height H_{m0} and the peak wave period T_p . The former follows a distribution that can be approximated with a Weibull function; its cumulative is given by:

$$P(H_{m0} \leq h) = 2 - \exp(-((h - H_0)/(H_e - H_0))^\gamma), h \geq H_0 \tag{1.1.88}$$

where H_c, H_0 and γ are parameters. However, a common way of representing the occurrence of different sea states within an analysed time period is a *scatter plot* as the one represented in Fig. (1.11).

1.1.3 Global wave energy potential

An estimate of the wave energy potential around the world is fundamental to justify and push for large public and private investments in the wave energy sector. However, due to the complicated description of the resource and the large scale of such an estimate, the data presented below should be read with caution.

The wave energy potential can be seen from different points of view. The easiest is to consider the *theoretical resource*, that represents the actual hydrodynamic power contained in ocean waves. Depending on the choices made by researchers, this value may be reduced by the potential contained in areas which

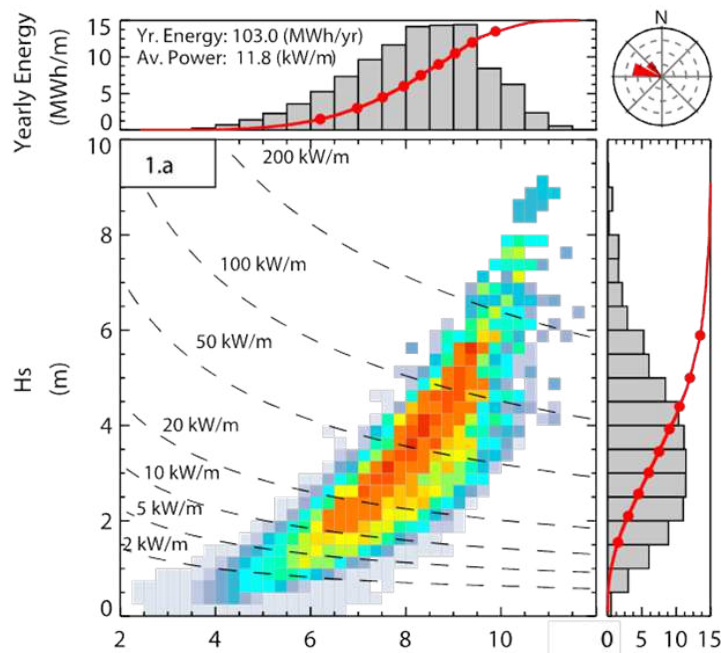


Figure 1.11: Scatter diagram for the Alghero location [Raffero, 2014].

are not considered exploitable even in the face of modest technological development. Another important quantity is the *technical resource*, i.e. the power that can be produced in a specific area by a certain wave energy converter. In this section we'll limit ourselves to report some data on the theoretical resource, while the next section will focus on the different types of wave energy converters that have been and are being developed.

The following information come from [Mørk et al., 2010], where an estimate of global wave potential is made continent by continent. Researchers used the WorldWaves package, consisting of a model for a 10-year period at 6-hourly intervals on a 0.5° lat/long worldwide grid calibrated using NASA/CNES satellite observations. Calibration led to adjust some wave periods and heights in enclosed seas, as the Mediterranean, where the sea surface is often influenced strongly by wind. Areas excluded for low feasibility are ones with very low power levels (power density per crest length ≤ 5 kW/m) and those where ice occurs during the year.

Results are reported in Tab. 1.2 and Fig. (1.12). The net resource is of almost 3 TW, against the 3.7 TW of the gross resource (as a measure of comparison, think that the average gross power required in Italy is equal to 39.1 GW); the Mediterranean sea undergoes a 50% reduction because of many low-power areas. Overall, the most energetic latitudes are among 40° and 60° in both the northern and southern hemisphere. Fig. (1.13) represents the seasonality of the resource, intended as the ratio between the minimum monthly wave power and the annual one: thus, lower values indicate higher seasonality. According to the author's opinion, the high seasonality that characterizes many areas of the northern hemisphere is a fairly important obstacle for the development of wave energy, being in some cases the average available power up to seven times higher in winter than in summer. Despite for largely electrified power systems in the north of the world the electrical consumption can be higher in winter than in summer, this difference does not normally exceed the 50% of the summer months consumption. One of the most interesting challenges related to wave energy can be the search for the right complementary

Table 1.2: Global and regional theoretical wave power resource - areas with $P < 5$ kW/m and ones potentially covered by ice are not considered [Mørk et al., 2010].

Region	P [GW]	P _{net} [GW]
Europe (N and W)	381	286
Baltic Sea	15	1
European Russia	37	3
Mediterranean	75	37
North Atlantic Archipelagos	111	111
North America (E)	115	35
North America (W)	273	207
Greenland	103	3
Central America	180	171
South America (E)	206	202
South America (W)	358	324
North Africa	40	40
West and Middle Africa	77	77
Africa (S)	178	178
Africa (E)	133	127
Asia (E)	173	157
Asia (SE) and Melanesia	356	283
Asia (W and S)	100	84
Asiatic Russia	172	23
Australia and New Zealand	590	574
Polynesia	63	63
TOTAL	3702	2985

sources and technological solutions that could cover the missing power from waves during summer months. An ideal candidate could be photovoltaic energy, using a panel inclination optimized to produce energy in summer months rather than in the whole year.

1.2 Wave Energy Converters

1.2.1 Historical notes and technology policies

Studies for the exploitation of wave energy have started in a fairly recent period, if compared to other renewable sources: the oscillatory motion of waves is more difficult to be studied and used for energy production than other more constant movements, such as those of tides or wind. In the following paragraphs we will try to explain in general terms the history of the exploitation of energy from waves, and then identify the main policies for the development of technology at European and global level. Most part of the information reported in this section comes from [Falcão, 2010] and [Novo, 2015].

The first patent for a device designed to capture energy from ocean waves was obtained in Paris, dates back to 1799 and bears the signature of Girard, father and son [Lynn, 2013]. However, there is no evidence that the device has ever been built. A century later, in 1898, a US citizen named Wright invented a wave motor system consisting of a hinged float that rode the waves and operated a hydraulic pump (Fig. 1.14a). In 1910 another French, Bochaux-Praceique, invented a device that allowed him to illuminate his house: the oscillatory motion of water in a semi-submerged chamber led to the compression of the air

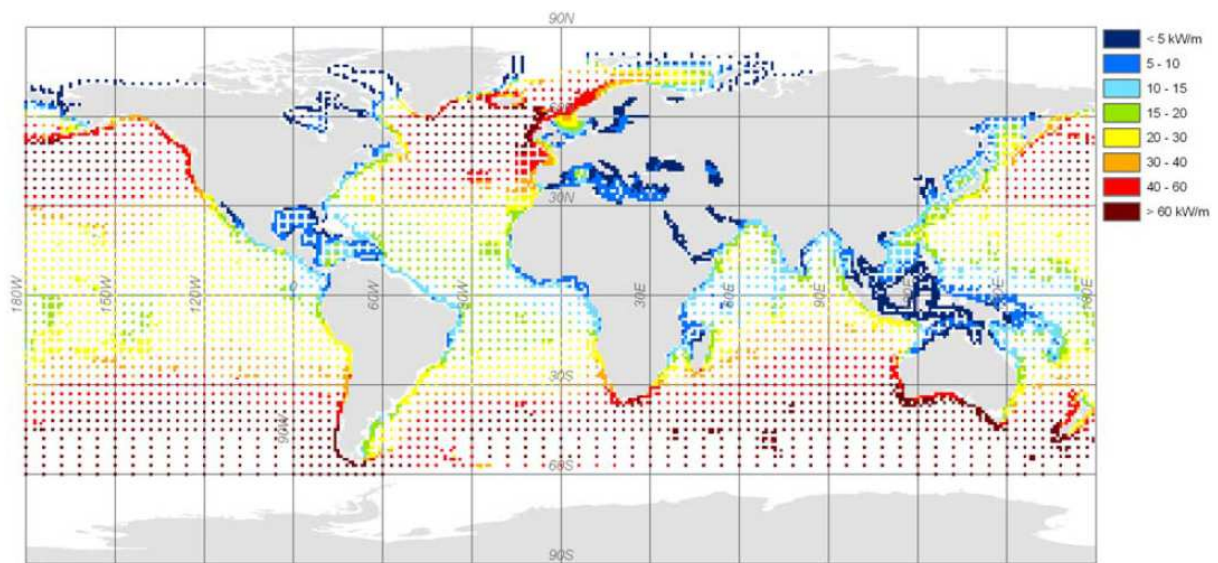


Figure 1.12: Annual global theoretical wave power for all WorldWaves grid points [Mørk et al., 2010].

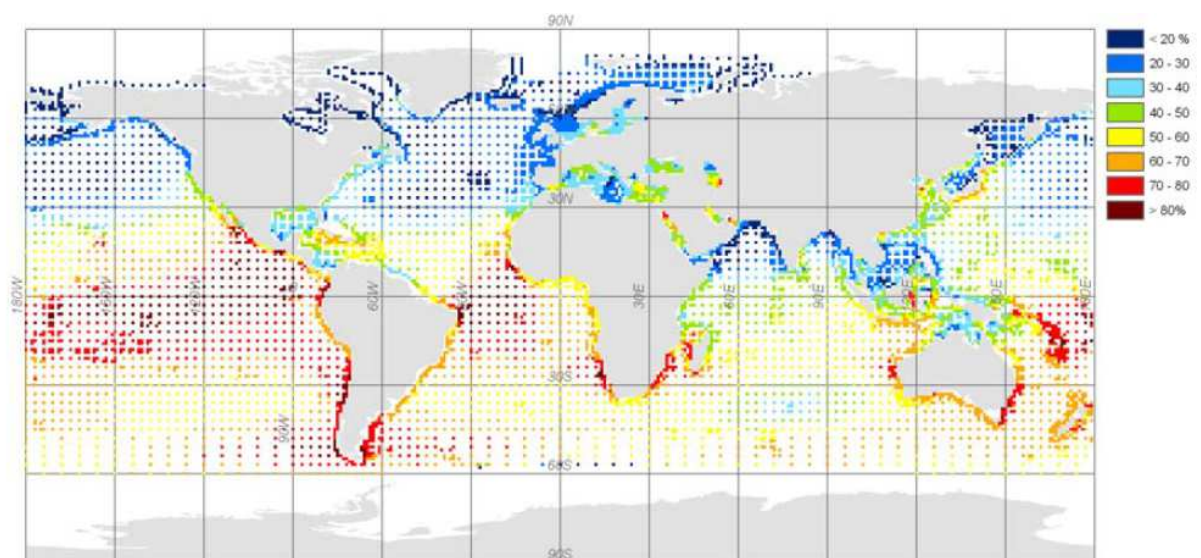
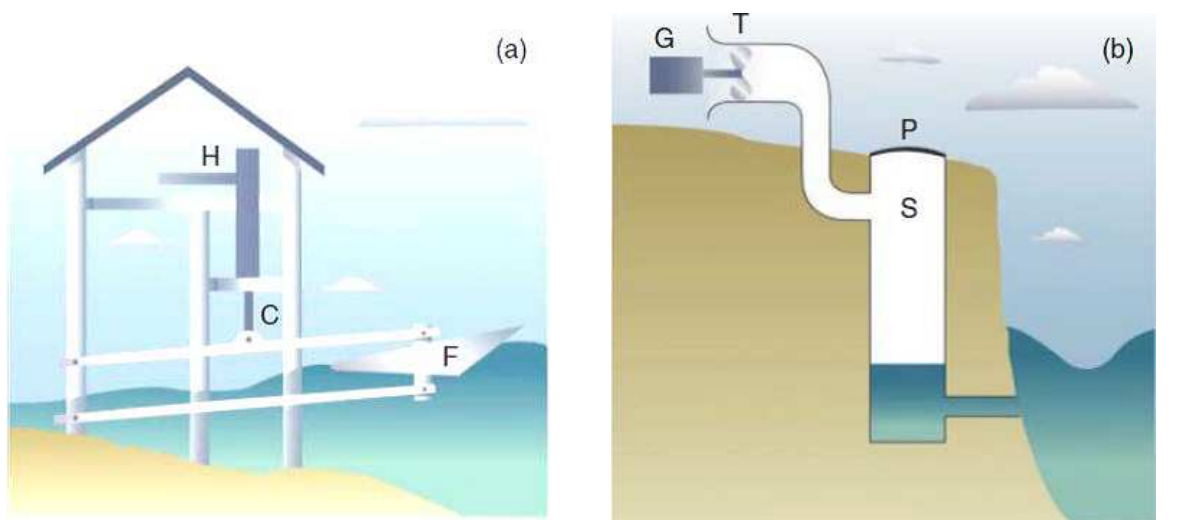


Figure 1.13: Seasonality of the wave resource - ratio of minimum monthly wave power and annual wave power [Mørk et al., 2010].

trapped over the free water surface, which made a turbine rotating (Fig. 1.14b). In the 20th century, many inventors devoted efforts to the wave energy field: in 1980 you could count more than a thousand patents [McCormick, 2013].

The Meadows Report on *The Limits to Growth* [Meadows et al., 1972] and the '70s oil crises pushed the research toward alternative sources in order to replace fossil fuels, and also the production of energy from waves for feed-in to the power grid entered the spotlight of the scientific community. The first Governments to support R&D programs in wave energy were the British and the Norwegian one, but the research was mainly performed at academic level up to the 90s [Falcão, 2010]. In 1991 the European Commission included wave energy in the research and development programs on renewable energies: the European Union started funding several different projects and sponsoring a series of *European Wave Energy Conferences*. Within its Programme for Research and Innovation *Horizon 2020*, the European Commission started funding ETIP Ocean, an advisory board with the aim of defining research and innovation priorities for the ocean energy sector. The board is coordinated by *Ocean Energy Europe*, a network of utilities, companies and research institutes active in the ocean energy sector. The declared target of the European wave energy industry seems ambitious: it consists in meeting the 10% of the electricity demand of the EU by ocean resources by 2050. The European Commission's *Ocean Energy Forum* of 2016 outlined a Roadmap of four Action Plans to achieve this objective [OEF, 2016]:

- **Action Plan 1 - R&D and Prototype:** setting performance indicators that need to be met before moving from one development step to the next one, in terms of power generation, availability, survivability, affordability, installability. Highlighting interdependencies of projects and initiatives in order to check the coherence and comparability of results. Constitution of a Fund with contributions from Member States to fund a significant share of development project costs.
- **Action Plans 2 and 3 - Demonstration & pre-commercial:** de-risking of pre-commercial projects up to their maturity through a Fund helping developers to access other private and public financing sources. Creation of an Insurance and Guarantee Fund to support deployment of the first demonstration and pre-commercial farms. Guarantee on availability, output performance, mechanical



(a) Wright's wave motor - 1898 [Lynn, 2013].

(b) Bocheaux-Praceique wave device - 1910 [Lynn, 2013].

Figure 1.14: Early wave energy devices

breakdown and defect.

- **Action Plan 4 - De-risking environmental consenting through an integrated programme of measures:** review of planning processes to facilitate installation sites selection through marine spatial planning. Identification of technique requirements and processes to secure applications, from the screening to the post-construction monitoring. Understanding for all involved parties of the impacts on the environment on ocean energy projects. Involvement of communities and local economy to continue attracting political support at different levels.

More recently, the interest in wave energy grew also in North-American and Asiatic countries, with increasing investments in research and development by both public sector and private companies. The *International Energy Agency*, an OECD intergovernmental organization having the mission of promoting the energy security of its partner countries, has been dealing with ocean energy since 2001; more recently, IEA established a *Technology Collaboration Programme* with the main aims of assessing the environmental effects of wave energy technologies and accelerating the energy device project development [OES, 2016].

Many different projects on wave energy are underway all around the world. It’s interesting to note how the larger part of them are being developed in the northern hemisphere of the world, generally more economically developed and energy intensive, despite the fact that the analysis of the resources suggests a really high potential especially in the southern hemisphere. As suggested in [REN21, 2017], wave energy most important progresses in 2016 were related to several pilot projects developed around the world, the most important being in Spain, Sweden, the United States, South Korea and China. Fig. 1.15 reports the global investments in renewable energy in 2016. Investments on ocean energy, mainly in wave and tidal technology, mirror the early technological development stage of the field: as no further investments have been done in large tidal plants, the USD 211 million invested in ocean energy have been spent for R&D and demonstration projects. However data are encouraging, given that investments in ocean energy amount to about 10% of those in geothermal energy, whose technology is well established.

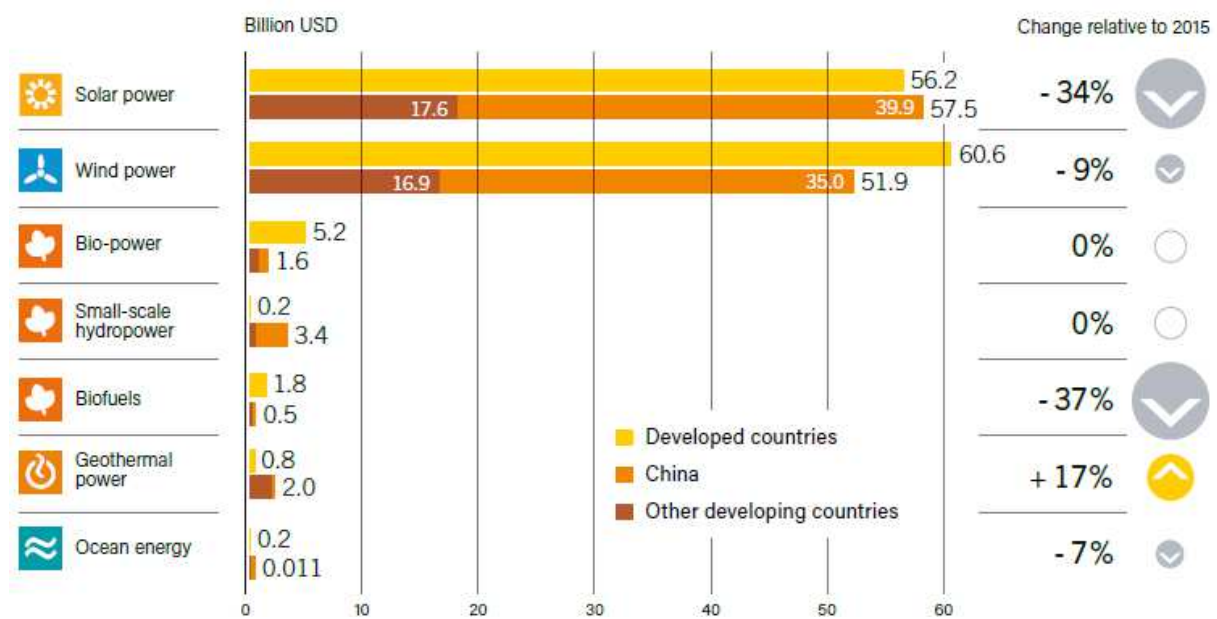


Figure 1.15: Global new investments in renewable energy by technology, 2016 [REN21, 2017].

Among the most active countries in financing research and development projects there is Scotland, that with the governmental subsidiary *Wave Energy Scotland* has awarded about USD 14.5 million to wave energy developers in 2016.

1.2.2 State of the art

There are many different technologies for harvesting energy from sea waves, and none of them has yet taken precedence over the others; while every year some projects are abandoned, new devices continue to be created. The feasibility of using a device is related to the characteristics of its location: prevailing sea-states, variability on short and long term, conformation of the seabed and of the coast. For this reason, it is likely and desirable that several technologies could be soon commercially available. There exist several different classifications for WECs: probably the most intuitive and complete classification is based on the working principle, such as the one reported in Fig. 1.16. This subsection will be devoted to a description of the different categories of converters; large part of the following information still comes from [Falcão, 2010], a study survey that contains a comprehensive review of existing technologies.

The Oscillating water column

Oscillating water column (OWC) devices produce energy through a turbine driven by the compressed air following the oscillatory motion of sea waves; the working principle is similar to the one of the Bocheaux-Praceique device of Fig. 1.14b. The first modern devices to be developed were *floating-structure* OWCs, assembled in Japan between the 60s and the 70s. A simple scheme of floating OWC is the *spar buoy* reported in Fig. 1.17a: it is an axisymmetric device with a vertical hollow tube opened on both extremities and fixed to a floater (buoyancy volume); a ballast on the lower part increases the stability of the device, that is normally slack-moored to the sea bed. This kind of devices have been so far used in wave-powered navigation buoys, that require low powers, as a valid alternative to the highly diffused photovoltaic driven buoys. Other floating OWCs have an asymmetric shape, that makes them sensitive to wave direction and can get higher rated powers; an example of this device is shown by Fig. 1.17b, representing the *Backward Bent Duct Buoy*.

Concerning *fixed-structure* OWCs, most of them are built on the shoreline or near-shore; the lower energy transported by waves near the shore can be compensated by refraction phenomena present in specific locations. The main advantages of shoreline devices are the simplified installation and maintenance and the absence of submarine cables. In general, fixed-structure OWCs have a partially submerged concrete or steel structure with an opening in atmosphere on the top and one on the bottom, under the water surface. As we can see in Fig. 1.18a, OWC chambers are preferably protruded in the direction of waves: this can improve significantly the energy harvesting process, as it has been found theoretically in [Count and Evans, 1984] and experimentally proven. The construction of the structure for fixed OWCs is probably the most sensitive part of the technology, as well as the most expensive: structures must withstand considerable stresses, as proved by the unfortunate end made by OSPREY, a big prototype of near shore bottom-standing OWC destroyed by waves soon after its installation. The integration of these devices with existing breakwaters can significantly reduce installation costs, and thus energy production ones. The plant in Fig. 1.18b is an example of OWCs whose installation costs have been shared with those of a new breakwater installed out of the port of Mutriku, on the north coast of Spain.

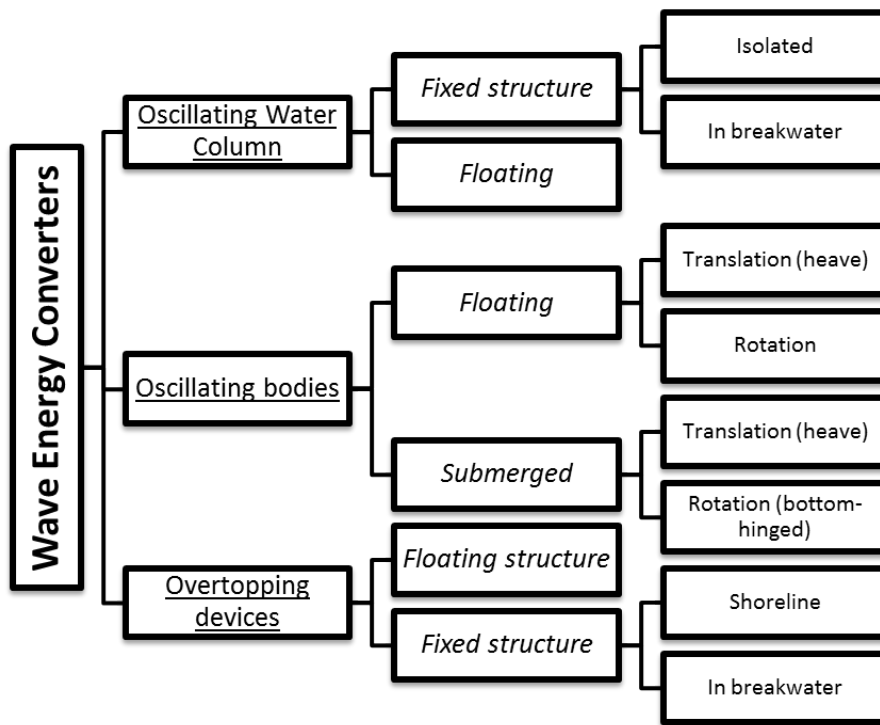
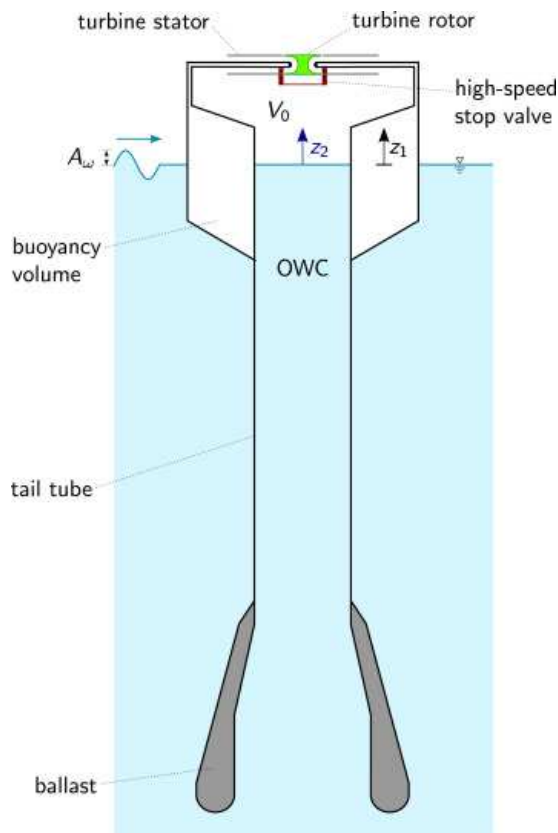
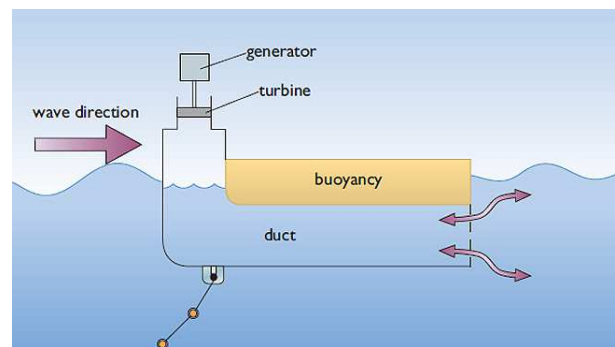


Figure 1.16: Wave energy technologies categorisation [Falcão, 2010].



(a) Longitudinal section of a OWC spar-buoy [Henriques et al., 2016].



(b) Schematic representation of the Backward Bent Duct Buoy [OpenLearn, 2018].

Figure 1.17: Floating Oscillating Water Column devices.

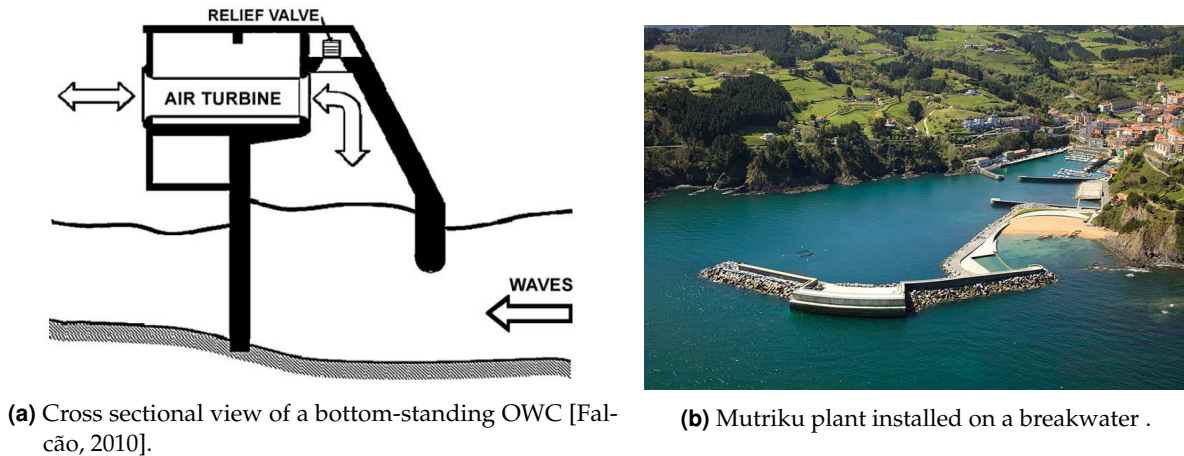


Figure 1.18: Fixed-structure Oscillating Water Column devices.

Concerning the air turbines used in OWCs, designers so far have preferred to use Wells turbines, that rotate in the same direction independently of the direction in which air flows. Unidirectional turbines would indeed require the use of self-rectifying valves, that lead to higher mechanical complexity and lower reliability of the whole system. Several researchers have been working over the years on valid bidirectional alternatives to the Wells turbines, that have several disadvantages, mainly low efficiency and poor starting characteristics [Takao and Setoguchi, 2012]. Furthermore, Wells turbines can also produce really high noise levels, as proved by the same Mutriku plant, dubbed "dragoia" (dragon in Basque language) by the local population.

Oscillating bodies

Oscillating body systems are the widest category of WECs: they include many different devices having different operating principles. Looking for a general definition, we can say that oscillating bodies share the characteristic of producing energy from the relative motion of two points; differences between them consist in the different positions assumed by the two reference points and the degree of freedom that is actually exploited for the energy production. In the following paragraphs we will try to propose an overview of existing devices following the classification of Fig. 1.16.

Floating devices have the advantage of exploiting the higher energy present in deep water rather than near shore. *Heaving systems* harvest wave energy taking advantage of the vertical translation motion between two points; *single body heaving buoys* have a unique floating body, while the second reference point is on the sea-bed or on the bottom of the device. A famous device of this type, represented in Fig. 1.19a, has been developed at Uppsala University; characterised by simplicity and robustness, its linear generator is placed on the sea-bed and is supported by some springs that limit its movement and generate a restoring force [Waters et al., 2007]. In *multi-body heaving systems* energy is produced thanks to the different oscillations of two bodies: one of them floats, while the second is submerged. Despite a slack mooring is always necessary, the "useful distance" for energy production is limited: this makes it possible using rigid connections between the reference points and avoiding problems related to tidal height differences. An example of such a device is the Irish device called *Wavebob*, producing energy through a high-pressure oil system (Fig. 1.19b).

Another subgroup of floating WECs is composed of *pitching devices*, that exploit the relative rotational

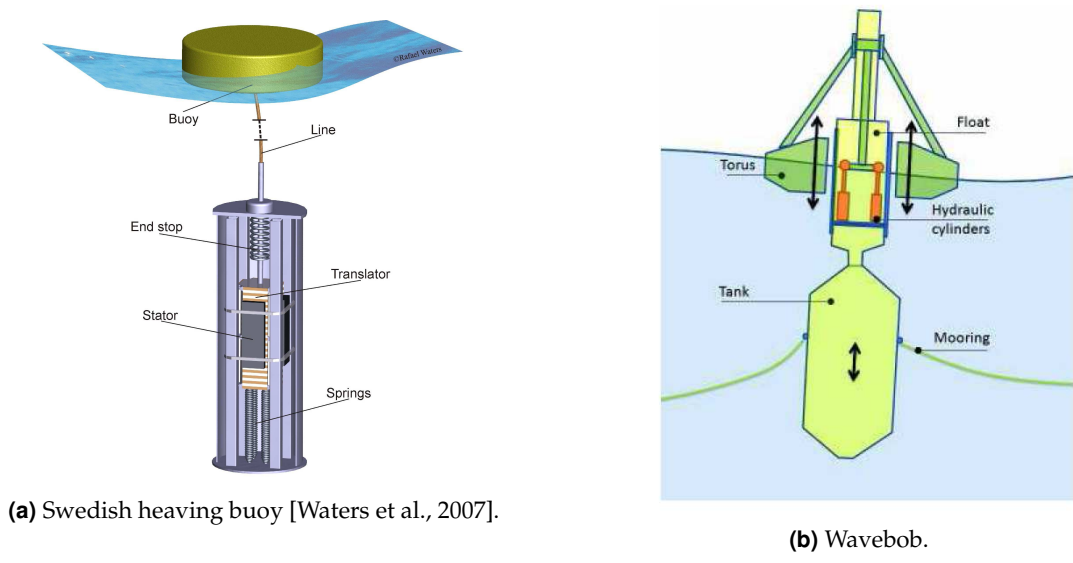


Figure 1.19: Floating heaving systems.

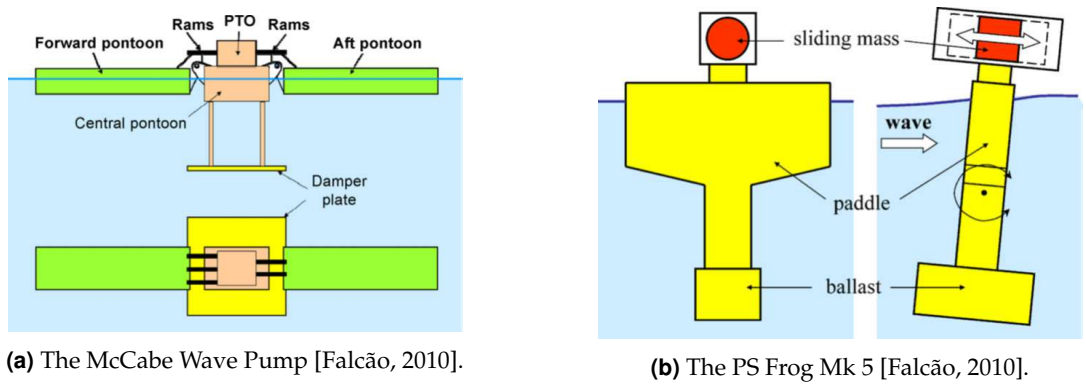


Figure 1.20: Pitching devices

motion of two or more bodies. An example of devices having all the reference bodies in contact with water is the *McCabe Wave Pump*, reported in Fig. 1.20a; the structure consists of three pontoons, the central one being rather stable thanks to a submerged damper plate. The motion of the rams connecting the lateral pontoons to the central one allows energy production through an hydraulic PTO [Falcão, 2010]. There also exist pitching devices where just one of the bodies is in contact with water, while the other is enclosed in it and connected with a certain degree of freedom; the pitch motion of the enclosing system involves thus a motion on the second body, permitting to harvest energy. A suitable example is given by the *PS Frog Mk 5*, made of a large buoyant paddle connected with a ballast; on the top of the device there's a sliding mass, from whose motion energy is harvested (Fig. 1.20b).

Submerged devices are always anchored to the sea bed and can be divided in two further groups. The first group is the one of *submerged heaving systems*, that make use of the pressure differential in the vertical direction through the motion of a floater with respect to the seabed. It is important to highlight that the floater reaches its upper position in correspondence with a wave trough, and vice-versa. The second group of submerged devices is the one of *bottom-hinged systems*: these devices are stressed on the surge motion, but rotate around their seabed attachment point. As a result, a fluid is pressurized and converted into electricity through a conventional hydraulic circuit; this last process normally takes place on shore.

Depending on the specific device and the tide level, bottom-hinged systems may or may not have a part out of the water.

Overtopping devices

The third and last category of WECs is the one of the *overtopping devices*, characterised by strong non-linearities; their study can't be addressed through the linear wave theory [Falcão, 2010]. Water is captured on the top of the wave crests and stored in a reservoir at a higher level with respect to the average sea level; water can then go back to the sea through one or more low-head turbines, thus generating mechanical energy and electricity; structures can be near-shore or floating. The use of several reflectors and a ramp can substantially increase the amount of water filling the reservoir, as done for the Wave Dragon device (Fig. 1.21).

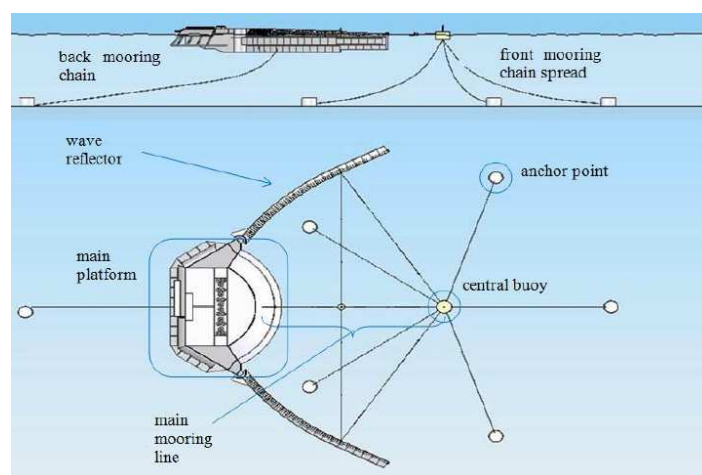


Figure 1.21: Wave Dragon scheme [Parmeggiani et al., 2013].

1.2.3 Numerical modelling of WECs

This section aims at giving an overview of the different numerical methods available for the study of WECs. As previously explained, representing accurately the operation of WECs is an issue of central importance in the wave energy field, mainly because of the early stage of development of the technology, of the relatively high installation costs in sea and of the high number of control parameters that characterise these devices. There are several different numerical methods for the modelling of WECs: they can be classified according to the theory behind them and the way in which non-linearities are dealt with. Non-linear effects can have different origins, mainly the resource (or incoming wave), the wave-body interaction (e.g. viscous effects, variation of wetted surface), and the power take-off (that is the system transforming the absorbed energy into usable electricity).

A classification of the main available numerical models is depicted in Fig. 1.22. The first family of models seeks direct solutions of the *Navier-Stokes equations*; *Computational fluid dynamics (CFD)* models are used for their numerical solution, and are based on space and time discretization. The second group consists of models that are based on the *linear potential theory*, an extension of the linear wave theory to the wave-body interaction; they represent over 90% of models used [Folley, 2016]. This group contains:

frequency-domain models, characterized by a fully linear approach; *time-domain models*, that permit a complete description of the WECs dynamics; *spectral-domain linearisation models*, based on a statistical approach to the device response; harmonic-balance models, that permit to take into account some non-linearities in the frequency-domain. The third group consists of those models that are based on the *non-linear potential flow theory*: they are suitable for particularly powerful sea conditions, and also for studying the survivability of the devices. Finally, *system identification models* describe WECs starting from input/output data. In the following paragraphs we will briefly explain the characteristics of the listed methods, with a focus to the advantages and disadvantages of each of them. It is important to mention how an additional field of study consists in the analysis of groups of WECs, whose interactions can strongly influence their functioning.

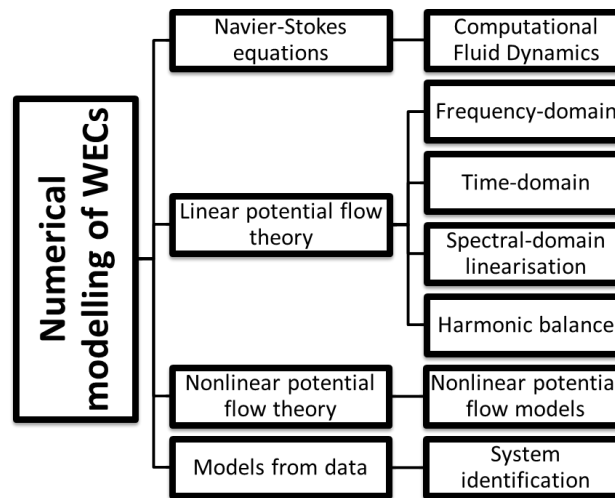


Figure 1.22: Main available numerical models for wave energy converters.

Computational fluid dynamics

CFD methods numerically solve the Navier-Stokes equations, that describe the macroscopic behaviour of a fluid in terms of transfer of mass, momentum and heat. The solution, i.e. pressure and velocity fields, is given at discrete points in space and time. CFD methods are fully non-linear, thus permit to include all the non-linear effects, both from the incoming wave and the wave-body interaction. There are two categories of CFD methods: *Eulerian*, in which the spatial domain is made of a finite set of points (the so called *mesh*), and *Lagrangian*, where the computational region is discretized by a set of particles moving at the same flow velocity [Folley, 2016]. For the former, the most largely used approach in WECs modelling is the *finite volumes*; an example of the latter is the *Smoothed-Particle Hydrodynamics* (SPH) method. Despite the precision of the results provided by CFD methods, their main limitation is related to computational time. Many advanced codes need time steps in the order of microseconds to avoid stability problems: this makes impracticable simulation times longer than some seconds [Folley, 2016]. Thanks to the significant improvement of the performance of computer hardware, CFD methods can be used to partially substitute experimental tests in the process for reaching optimal WEC designs [Penalba et al., 2017].

Linear potential flow theory

Potential flow theory permits to study wave-body interactions describing the velocity flow of an inviscid fluid as the gradient of the velocity potential; the linear potential flow model assumes also that the flow is irrotational and incompressible, as reported in Section 1.1.1. Furthermore, hypothesis for the wave-body interaction are that the body is stiff, it has zero forward motion and it follows small amplitudes with respect to its equilibrium position. The potential associated to the incident flow can be split into three parts: the undisturbed potential (due to the wave motion in absence of the body), the diffracted potential (related to the wave alteration due to the presence of the body) and the radiated potential (due to the oscillation of the body in still water). There is also a potential associated to the restoring forces acting on a static body in still water. The linearity hypothesis permits to simply sum up the different components.

Frequency-domain models

Frequency-domain models are the most simplified amongst the linear potential flow theory; in addition to the linearity in the hydrodynamic description, they also need a linear representation of reactive forces, mainly moorings and power take-off systems. This permits to apply the superposition principle: the response caused by many harmonic stimuli is just the algebraic sum of the responses caused by every stimulus [Folley, 2016]. The models in frequency-domain thus make use of matrices which give information about the response of the analysed floater under a wide finite range of frequencies of the incoming wave; these data can be obtained from *Boundary Element Method* (BEM) codes (e.g. WAMIT, ANSYS-AQWA). Once these data are available, the solution of the problem is straightforward, both from a theoretical and numerical point of view. Because of their limitation to strictly linear problems, frequency-domain models have limited applicability, mainly to small amplitude oscillations: energetic sea states and response to frequencies close to the resonance one are often poorly described. Also, because of the inviscid fluid assumption, non-linear viscous effects can't be taken into account. Furthermore, as the results are translated from the frequency-domain to the time-domain only at the end of the whole computation, controllability can't be studied at all in frequency-domain, as it needs for real-time results. However, frequency-domain models have the advantage to be the fastest in terms of computational time: thus, they can be suitable for optimization of some long term parameters or for an estimate of the yearly producible energy in a certain location.

Time-domain models

Time-domain numerical techniques for WECs are based on the equation proposed by Cummins in 1962, that allowed for the first time to compute in a deterministic way the dynamics of floating bodies out of the frequency-domain. In particular, Cummins showed that the frequency dependence of some terms describing the motion of floaters could be taken into account through a convolution term in the motion equation [Cummins, 1962]; the starting point are still the data from Boundary Elements Method codes. Time-domain models permit to describe non-linearities of the PTO and any other system used for the energy extraction; they also allow to consider and simulate real-time control strategies, which are of central importance for the dynamics of wave energy converters. Although based on the linear potential flow theory, and thus on the inviscid fluid hypothesis, time-domain models allow to include

externally some viscous effects; the Morison equation for a quadratic viscous term is an example [Penalba et al., 2017]. The calculation of the radiation convolution term is often too computationally demanding; it can be effectively substituted by a state space representation, that can reduce the computational time by 20 to 80 times. Time-domain models can be applied to any sort of systems, but nevertheless have some intrinsic limitations. First of all, the state-space modelling of hydrodynamics is an idealization, that can be more or less accurate depending on several factors. Other sources of inaccuracies can come from the number of frequency components chosen and the discretization in the numerical integration [Folley, 2016]. Furthermore, working in time-domain can require relatively high computational resources, especially when dealing with many degrees of freedom. This aspect should also be considered keeping in mind that ocean waves have a random nature, as for a certain wave spectrum there are infinite wave elevation time series: if we're interested in macro parameters, as the average power absorbed, a long simulation time or a high number of shorter simulations are needed.

Spectral-domain linearisation

The spectral domain makes use of a probabilistic model of the systems dynamics: starting from a statistical representation of waves it gives information concerning the statistical response of the device, e.g. in terms of average power capture or produced power [Folley, 2016]. The statistical representation of waves is reasonably given by their energy spectrum; a further assumption is that there's a random phase relationship between the wave components, that leads to represent the wave phenomena as a Gaussian process. Spectral-domain linearisation permits, on the assumptions of a Gaussian sea, to represent a linear system equivalent to the non-linear one under study through an iterative process; the solution is then simply obtained in the frequency-domain. The model has for the first time been applied to WECs in [Folley and Whittaker, 2010] and produced a statistically similar response to the one of time-domain models for different WECs and non-linearity sources; it demonstrated great computational efficiency compared to time-domain models. The main limitation of spectral-domain models is the impossibility of describing any temporal response, thus it can't describe the control of the devices. Furthermore, the statistical linearisation of non-linear forces requires that those forces are differentiable, in order to obtain a quasilinear coefficient [Folley, 2016]. Concluding, a Gaussian response of the device is the hypothesis on which the model is built: as the influence of non-linear forces becomes greater, the response is less likely to be Gaussian. Spectral-domain linearisation is a quite recent research theme in the wave energy field: further developments are expected for the following years.

Harmonic balance

Harmonic balance (HB) is the most recent amongst the methods for modelling WECs based on the linear wave theory; it has been applied in the wave energy field for the first time in [Mérigaud and Ringwood, 2018b], where it was termed *non-linear frequency-domain* approach. The method is based on the projection of the system inputs and outputs onto a Fourier basis, i.e. a sum of harmonic sinusoids. By separating the linear terms from the non-linear ones, the method is able to efficiently solve the problem in the frequency-domain, while keeping the description of the non-linear terms effects. The set of non-linear equations describing the WECs dynamics is then solved making use of a suitable algorithm; computational efficiency is enforced by the use of explicit Jacobian computation. The approach

has shown to be successfully applicable to simulation of WECs with high non-linearities, maintaining most of the computational benefits given by the classic frequency-domain approach and not requiring any approximation of the linear radiation forces [Mérigaud and Ringwood, 2018b]. However, the main limitations lie in the impossibility of representing real-time control loops, especially when particular constraints must be taken into account. Because of its characteristics, some important application fields could be the optimization of long-term control parameters and the power production assessment, as a potentially more reliable alternative to power matrices [Mérigaud and Ringwood, 2018a].

Non-linear potential flow models

Until recently, many WEC projects did not overcome the stage of early design and deployment, and therefore few projects could boast small prototypes tested at sea [Folley, 2016]. Recent years have seen several projects reaching the small-scale prototype deployment, and thus the survivability of the devices in highly energetic sea-states has become increasingly important. For this reason, the interest in tools capable of describing wave-floater interaction in steep sea-states has progressively increased, going in two main directions: on one hand large viscous waves implications on WECs can be accurately described by computational fluid dynamic models, whose limitations have already been exposed; on the other, non-linear potential flow models can describe large body motions with the hypothesis of inviscid fluid at a computational cost lower than those of CFD models. Non-linear potential flow models can be classified in weakly non-linear and fully non-linear whether or not there's an approximation of the formulation. The velocity potential and other quantities of interest are expressed as perturbation series with respect to the wave steepness, while boundary conditions are written according to their Taylor expansion. Higher degrees of steepness are analysed using as input the results for lower steepness [Penalba et al., 2017]; the solution is looked for in the time-domain. Non-linear potential flow models have been validated on both OWCs [Koo and Kim, 2010] and floating devices, with a particular glance at the comparison of weakly and fully non-linear models [Letournel et al., 2014]. Main limitations of these models are in the absence of viscous effects, that can be relevant and beneficial for floating devices survivability; addition of Morison-type external viscosity can partially overcome this drawback.

System identification

The last group of models for WECs we'll present involves a different approach to what has been presented so far; its origins are recent, dating back to 2013 [Davidson et al., 2013]. When the analysed system is very complex, it can be useful to base the representative model on available data rather than on the physical process itself; system identification models, starting from available data, make use of statistical methods to build a suitable mathematical model for the device under investigation [Penalba et al., 2017]. Data must be accurate and representative of the system, thus wave tank or numerical wave tank experiments are normally used. Experiments used for generating adequate data can be of different types: from the simple decay test [Davidson et al., 2013] to the experiments with input waves or force [Folley, 2016] or prescribed motion [Davidson et al., 2015]. Then, the structure of the model must be determined, with the largest part of system identification techniques making use of discrete-time models with different orders and non-linear terms [Ljung, 1998]. Finally, parameters must be chosen and identified making use of numerical optimization. Main limitations come from the quantity and quality of

data used for identifying the models: system identification is an advanced technique that somehow leads to their extrapolation and generalization.

Current challenges

We've briefly analysed several different approaches for the modelling of WECs, each having its own advantages and limitations. It does not exist a method that can be considered the best in absolute terms, either because of the wide technological landscape or the different needs at various steps of the development process. Frequency-domain models can be useful at early development stages, while time-domain models can be required when dealing with complex real time control loops. And again, models from data can be useful when dealing with particularly complex systems, non-linear potential flow models when studying reactions to extreme sea states, while spectral-domain models are suitable when studying productivity. As seen, computational fluid dynamics can often be an effective alternative to real experiments, allowing the values of all the exchanged forces to be derived. The continuous increase in computing power is having an impact on the WECs numerical modelling field, by opening the door to more computationally expensive approaches, but also raising the expectation behind the models [Folley and Whittaker, 2010]. This research paper will focus on the harmonic balance approach, that has so far been exclusively applied to one DoF devices. Further considerations on the potentialities and limitations of this method are referred to the conclusions.

ISWEC - Inertial Sea Wave Energy Converter

This chapter provides all information about the ISWEC device needed to understand its working principle and physical model. After a brief introduction on the ISWEC project and the achieved objectives, the device is studied in depth, from the gyroscope mathematical model to the hydrodynamic interaction. Some efforts are then devoted to explain the PTO model, the operational constraints and the control parameters of the WEC. The last section focuses on the existing simulation frameworks of the ISWEC, in order to understand what are the limits and strengths of the numerical simulations of the device which have been used so far.

The information contained herein is mainly derived from [Vissio, 2017] and [Bracco, 2010].

2.1 Structure and working principle

The ISWEC (Inertial Sea Wave Energy Converter) produces energy from sea waves exploiting the gyroscopic effect generated by the combination of the pitch motion and the rotation of a flywheel. It is an offshore, single body, floating WEC. The device consists of a monolithic hull and an inner space completely sealed with respect to the outer sea environment. In the interior there are two gyroscopes, the PTO and the power conditioning system. The device has originally been developed with one gyroscope; the presence of the second one does not change the physics of the device. An electric cable is the only equipment which crosses the hull. The sealing ensures high reliability and low maintainability, with all the most sensitive parts of the device protected from the external environment; this characteristic is an asset of the ISWEC [Vissio, 2017].

The device works aligned with the wavefront direction and the entire floater performs a pitch motion about the pitch axis identified by the angle δ . The flywheel within the gyroscopic frame is kept rotating with spinning velocity $\dot{\varphi}$. The combination of the two motions generates an inertial gyroscopic torque that results in the rotation of the gyroscopic structure about its precession axis ε . On the same shaft are installed the electric motors, that produce electricity braking the rotation motion. Fig. 2.1 gives a complete representation of the device and its rotation angles.

Power absorption occurs through the exchange of torques from the gyroscopic frames to the hull and the waves. The value taken over by the angular momentum exchanged between the hull and the

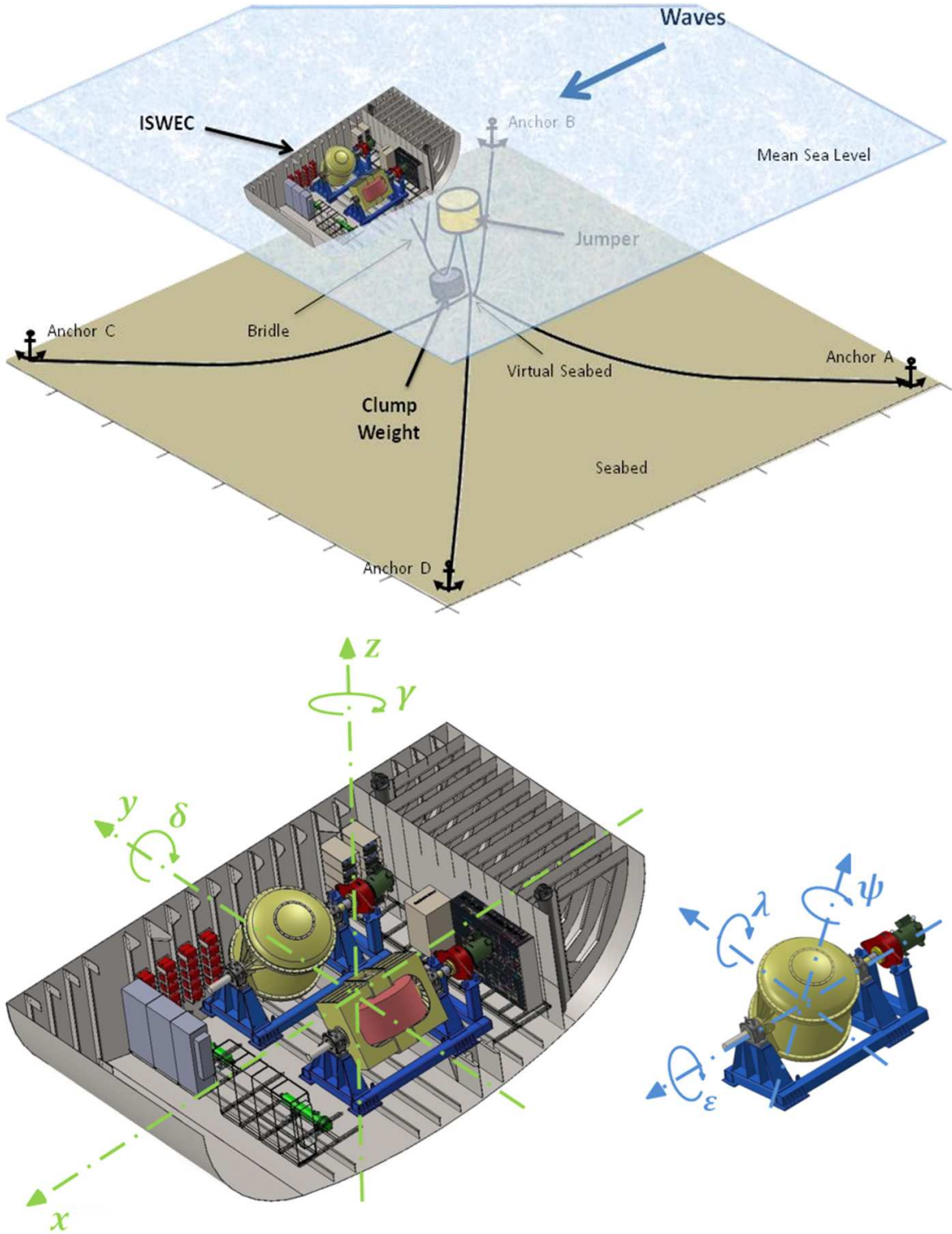


Figure 2.1: ISWEC prototype and installation drawings [Vissio, 2017].

gyroscopic system depends on the flywheel speed, that can be tuned. The natural frequency of the device can thus be modified depending on the sea-state to which the device is exposed. The other control parameters are directly related to the PTO system, and will be better explained below.

The floater has a slack mooring configuration, consisting of a single line with a clump weight and a jumper (See Fig. 2.1). The line is connected to the device through a bridle and to the seabed by mean of four anchors. This configuration permits the hull to passively self-align itself and keep the position with respect to the wavefront direction.

The characteristics of the ISWEC make it particularly suitable to work with waves having large steepness and high frequency, as the ones that can be encountered in enclosed sea environments, e.g. the Mediterranean Sea.

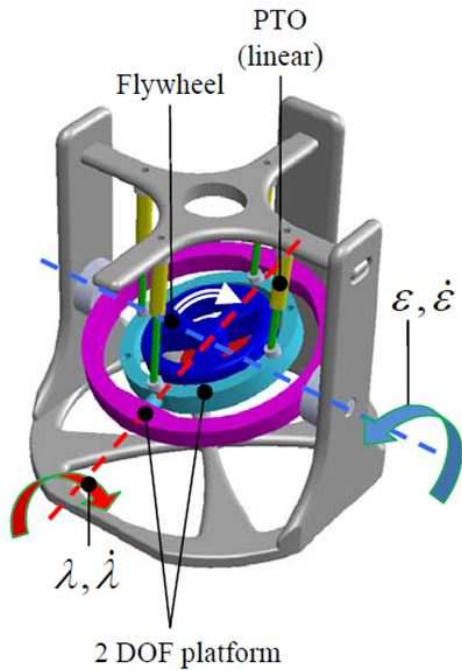


Figure 2.2: Pantelleria (TP, Italy), 2015. ISWEC installed prototype in operation. [Vissio, 2017].

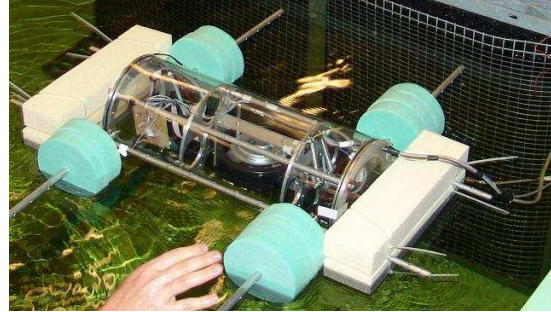
2.2 The ISWEC project: goals and timeline

The first idea of exploiting the gyroscopic effect created by the combination of a hull motion and a flywheel spinning speed to harvest wave energy dates back to 2005. The idea came from the renewable group of the Mechanical and Aerospace Engineering department (DIMEAS) of Politecnico di Torino, in particular from the work of the engineers Giuliana Mattiazzo and Ermanno Giorcelli. The first concept had a 2 DoF gyroscope system, as reported in Fig. 2.3a. A first proof of concept was developed in 2007, and tested at Politecnico di Torino. The tests led to the simplification of the overall system and the internal gyroscope lost one DoF, keeping the only precession motion; since that moment, the PTO system has been installed on the same oscillating shaft of the gyroscope frame.

A complete and structured research program was developed, following the guidelines and evaluations protocols for wave power by HMRC [Holmes, 2003]. In 2009 the first prototype of the ISWEC was developed: it was a 1:45 scaled device which can be observed in Fig. 2.3b. The prototype was tested at Politecnico di Torino and University of Edinburgh. Results were used to hypothesize some arrangements and system configurations, but also to validate the mathematical and numerical models. Nevertheless, some phenomena can't be scaled and could not be studied, mainly the friction and the aerodynamic



(a) ISWEC first concept - 2 DoF gyroscopic system.



(b) ISWEC prototype - 1:45 scale.

Figure 2.3: First steps of the ISWEC device development [Vissio, 2017].

losses.

The following step consisted in the design and realisation of a bigger scale prototype: this was performed thanks to an Italian Regional funding related to the SPOS-DET project in 2009. In the meanwhile, two other important events marked the history of the ISWEC project. The first one is the choice of the design location, which was made on Pantelleria island (TP, Italy); a data harvesting campaign from January 2010 to December 2011 permitted to obtain the occurrences scatter table for the location. The second one is the founding of the university spin-off "Wave for Energy S.r.l.", with the aim of realising and commercialising the ISWEC device. A 1:8 scaled prototype was assembled and tested in 2012 at INSEAN wave tank in Rome, which permitted to assess the hull hydrodynamic conversion capabilities and the estimation of the electro-mechanical power losses [Vissio, 2017].

In 2012 a public structure related to Regione Piemonte funded the development of a full scale 60kW prototype of the ISWEC device to be installed in the Pantelleria site. The main aim was to demonstrate the power production capabilities of the WEC. The design and optimization of the device has been carried out up to 2014 and is exhaustively described in [Raffero, 2014]. The device was concluded in summer 2015, and the experimental campaign started in August 2015 (Fig. 2.2).

2.3 Reference frames

The following Sections will present the analytic model of the ISWEC, covering the two main phenomena involved in the power conversion, i.e. the gyroscope system and the hydrodynamic interaction. Therefore, it is necessary to define some reference frames that permit us to write down the equations governing the device motion. The reference figure is Fig. 2.4, where the main components of the gyroscopic system can be identified: the PTO system in green, the flywheel in red and the gyroscopic structure in

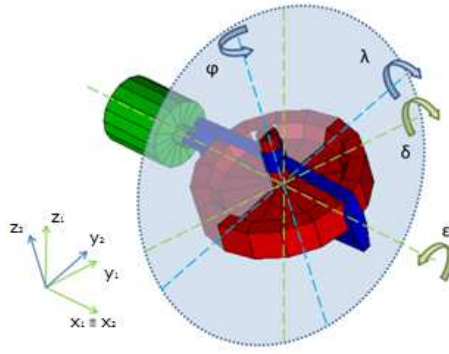


Figure 2.4: The FCS and GCS coordinate systems [Raffero, 2014].

blue.

The reference frames are defined as follows [Vissio, 2017]:

- ECS: earth-fixed coordinate system (x_0, y_0, z_0) .
- FCS: floater-fixed coordinate system (x_1, y_1, z_1) .
- GCS: gyroscopic structure-fixed coordinate system (x_2, y_2, z_2) .

Some important remarks also need to be done:

- ECS and FCS have the same origin, in the center of gravity of the system.
- The x_1 and x_2 axes coincide, as shown in Fig. 2.4.

Tables 2.1 and 2.2 show the DoF and the variables related to, respectively, the FCs and the GCS. In particular, the rotation around the y_1 axis is the pitch (δ), that is the main motion generated by the floater-wave interaction. Concerning the gyroscope not all the DoF are free as the gyroscope structure is fixed to the hull; the rotation around the precession axis $x_2 \parallel x_1$ is named ϵ . The flywheel is free to rotate around the z_2 axis with set speed $\dot{\varphi}$, thus resulting in an additional DoF of the system.

Table 2.1: Hull-fixed FCS notation [Vissio, 2017].

DOF	Name	Comment	Symbol
1	surge	motions in the x_1 -direction	x
2	sway	motions in the y_1 -direction	y
3	heave	motions in the z_1 -direction	z
4	roll	rotations about the x_1 -axis	r_x
5	pitch	rotations about the y_1 -axis	r_y, δ
6	yaw	rotations about the z_1 -axis	r_z, γ

2.4 Gyroscope mathematical model

The gyroscopic system is the most important feature of the ISWEC and represents the mean by which the kinetic energy of the floater becomes mechanical energy on the PTO axis. This Section presents the system of equations that describe the dynamic behaviour of the gyroscopic system. For further details please refer to [Raffero, 2014].

Table 2.2: Gyroscope structure-fixed GCS notation [Vissio, 2017].

DOF	Name	Comment	Symbol
1	-	$x_2 \parallel x_1$	-
2	-	-	-
3	-	-	-
4	precession axis	rotations about x_2 -axis	ε
5	-	rotations about y_2 -axis	λ
6	-	rotations about the z_2 -axis	ψ

2.4.1 Physical equations for the gyroscope

The whole analysis is carried out with a Newtonian approach. Starting from the Newton's Second Law, we aim at evaluating the mechanical momentum generated on the centre of gravity of the system by the variation in time of the angular momentum. The angular momentum conservation theorem can be expressed as:

$$\vec{M}_E = -\frac{d\vec{L}}{dt} = \sum_{i=0}^N \vec{T}_{E,i} \quad (2.4.1)$$

which shows that the angular momentum variation in time is equal to the external generalised forces acting on the system.

We can write the angular velocities of the GCS and the flywheel, respectively $\vec{\omega}_{GCS}$ and $\vec{\omega}_{fw}$, in GCS as:

$$\vec{\omega}_{GCS} = \dot{\varepsilon}\hat{i}_2 + \dot{\lambda}\hat{j}_2 + \dot{\psi}\hat{k}_2 \quad (2.4.2)$$

$$\vec{\omega}_{fw} = \vec{\omega}_{GCS} + \dot{\varphi}\hat{k}_2 = \dot{\varepsilon}\hat{i}_2 + \dot{\lambda}\hat{j}_2 + (\dot{\varphi} + \dot{\psi})\hat{k}_2 \quad (2.4.3)$$

where $\hat{i}_2, \hat{j}_2, \hat{k}_2$ are the three GCS mutually orthogonal unit versors, while the other quantities have been defined in Section 2.3. Then, the flywheel angular momentum is equal to:

$$\vec{L}_{fw} = \hat{I}_{fw} \cdot \vec{\omega}_{fw} \quad (2.4.4)$$

As GCS is constituted by principal axes of inertia, the inertia tensor of the flywheel can be written as:

$$\hat{I}_{fw} = \begin{pmatrix} I_{fw} & 0 & 0 \\ 0 & I_{fw} & 0 \\ 0 & 0 & J \end{pmatrix} \quad (2.4.5)$$

where J is the flywheel moment of inertia around its axis, while I_{fw} is its moment of inertia around any axis perpendicular to the first one [Raffero, 2014]. Merging Eqs. (2.4.3), (2.4.4) and (2.4.5), we obtain:

$$\vec{L}_{fw} = I_{fw}\dot{\varepsilon}\hat{i}_2 + I_{fw}\dot{\lambda}\hat{j}_2 + J(\dot{\varphi} + \dot{\psi})\hat{k}_2 \quad (2.4.6)$$

In order to apply Eq. (2.4.1), we need to remember that the time derivative of a versor is equal to the

cross product of the angular speed of that versor by itself. Thus:

$$\frac{d\hat{i}_2}{dt} = \vec{\omega}_{GCS} \times \hat{i}_2 = -\lambda\hat{k}_2 + \psi\hat{j}_2 \quad (2.4.7)$$

$$\frac{d\hat{j}_2}{dt} = \vec{\omega}_{GCS} \times \hat{j}_2 = \epsilon\hat{k}_2 - \psi\hat{i}_2 \quad (2.4.8)$$

$$\frac{d\hat{k}_2}{dt} = \vec{\omega}_{GCS} \times \hat{k}_2 = -\epsilon\hat{j}_2 + \lambda\hat{i}_2 \quad (2.4.9)$$

We can now use the angular momentum conservation theorem to give an expression of the external generalised forces applied to the flywheel:

$$\begin{aligned} \vec{M}_{Efw} = & I_{fw}\ddot{\epsilon}\hat{i}_2 + I_{fw}\dot{\epsilon}(\psi\hat{j}_2 - \lambda\hat{k}_2) + I_{fw}\ddot{\lambda}\hat{j}_2 + I_{fw}\dot{\lambda}(\epsilon\hat{k}_2 - \psi\hat{i}_2) + \\ & + J(\ddot{\varphi} + \ddot{\psi})\hat{k}_2 + J(\dot{\varphi} + \dot{\psi})(\lambda\hat{i}_2 - \epsilon\hat{j}_2) \end{aligned} \quad (2.4.10)$$

The scalar components of the external forces in GCS are:

$$M_{Efw,x_2} = \vec{M}_E \cdot \hat{i}_2 = I_{fw}\ddot{\epsilon} + (J - I_{fw})\dot{\lambda}\dot{\psi} + J\dot{\varphi}\dot{\lambda} \quad (2.4.11)$$

$$M_{Efw,y_2} = \vec{M}_E \cdot \hat{j}_2 = I_{fw}\ddot{\lambda} - (J - I_{fw})\dot{\epsilon}\dot{\psi} - J\dot{\varphi}\dot{\epsilon} \quad (2.4.12)$$

$$M_{Efw,z_2} = \vec{M}_E \cdot \hat{k}_2 = J(\ddot{\varphi} + \ddot{\psi}) \quad (2.4.13)$$

2.4.2 Gyroscope equations in hull reference frame

As later it will be necessary to pair the hull and gyroscopic models, it is useful to rewrite the gyroscope model in FCS. The $\dot{\delta}$ and $\dot{\psi}$ velocities are related to the speed on the pitch rotation $\dot{\delta}$ as:

$$\dot{\lambda} = \dot{\delta} \cos \epsilon \quad (2.4.14)$$

$$\dot{\psi} = -\dot{\delta} \sin \epsilon \quad (2.4.15)$$

while for the acceleration it is:

$$\ddot{\lambda} = \ddot{\delta} \cos \epsilon - \dot{\delta} \dot{\epsilon} \sin \epsilon \quad (2.4.16)$$

$$\ddot{\psi} = -\ddot{\delta} \sin \epsilon - \dot{\delta} \dot{\epsilon} \cos \epsilon \quad (2.4.17)$$

Using the above relations within Eqs. (2.4.11) to (2.4.13) we obtain the following equations, still in GCS:

$$M_{Efw,x_2} = I_{fw}\ddot{\epsilon} - (J - I_{fw})\dot{\delta}^2 \sin \epsilon \cos \epsilon + J\dot{\varphi}\dot{\delta} \cos \epsilon \quad (2.4.18)$$

$$M_{Efw,y_2} = I_{fw}\ddot{\delta} \cos \epsilon + (J - 2I_{fw})\dot{\delta}\dot{\epsilon} \sin \epsilon - J\dot{\varphi}\dot{\epsilon} \quad (2.4.19)$$

$$M_{Efw,z_2} = J\ddot{\varphi} - J\ddot{\delta} \sin \epsilon - J\dot{\delta}\dot{\epsilon} \cos \epsilon \quad (2.4.20)$$

The equations for the external torques in FCS can be obtained doing the dot product of \vec{M}_E by the FCS versors $\hat{i}_1, \hat{j}_1, \hat{k}_1$. We obtain:

$$M_{Efw,x_1} = \vec{M}_E \cdot \hat{i}_1 = \vec{M}_E \cdot \hat{i}_2 = M_{E,x_2} = \quad (2.4.21)$$

$$I_{fw}\ddot{\varepsilon} - (J - I_{fw})\delta^2 \sin \varepsilon \cos \varepsilon + J\dot{\varphi}\dot{\delta} \cos \varepsilon$$

$$M_{Efw,y_1} = \vec{M}_E \cdot \hat{j}_1 = \quad (2.4.22)$$

$$(I_{fw} \cos^2 \varepsilon + J \sin^2 \varepsilon)\ddot{\delta} + 2(J - I_{fw})\dot{\delta}\dot{\varepsilon} \sin \varepsilon \cos \varepsilon - J\dot{\varphi}\dot{\varepsilon} \cos \varepsilon - J\ddot{\varphi} \sin \varepsilon$$

$$M_{Efw,z_1} = \vec{M}_E \cdot \hat{k}_1 = \quad (2.4.23)$$

$$- (J - I_{fw})\dot{\delta} \sin \varepsilon \cos \varepsilon + [(J - 2I_{fw}) \sin^2 \varepsilon - J \cos^2 \varepsilon]\dot{\delta}\dot{\varepsilon} - J\dot{\varphi}\dot{\varepsilon} \sin \varepsilon + J\ddot{\varphi} \cos \varepsilon$$

The above equations describe the behaviour of the gyroscopic system with respect to the pitch velocity $\dot{\delta}$ and acceleration $\ddot{\delta}$ and the flywheel speed $\dot{\varphi}$ and acceleration $\ddot{\varphi}$.

2.4.3 Gyroscope supporting frame

In order to completely describe the gyroscopic group, also the term related to the gyroscopic structure should be considered. The angular momentum of the gyroscope structure can be written similarly to Eq. (2.4.4):

$$\vec{L}_{gs} = \hat{I}_{gs} \cdot \vec{\omega}_{GCS} \quad (2.4.24)$$

As the reference system GCS is constituted by principal axes of inertia, the inertia tensor of the gyroscopic structure can be written as:

$$\hat{I}_{gs} = \begin{pmatrix} I_{gs,x} & 0 & 0 \\ 0 & I_{gs,y} & 0 \\ 0 & 0 & I_{gs,z} \end{pmatrix} \quad (2.4.25)$$

Let us define the following moments of inertia, obtained adding to the flywheel moments of inertia those of the gyro structure:

$$I_x = I_{gs,x} + I_{fw} \quad (2.4.26)$$

$$I_y = I_{gs,y} + I_{fw} \quad (2.4.27)$$

$$I_z = I_{gs,z} + J \quad (2.4.28)$$

The overall external generalised forces in GCS can be written as:

$$\begin{aligned} \vec{M}_{Etot} = & I_x \dot{\varepsilon} \hat{i}_2 + I_x \dot{\varepsilon} (\dot{\psi} \hat{j}_2 - \dot{\lambda} \hat{k}_2) + I_y \ddot{\lambda} \hat{j}_2 + I_y \dot{\lambda} (\dot{\varepsilon} \hat{k}_2 - \dot{\psi} \hat{i}_2) + \\ & + I_z \ddot{\psi} \hat{k}_2 + I_z \dot{\psi} (\dot{\lambda} \hat{i}_2 - \dot{\varepsilon} \hat{j}_2) + J \ddot{\varphi} \hat{k}_2 + J \dot{\varphi} (\dot{\lambda} \hat{i}_2 - \dot{\varepsilon} \hat{j}_2) \end{aligned} \quad (2.4.29)$$

where the last two terms are due the difference between ω_{GCS} and ω_{fw} , i.e. to rotation of the flywheel around its own axis. The scalar components of the external forces in GCS are:

$$M_{Etot,x2} = I_x \ddot{\epsilon} - I_y \dot{\lambda} \dot{\psi} + I_z \dot{\psi} \dot{\lambda} + J \dot{\phi} \dot{\lambda} = \quad (2.4.30)$$

$$= I_x \ddot{\epsilon} + (I_z - I_y) \dot{\lambda} \dot{\psi} + J \dot{\phi} \dot{\lambda}$$

$$M_{Etot,y2} = I_x \dot{\epsilon} \dot{\psi} + I_y \ddot{\lambda} - I_z \dot{\psi} \dot{\epsilon} - J \dot{\phi} \dot{\epsilon} \quad (2.4.31)$$

$$M_{Etot,z2} = -I_x \dot{\epsilon} \dot{\lambda} + I_y \dot{\lambda} \dot{\epsilon} + I_z \ddot{\psi} + J \ddot{\epsilon} = \quad (2.4.32)$$

$$= (I_y - I_x) \dot{\lambda} \dot{\epsilon} + I_z \ddot{\psi} + J \ddot{\epsilon}$$

Let us now apply Eqs. (2.4.14) to (2.4.17) to the set of equations above, in order to highlight the relations with the pitch and precession motions:

$$M_{Etot,x2} = I_x \ddot{\epsilon} - (I_z - I_y) \delta^2 \sin \epsilon \cos \epsilon + J \dot{\phi} \dot{\delta} \cos \epsilon \quad (2.4.33)$$

$$M_{Etot,y2} = -I_x \dot{\epsilon} \dot{\delta} \sin \epsilon + I_y (\ddot{\delta} \cos \epsilon - \dot{\delta} \dot{\epsilon} \sin \epsilon) + I_z \dot{\delta} \dot{\epsilon} \sin \epsilon - J \dot{\phi} \dot{\delta} \quad (2.4.34)$$

$$M_{Etot,z2} = (I_y - I_x) \dot{\delta} \dot{\epsilon} \cos \epsilon - I_z (\ddot{\delta} \sin \epsilon + \dot{\delta} \dot{\epsilon} \cos \epsilon) + J \ddot{\phi} \quad (2.4.35)$$

The external torques in FCS can be obtained doing the dot product of M_E by the FCS versors $\hat{i}_1, \hat{j}_1, \hat{k}_1$. We obtain:

$$M_{Etot,x1} = \vec{M}_E \cdot \hat{i}_1 = \vec{M}_E \cdot \hat{i}_2 = M_{E,x2} = \quad (2.4.36)$$

$$= I_x \ddot{\epsilon} - (I_z - I_y) \dot{\epsilon}^2 \sin \epsilon \cos \epsilon + J \dot{\phi} \dot{\delta} \cos \epsilon$$

$$M_{Etot,y1} = \vec{M}_E \cdot \hat{j}_1 = \quad (2.4.37)$$

$$= -I_x \dot{\epsilon} \dot{\delta} \sin \epsilon \cos \epsilon + I_y \ddot{\delta} \cos^2 \epsilon - I_y \dot{\delta} \dot{\epsilon} \sin \epsilon \cos \epsilon + I_z \dot{\delta} \dot{\epsilon} \sin \epsilon \cos \epsilon - J \dot{\phi} \dot{\delta} \cos \epsilon +$$

$$- [(I_y - I_x) \dot{\delta} \dot{\epsilon} \cos \epsilon \sin \epsilon + I_z (\ddot{\delta} \sin \epsilon - \dot{\delta} \dot{\epsilon} \cos \epsilon) \sin \epsilon + J \ddot{\phi} \sin \epsilon =$$

$$= -I_x \dot{\epsilon} \dot{\delta} \sin \epsilon \cos \epsilon + I_y \ddot{\delta} \cos^2 \epsilon - I_y \dot{\delta} \dot{\epsilon} \sin \epsilon \cos \epsilon + I_z \dot{\delta} \dot{\epsilon} \sin \epsilon \cos \epsilon +$$

$$- (I_y - I_x) \dot{\delta} \dot{\epsilon} \cos \epsilon \sin \epsilon + I_z (\ddot{\delta} \sin \epsilon + \dot{\delta} \dot{\epsilon} \cos \epsilon) \sin \epsilon - J \ddot{\phi} \sin \epsilon =$$

$$= (-I_x - I_y + I_z - I_y + I_x + I_z) \dot{\delta} \dot{\epsilon} \sin \epsilon \cos \epsilon + I_y \ddot{\delta} \cos^2 \epsilon + I_z \ddot{\delta} \sin^2 \epsilon - J \dot{\phi} \dot{\delta} \cos \epsilon - J \ddot{\phi} \sin \epsilon =$$

$$= 2(I_z - I_y) \dot{\delta} \dot{\epsilon} \sin \epsilon \cos \epsilon + I_y \ddot{\delta} \cos^2 \epsilon + I_z \ddot{\delta} \sin^2 \epsilon - J \dot{\phi} \dot{\delta} \cos \epsilon - J \ddot{\phi} \sin \epsilon$$

$$M_{Etot,z1} = \vec{M}_E \cdot \hat{k}_1 = \quad (2.4.38)$$

$$- I_x \dot{\epsilon} \dot{\delta} \sin^2 \epsilon + I_y \dot{\delta} \sin \epsilon \cos \epsilon - I_y \dot{\delta} \dot{\epsilon} \sin^2 \epsilon + I_z \dot{\delta} \dot{\epsilon} \sin^2 \epsilon - J \dot{\phi} \dot{\delta} \sin \epsilon + (I_y - I_x) \dot{\delta} \dot{\epsilon} \cos^2 \epsilon +$$

$$+ I_z (-\ddot{\delta} \sin \epsilon \cos \epsilon - \dot{\delta} \dot{\epsilon} \cos^2 \epsilon) + J \ddot{\phi} \cos \epsilon =$$

$$= (-I_x - I_y + I_z) \dot{\delta} \dot{\epsilon} \sin^2 \epsilon + (I_y - I_z) \dot{\delta} \sin \epsilon \cos \epsilon - J \dot{\phi} \dot{\delta} \sin \epsilon + (I_y - I_x - I_z) \dot{\delta} \dot{\epsilon} \cos^2 \epsilon + J \ddot{\phi} \cos \epsilon$$

2.4.4 Equations simplification

The above equations can be simplified on the basis of some reasonable assumptions. The first one concerns the moments of inertia of the whole gyroscopic system about the different axis. The flywheel moments of inertia J and I_{fw} have the same order of magnitude and are often quite similar, also because of the contribute of the support shafts to the terms I_{fw} [Raffero, 2014]; let us then suppose that $I_x \cong I_y \cong$

$I_z = I$. From Eqs. (2.4.33) to (2.4.35) in GCS we get in GCS:

$$M_{Etot,x2} = I\ddot{\varepsilon} + J\dot{\varphi}\dot{\delta} \cos \varepsilon \quad (2.4.39)$$

$$M_{Etot,y2} = -I\dot{\varepsilon}\dot{\delta} \sin \varepsilon + I\ddot{\delta} \cos \varepsilon - J\dot{\varphi}\dot{\varepsilon} \quad (2.4.40)$$

$$M_{Etot,z2} = -I(\ddot{\delta} \sin \varepsilon + \dot{\delta}\dot{\varepsilon} \cos \varepsilon) + J\ddot{\varphi} \quad (2.4.41)$$

On the other side, from Eqs. (2.4.36) to (2.4.38) in FCS we obtain:

$$M_{Etot,x1} = I\ddot{\varepsilon} + J\dot{\varphi}\dot{\delta} \cos \varepsilon \quad (2.4.42)$$

$$\begin{aligned} M_{Etot,y1} &= I\ddot{\delta} \cos^2 \varepsilon + I\ddot{\delta} \sin^2 \varepsilon - J\dot{\varphi}\dot{\varepsilon} \cos \varepsilon - J\ddot{\varphi} \sin \varepsilon = \\ &= I\ddot{\delta} - J\dot{\varphi}\dot{\varepsilon} \cos \varepsilon - J\ddot{\varphi} \sin \varepsilon \end{aligned} \quad (2.4.43)$$

$$M_{Etot,z1} = I\dot{\delta}\dot{\varepsilon} \sin^2 \varepsilon - J\dot{\varphi}\dot{\varepsilon} \sin \varepsilon - I\dot{\delta}\dot{\varepsilon} \cos^2 \varepsilon + J\ddot{\varphi} \cos \varepsilon \quad (2.4.44)$$

Some other engineering considerations related to the magnitude of the main variables are the following:

- **Wave frequency:** the wave period T_w to which the device is exposed can range from 0.5 to 20 s. It thus leads to a wave frequency ω_w from 12.5 to 0.3 rad/s.
- **Oscillation angles:** the oscillation angles depend on the wave characteristics and the values assumed by the control parameters. However, we can assume the following maximum values:
 - pitch angle: $\delta_{max} = 20 \text{ deg} = 0.349 \text{ rad}$.
 - precession angle: $\varepsilon_{max} = 90 \text{ deg} = 1.571 \text{ rad}$.
- **Velocity and acceleration:** from the previous defined quantities we can estimate the maximum speeds and accelerations:
 - pitch velocity: $\dot{\delta}_{max} = \omega_w \delta_{max} \cong 4.4 \div 0.1 \text{ rad/s}$.
 - pitch acceleration: $\ddot{\delta}_{max} = \omega_w^2 \delta_{max} \cong 54.5 \div 0.03 \text{ rad/s}^2$.
 - precession velocity: $\dot{\varepsilon}_{max} = \omega_w \varepsilon_{max} \cong 19.6 \div 0.47 \text{ rad/s}$.
 - precession acceleration: $\ddot{\varepsilon}_{max} = \omega_w^2 \varepsilon_{max} \cong 245.5 \div 0.14 \text{ rad/s}^2$.

Moreover, also the flywheel should be considered: its speed is normally constant, and thus we have:

$$\text{– flywheel velocity: } \dot{\varphi}_{max} \cong 500 \div 10 \text{ rad/s.}$$

$$\text{– flywheel acceleration: } \ddot{\varphi} \cong 0 \text{ rad/s}^2.$$

All these considerations lead to the simplified form of the sets of Eqs (2.4.33) to (2.4.35) and (2.4.42) to (2.4.44). The terms containing $\ddot{\varphi}$, those containing $\ddot{\delta}$ and those containing $\dot{\delta}\dot{\varepsilon}$ have been removed because of their lower order of magnitudes with respect to the other terms in the same equations. In GCS we have:

$$M_{Etot,x2} = I\ddot{\varepsilon} + J\dot{\varphi}\dot{\delta} \cos \varepsilon \quad (2.4.45)$$

$$M_{Etot,y2} = -J\dot{\varphi}\dot{\varepsilon} \quad (2.4.46)$$

$$M_{Etot,z2} = -I(\dot{\delta} \sin \varepsilon + \dot{\delta}\dot{\varepsilon} \cos \varepsilon) \quad (2.4.47)$$

where the sum of the external forces on the z_2 -axis is orders of magnitude smaller than the other components. In FCS it is:

$$M_{Etot,x1} = I\ddot{\varepsilon} + J\dot{\varphi}\dot{\delta} \cos \varepsilon \quad (2.4.48)$$

$$M_{Etot,y1} = -J\dot{\varphi}\dot{\varepsilon} \cos \varepsilon \quad (2.4.49)$$

$$M_{Etot,z1} = -J\dot{\varphi}\dot{\varepsilon} \sin \varepsilon \quad (2.4.50)$$

It is useful to define some new variables to refer to the gyroscopic torques [Raffero, 2014]:

$$T_\varepsilon = I\ddot{\varepsilon} + J\dot{\varphi}\dot{\delta} \cos \varepsilon \quad (2.4.51)$$

$$T_\lambda = J\dot{\varphi}\dot{\varepsilon} \quad (2.4.52)$$

$$T_\varphi = I(\ddot{\delta} \sin \varepsilon + \dot{\delta}\dot{\varepsilon} \cos \varepsilon) \quad (2.4.53)$$

where T_ε is the torque on the PTO and T_φ is the torque on the motor driving the flywheel. The torque T_λ on the y_1 -axis can be split into the two terms T_δ and T_γ , representing the torques discharged from the gyroscopic system to the floating body respectively on the pitching and yawing directions:

$$T_\delta = T_\lambda \cos \varepsilon = J\dot{\varphi}\dot{\varepsilon} \cos \varepsilon \quad (2.4.54)$$

$$T_\gamma = T_\lambda \sin \varepsilon = J\dot{\varphi}\dot{\varepsilon} \sin \varepsilon \quad (2.4.55)$$

2.4.5 Linearisation

Eqs. (2.4.48) to (2.4.50) are non-linear and coupled together. The application of some useful mathematical tools, e.g. the analysis in the frequency-domain and the control development, require their linearisation. The result is reported as follows:

$$M_{Etot,x1} = I\ddot{\varepsilon} + J\dot{\varphi}\dot{\delta} \quad (2.4.56)$$

$$M_{Etot,y1} = I\ddot{\delta} - J\dot{\varphi}\dot{\varepsilon} \quad (2.4.57)$$

$$M_{Etot,z1} = -J\dot{\varphi}\dot{\varepsilon} \quad (2.4.58)$$

2.5 Hydrodynamical model

An accurate representation of the wave-hull interaction is essential for a satisfactory description of the energy harvesting and power conversion. However, fluid dynamics phenomena are complex and difficult to be treated, both from an analytical and numerical point of view [Pérez and Fossen, 2008]. The Navier-Stokes equations can be directly solved through numerical methods (CFD), but this approach requires high computational time and power. Another possibility, that as reported in Subsection 1.2.3 is also the most widely used, is the application of the linear potential flow theory. The outcome of this theory is the pressure distribution around the floater in steady-state condition, thus permitting the computation of exchanged forces and torques. The hydrodynamical model of the ISWEC is here presented without considering the reaction given by the gyroscopic system; the two models, together with those of the PTO system, will be joined for the 2 DoF case in Section 2.7.

2.5.1 Assumptions and hydrodynamic actions

The main assumptions of the linear potential flow theory are those written in Subsection 1.1.1, to which we should add some hypotheses concerning the body motion:

- The body is stiff.
- The body has zero or very slow forward motion.
- The body follows small motions with respect to its equilibrium position.

The hydrostatic and hydrodynamic forces acting on the body can be grouped under three main categories [Vissio, 2017]:

- Forces affecting the body in still water:
 - **Hydrostatic restoring force:** contribution of gravity and buoyancy forces with the floater in static condition and with still water surface.
- Forces acting on the oscillating body in still water:
 - **Added mass:** contribution of the acceleration of the fluid around the floater.
 - **Radiation forces:** forces of the waves generated by the hull motion, that are related to the velocity vector of the body.
- Forces acting on the still body under monochromatic waves:
 - **Froude-Krylov forces:** forcing term related to the pressure field generated by the undisturbed waves acting on the body.
 - **Diffraction forces:** forcing term related to the waves diffracted by the body itself.

For each of these forces a certain potential associated with the fluid around the hull can be written [Raffero, 2014]. The different potentials are then simply added thanks to the linearity assumption. BEM codes, as ANSYS-AQWA, permit to calculate the matrices required in the fast-running Cummins lumped parameters equation [Pérez and Fossen, 2008]; those matrices describe the terms of added mass, radiation, Froude-Krylov and diffraction potential forces at different frequencies of monochromatic incoming waves. This approach is at the basis of the hydrodynamic modelling of the ISWEC device.

2.5.2 Frequency-domain equation

The Cummins equation is a linear time-invariant integro-differential equation [Cummins, 1962]. However, it is here first presented in its frequency-domain version, that is a second order differential equation with frequency-dependent coefficients [Newman, 1977]:

$$[-\omega^2[\mathbf{M} + \mathbf{M}_a(\omega)] + j\omega\mathbf{B}(\omega) + \mathbf{K}]X(\omega) = F_w(\omega) + F_m(\omega) \quad (2.5.1)$$

where:

- $X(\omega) = [x, y, z, r_x, r_y, r_z]^T = [surge, sway, heave, rol, pitch, yaw]^T$ is the vector containing the 6 DoF of the floater [6x1].

- \mathbf{M} is the floating body inertia matrix [6x6].
- $\mathbf{M}_a(\omega)$ is the frequency dependent added mass matrix [6x6].
- $\mathbf{B}(\omega)$ is the frequency dependent radiation matrix, also called damping matrix [6x6].
- \mathbf{K} is the hydrostatic stiffness matrix, accounting for hydrostatic restoring forces [6x6].
- $F_w(\omega)$ is the frequency-dependent wave force vector [6x1], accounting for both Froude-Krylov and diffraction forces.
- $F_m(\omega)$ are the mooring line actions [6x1].

Coefficients description

The matrices in the equation above depend either on the wave frequency and the direction of the incoming waves. Concerning the ISWEC, it should be remembered that the device is able to passively align itself with the incoming wave front direction. In the following lines the single components of Eq. (2.5.1) for the ISWEC are explained; the contents of the following lines are mostly taken from [Raffero, 2014].

- The inertia matrix \mathbf{M} is composed by the mass of the body in the first three diagonal entries. The fourth quarter of the matrix is instead the inertia tensor of the whole device; non-diagonal terms are zero if the principal axes of inertia are used as reference frame. The distance between the center of mass and the center of buoyancy of the device is written as d_{gb} . The entries of the inertia matrix are non frequency-dependent.

$$\mathbf{M} = \begin{pmatrix} m & 0 & 0 & 0 & md_{gb} & 0 \\ 0 & m & 0 & -md_{gb} & 0 & 0 \\ 0 & 0 & m & 0 & 0 & 0 \\ 0 & -md_{gb} & 0 & I_{xx} & I_{xy} & I_{xz} \\ md_{gb} & 0 & 0 & I_{yx} & I_{yy} & I_{yz} \\ 0 & 0 & 0 & I_{zx} & I_{zy} & I_{zz} \end{pmatrix} \quad (2.5.2)$$

- The hydrostatic stiffness matrix \mathbf{K} is constant for different wave frequencies and directions. Surge, sway and yaw entries are null - and this is the reason why there's need for mooring lines.

$$\mathbf{K} = \begin{pmatrix} 0 & & & & & 0 \\ & 0 & & & & \\ & & K_{33} & & & \\ & & & K_{44} & & \\ & & & & K_{55} & \\ 0 & & & & & 0 \end{pmatrix} \quad (2.5.3)$$

- The added mass matrix $\mathbf{M}_a(\omega)$ highlights the coupling between some DoF: sway is coupled with roll, while surge is coupled with pitch. The latter coupling has some significant effects on the power

production. All the entries are frequency dependent.

$$\mathbf{M}_a(\omega) = \begin{pmatrix} A_{11}(\omega) & 0 & 0 & 0 & A_{15}(\omega) & 0 \\ 0 & A_{22}(\omega) & 0 & A_{42}(\omega) & 0 & 0 \\ 0 & 0 & A_{33}(\omega) & 0 & 0 & 0 \\ 0 & A_{24}(\omega) & 0 & A_{44}(\omega) & 0 & 0 \\ A_{51}(\omega) & 0 & 0 & 0 & A_{55}(\omega) & 0 \\ 0 & 0 & 0 & 0 & 0 & A_{66}(\omega) \end{pmatrix} \quad (2.5.4)$$

- The radiation matrix $\mathbf{B}(\omega)$ has non-null entries in the same position of the added mass matrix. Also its terms are all frequency dependent.

$$\mathbf{B}(\omega) = \begin{pmatrix} B_{11}(\omega) & 0 & 0 & 0 & B_{15}(\omega) & 0 \\ 0 & B_{22}(\omega) & 0 & B_{42}(\omega) & 0 & 0 \\ 0 & 0 & B_{33}(\omega) & 0 & 0 & 0 \\ 0 & B_{24}(\omega) & 0 & B_{44}(\omega) & 0 & 0 \\ B_{51}(\omega) & 0 & 0 & 0 & B_{55}(\omega) & 0 \\ 0 & 0 & 0 & 0 & 0 & B_{66}(\omega) \end{pmatrix} \quad (2.5.5)$$

- The wave excitation force vector $F_w(\omega)$ is obtained multiplying the wave amplitude by the force coefficient vector, obtained by a BEM software as all the other matrices. Those coefficients are complex numbers: their magnitude describes the force amplitude per wave amplitude, while their angle indicates the phase of the force with respect to the water surface elevation. The excitation forces are non-null for the surge, heave and pitch DoF; for all the other DoF the structure of the floater makes the excitation forces negligible.

$$F_w(\omega) = a_w \begin{pmatrix} f_1(\omega)e^{j\omega+\Phi_1} \\ \sim 0 \\ f_2(\omega)e^{j\omega+\Phi_2} \\ \sim 0 \\ f_3(\omega)e^{j\omega+\Phi_3} \\ \sim 0 \end{pmatrix} \quad (2.5.6)$$

For what concerns the mooring terms, please refer to [Vissio, 2017]. $F_m(\omega)$ is a non-linear static term function of the floater motion, that can be linearised for applications in frequency-domain. Also, it is possible to add the influence of mean drift forces within Eq. (2.5.1), which describe the interaction of waves and mooring systems and are obtained from 2nd order approximation of the potential [Vissio, 2017].

2.5.3 Time-domain equation

The Cummins equation in time-domain is an integro-differential equation with a convolution integral describing the memory effects associated to the radiation forces. It is presented as a matrix equation:

$$(\mathbf{M} + \mathbf{M}_{a_\infty})\ddot{\mathbf{X}} + \int_0^t \mathbf{h}_r(t - \tau)\dot{\mathbf{X}}d\tau + \mathbf{K}\mathbf{X} = F_w(t) + F_m(t) \quad (2.5.7)$$

where:

- $\mathbf{X}(t) = [x, y, z, r_x, r_y, r_z]^T = [\text{surge}, \text{sway}, \text{heave}, \text{roll}, \text{pitch}, \text{yaw}]^T$ is the vector containing the 6 DoF of the floater [6x1].
- \mathbf{M} is the floating body inertia matrix [6x6].
- \mathbf{M}_{a_∞} is the infinite frequency added mass matrix [6x6].
- $\mathbf{h}_r(t)$ is the impulse response function for the 6 DoF [6x6].
- \mathbf{K} is the hydrostatic stiffness matrix [6x6].
- $F_w(t)$ is the wave force vector [6x1].
- $F_m(t)$ is the mooring line action [6x1].

It should be also highlighted that Eq. (2.5.7) can contain non-linearities, thus more realistic external forces can be applied if necessary; some examples are viscous drag terms and reactions from the internal systems. The terms of added mass and radiation forces should be analysed more in deep, because of their relationships with the frequency-domain parameters and because of the computational burden brought by the integral in Eq. (2.5.7).

Added mass and radiation forces

The relationships between the parameters of the Eqs (2.5.1) and (2.5.7) have been obtained by Ogilvie through the application of the Fourier transform under a sinusoidal regime [Ogilvie, 1964]:

$$\mathbf{M}_a(\omega) = \mathbf{M}_{a_\infty} - \frac{1}{\omega} \int_0^\infty \mathbf{h}_r(t) \sin(\omega t) dt \quad (2.5.8)$$

$$\mathbf{B}(\omega) = \int_0^\infty \mathbf{h}_r(t) \cos(\omega t) dt \quad (2.5.9)$$

Thus, the infinite frequency added mass is defined as:

$$\mathbf{M}_{a_\infty} = \lim_{\omega \rightarrow \infty} \mathbf{M}_a(\omega) \quad (2.5.10)$$

The impulse response function can also be obtained by Fourier transform. In time-domain it is:

$$\mathbf{h}_r(t) = \frac{2}{\pi} \int_0^\infty \mathbf{B}(\omega) \cos(\omega t) dt \quad (2.5.11)$$

while in frequency-domain:

$$\mathbf{h}_r(j\omega) = \int_0^\infty \mathbf{h}_r(t) e^{-j\omega t} dt = \mathbf{B}(\omega) + j\omega[\mathbf{M}_a(\omega) - \mathbf{M}_{a_\infty}] \quad (2.5.12)$$

The numerical computation of the convolution integral of Eq. (2.5.1) can be really time-consuming; this makes it unsuitable for WECs simulation and for the design of their control systems. For this reason Pérez suggested a performing state-space representation of radiation forces [Pérez and Fossen, 2008]. For each element of the [6x6] matrix $\mathbf{h}_r(t)$, the radiation force $F_r(t)$ can be written through a set of two first-order differential equations. In particular, for a certain entry h_{r_i} of the matrix \mathbf{h}_r and related to the DoF named ν , it is:

$$F_r = \int_0^t h_{r_i}(t - \tau)\dot{\nu}(\tau)d\tau \approx \begin{cases} \dot{\zeta} = A_{rad}\zeta + B_{rad}\dot{\nu} \\ \mu = C_{rad}\zeta \end{cases} \quad (2.5.13)$$

The state-space representation can be obtained through some toolboxes as the one explained in [Smogeli et al., 2005]. Further information concerning the modeling of radiation forces on the ISWEC device can be found in [Raffero, 2014].

To resume, the logical process that leads to accounting for radiation forces and added mass for numerical simulation of the ISWEC is the following:

- The frequency-dependent added mass matrix $\mathbf{A}(\omega)$ and damping matrix $\mathbf{B}(\omega)$ are obtained making use of BEM codes.
- The parameters obtained at the previous step can be directly applied in frequency-domain simulations.
- For time-domain simulations, the impulse response function can be obtained by mean of the Ogilvie's relation of Eq. (2.5.11). The infinite frequency added mass is also needed.
- If the computational cost of the convolution integral calculation is too high, it is possible to use a state-space approximation for the radiation forces as the one in Eq. (2.5.13)

2.5.4 Viscous terms

As told, Eq. (2.5.7) can also be extended with some non-linear terms. In particular, it has to be highlighted how Cummins equation is reliable for the slow and small motions of the floater; this can be a source of weakness especially when devices are designed and controlled to work in resonance condition. It is then common to add a viscous term in order to increase the range of validity of the model and overcome this issue [Penalba et al., 2017]. Also, it is possible to add a viscous term that can represent the damping effect on the floater forward motion; this can be done on the ISWEC, that has a certain freedom on the surge motion because of its slack mooring system [Vissio, 2017].

The viscous damping force on the pitch motion is a quadratic viscous drag term :

$$F_{viscous,\delta} = -\beta\dot{\delta}|\dot{\delta}| \quad (2.5.14)$$

where the β coefficient is identified from experimental data or CFD analysis.

On the surge motion, the action of viscous forces is evaluated according to the drag force from the Morison equation; this is valid under the hypothesis of low forward speed. Its expression is:

$$F_{viscous,x} = -\frac{1}{2}\rho C_d S \dot{x}|\dot{x}| \quad (2.5.15)$$

where:

- ρ is the water density.
- C_d is the drag coefficient, that can be found in literature for many geometries.
- S is the cross section area with respect to the incoming water front direction

2.6 PTO model and constraints

The PTO system is the component of the WEC performing the power conversion. Its input is mechanical, while its output is electrical: it is thus a rotating electric motor, and its torque is directly affecting the oscillations of the gyroscopic frame. As illustrated in Fig. 2.4, the PTO is directly linked to the gyroscopic system shaft. The reactive control law has been designed as made up of a stiffness component proportional to the precession angle ε and a damping component proportional to the speed $\dot{\varepsilon}$:

$$T_{\varepsilon PTO}(t) = -k_{PTO}\varepsilon(t) - c_{PTO}\dot{\varepsilon}(t) \quad (2.6.1)$$

This linear control, where c_{PTO} and k_{PTO} are the parameters, permits to tune both the active and reactive power contributions. The PTO torque has to be inserted in the external forces in Eq. (2.4.48).

Some important issues concerning the PTO are the time delay related to the control unit and the backlash due to the use of a gear box [Raffero, 2014]. The control unit is needed because the PTO torque is related to the behaviour of the system: it has to acquire the system feedback variables, run the control algorithm and generate the signal for the PTO control driver; this is the device which generates the action on the machine. The gear box is a component often used in wave energy, a field characterised by low speed and high torques/forces; the use of such a system in the ISWEC permits to increase the PTO speed and to reduce its torque and power losses. However, the oscillatory nature of waves implies that the PTO action is also characterised by motion inversion. This leads to control issues and impulsive stresses when the torque crosses zero value. The problem seems to be of limited importance for a unique stage gearbox.

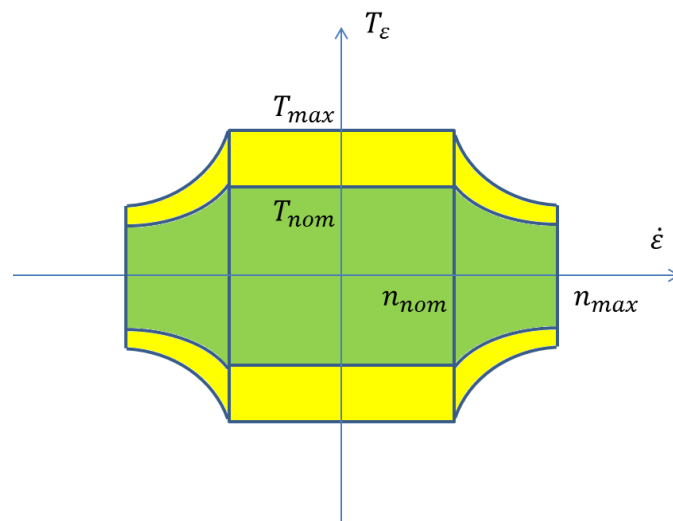


Figure 2.5: PTO working map for the ISWEC device [Raffero, 2014].

The PTO torque and speed have maximum values depending on the size of the system; higher sizes permit to reach better performances, but also increase the investment cost. The working map in Fig. 2.5 shows:

- A green area delimited by the nominal values of torque $T_{\epsilon PTO}$ and angular speed $\dot{\epsilon}$, where the device can work for indefinite time.
- A yellow area, where the PTO system can work in overload for a finite time, provided a certain interval at the end to dissipate the heat generated.

Out of the two delimited areas, the device is at risk of failure. If the PTO speed overcomes the nominal value, the control system reduces the maximum torque and follows the hyperbolic lines, which are constant power working conditions. The values of n_{nom} , T_{nom} , n_{max} and T_{max} are reported in [Vissio, 2017].

2.7 Pitch DoF model

Despite ISWEC captures energy from the pitch motion, the floater is also allowed to move in other hydrodynamic DoFs, heave and surge in particular. The model used in this research project has only one hydrodynamic DoF, the pitch angle δ , while the other hull motions are neglected: the physical model itself is thus an approximation. In reality heave would be uncoupled from the other DoF and would't influence the gyroscopic dynamics; it would only affect the mooring forces. Surge would instead be coupled with pitch: it would have an influence on the gyroscopic motion and the power production. The main approximation with respect to power production when leading with a pitch model is then related to the neglect of surge motion. In addition to pitch, the gyroscopic system is obviously described through the rotation angle about the PTO axis ϵ . Altogether, the model has thus 2-DoF: one for the hull, δ , and one for the gyroscopic system, ϵ .

The overall system of equations can be obtained from the equations presented in Sections 2.4, 2.5 and 2.6. The hydrodynamic linear matrix problem of dimension [6x6] collapses into a scalar one [Vissio, 2017]. In particular, the Cummins equation of Eq. (2.5.7), describing the behaviour of the hull, is completed with the viscous term in Eq. (2.5.14) and the torque exerted from the gyroscopic system on the $y - 1$ axis in Eq. (2.4.54). The second equation of the system is the one governing the gyroscope: it is obtained matching Eq. (2.4.51) for the torque on the precession angle and Eq. (2.6.1) for the torque in the PTO system. The result is reported below:

$$\begin{cases} (I_{eq} + \mu_{\infty})\ddot{\delta} + s_w\dot{\delta} + \int_0^t h(t - \tau)\dot{\delta}(\tau)d\tau + \beta|\dot{\delta}|\dot{\delta} - J_g\dot{\phi}\dot{\epsilon}\cos(\epsilon) - T_w = 0 \\ I_g\ddot{\epsilon} + c_{PTO}\dot{\epsilon} + k_{PTO}\epsilon + J_g\dot{\phi}\dot{\delta}\cos(\epsilon) = 0 \end{cases} \quad (2.7.1)$$

where:

- T_w is the torque induced on the floater by the waves.
- I_{eq} is the momentum of inertia of the device for pitch.
- μ_{∞} is the infinite added mass.

- $\int_0^t h(t - \tau)\dot{\delta}(\tau)d\tau$ is the convolution integral of radiation forces.
- β is a quadratic viscous damping coefficient.
- s_w is the linear hydrostatic stiffness.
- I_g is the overall gyroscope momentum of inertia around the precession. axis, J_g is the flywheel momentum of inertia about its rotating axis.
- c_{PTO} is the PTO damping coefficient and k_{PTO} is the PTO stiffness coefficient.

The two equations are non-linearly coupled by the terms $J_g\dot{\phi}\dot{\epsilon}\cos(\epsilon)$ and $J_g\dot{\phi}\delta\dot{\cos}(\epsilon)$. When the flywheel speed $\dot{\phi}$ goes to zero, the two equations become independent, because the gyroscopic effect is cancelled. The main parameters for controlling and adjusting the ISWEC device are the PTO linear stiffness coefficient k_{PTO} , the linear damping coefficient c_{PTO} and the flywheel speed $\dot{\phi}$. While the first two parameters are actually controlled in real time, wave by wave, the flywheel speed is adapted depending on the sea-state encountered by the ISWEC.

2.8 Simulation frameworks

This last Section tries to give a brief overview on the simulation frameworks available for the ISWEC device. The aim is to highlight the main pros and cons of the main physical models and numerical methods that have been applied to ISWEC, besides providing the sources for further investigation.

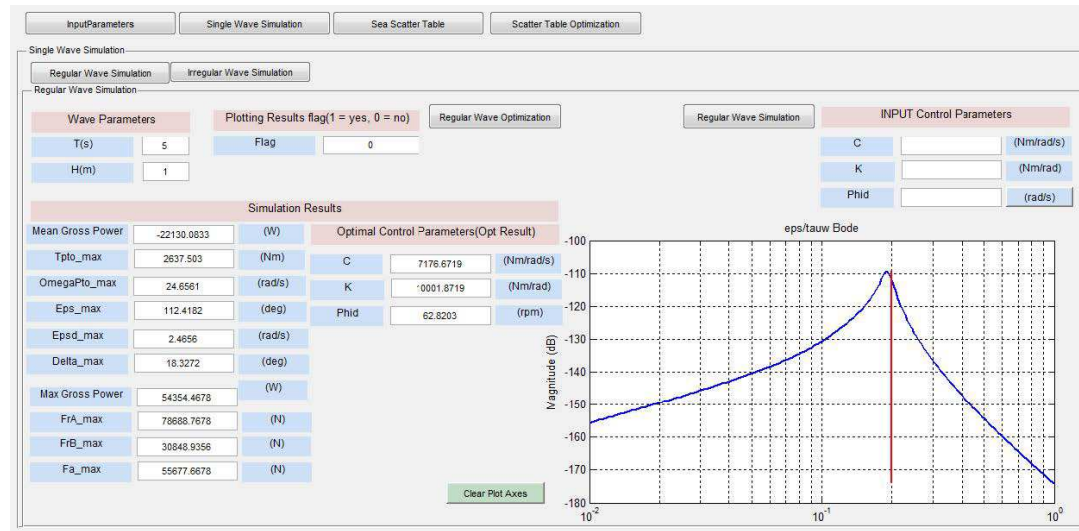
2.8.1 Frequency-domain: ISWEC design tool

The ISWEC design tool has been developed for the master's thesis [Sirigu, 2015], and then presented in [Sirigu et al., 2016]. It makes use of the original Cummins' equation and of the linearised form of the gyroscopic system equations in order to offer a computationally-efficient simulation framework of the whole device. The physical model used in the ISWEC design tool has 2-DoF: the pitch angle for the hull and the precession angle for the gyroscopic system. The possible presence of two gyroscopes is addressed through an equivalent gyroscope. The main aim of the tool is to permit a fast and effective design of the construction and control parameters. The analysis in the frequency-domain leads to a sharp reduction of the computational time, thus permitting to easily explore different device configurations and make an early sizing of components.

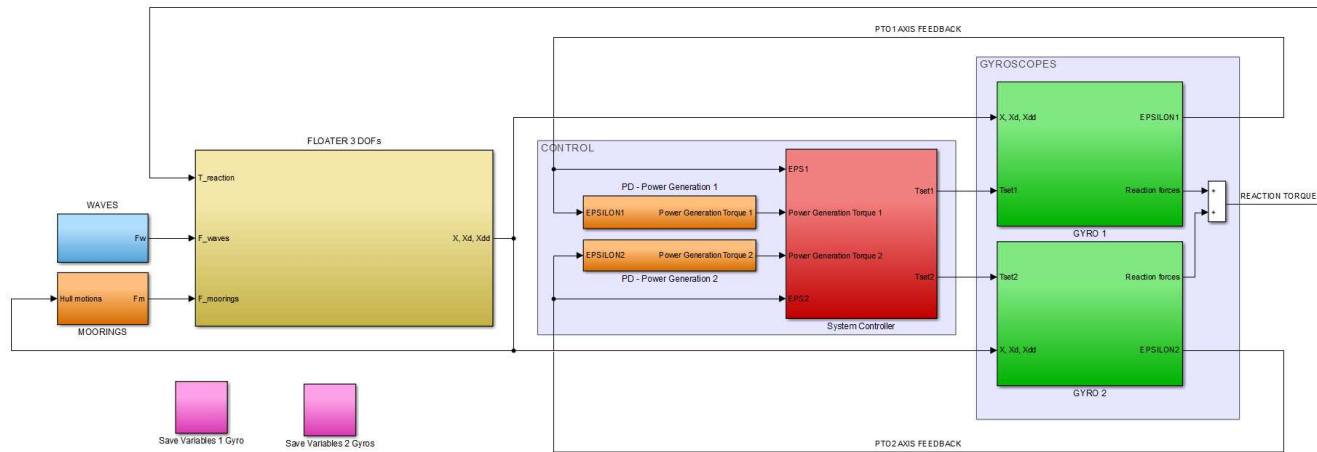
Despite reducing the computational cost, the neglect of non-linearities induces necessarily some errors that increase as long as the input waves become more energetic. The use of appropriate cost-functions permits to take into account the device constraints after the simulations have been performed, penalising those control parameters that lead to overcome the limits imposed. Fig. 2.6a represents a view of the GUI interface that has been developed for the ISWEC design tool.

2.8.2 Time-domain: the Simulink model

Simulink is the environment where the most efforts for the ISWEC numerical modelling have been spent. Several different versions of Simulink model have been developed, depending on the functionalities



(a) $T_e = 8s, H_s = 1.5m$ and $H_s = 2m$



(b) Simulink model - main block diagram [Vissio, 2017].

Figure 2.6: Time-domain simulation frameworks for the ISWEC device

required [Vissio, 2017]. The block model in Fig. 2.6b is the one that has been used, among the other applications, for the ISWEC scatter table fulfillment. The time-domain model is solved through an adaptive algorithm: although a maximum time-step is imposed, the algorithm can change its behaviour while it is running. The eventual presence of two gyroscopes is addressed in different ways depending on the version of the model: both of them can be entirely represented or an equivalent gyroscope can be used. The model has been developed up to 3-DoF on the floater (pitch, surge and heave). The radiation forces are represented through a state-space approximation, as the one described in Subsection 2.5.3. The Simulink model falls in the category of Wave to Wire (W2W) models, able to comprehensively evaluate the power conversion capabilities of the analysed devices.

Let us briefly analyse the blocks in Fig. 2.6b. The first block on the top left, "WAVES", contains the wave loads, that represent the external forces applied to the floater. Beneath it, the block "MOORINGS" contains the mooring forces, modelled through some look-up tables. The yellow block "FLOATER 3 DoF" models the hydrodynamic interactions between waves and hull; its input are the forces from moorings and waves, and the feedback from the internal gyroscopic systems. The green blocks "GYROSCOPES" have as an input the floater kinematics itself and the power production set points from the "CONTROL" blocks. The control blocks permit also to accurately describe the PTO model, accounting for the saturations of torque and angular speed.

2.8.3 Time-domain: Runge-Kutta 2

Overview

A further time-domain simulation framework for the simplified model of Section 2.7 is specifically developed for the research project here presented, using the 2nd order Runge-Kutta method as solving algorithm. The need for such a simulation framework for the ISWEC comes from the necessity of validating the new 2-DoF HB simulation framework that will be presented in Section 3.3 with a model in time-domain having similar characteristics. After a long and careful study, the use of the available Simulink model for such a scope was considered inappropriate because of the computation of radiation forces through the state-space. It would have been inaccurate to validate a model that directly computes the radiation forces through the frequency-dependent damping matrix with a model that introduces an approximation potentially source of significant errors.

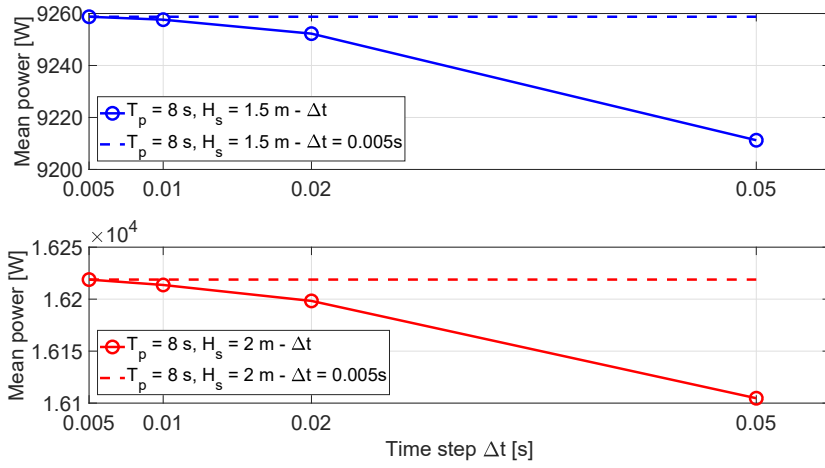
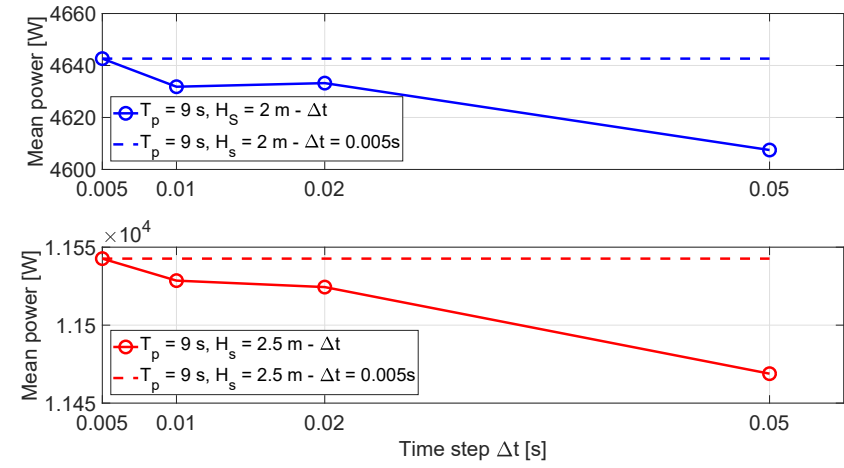
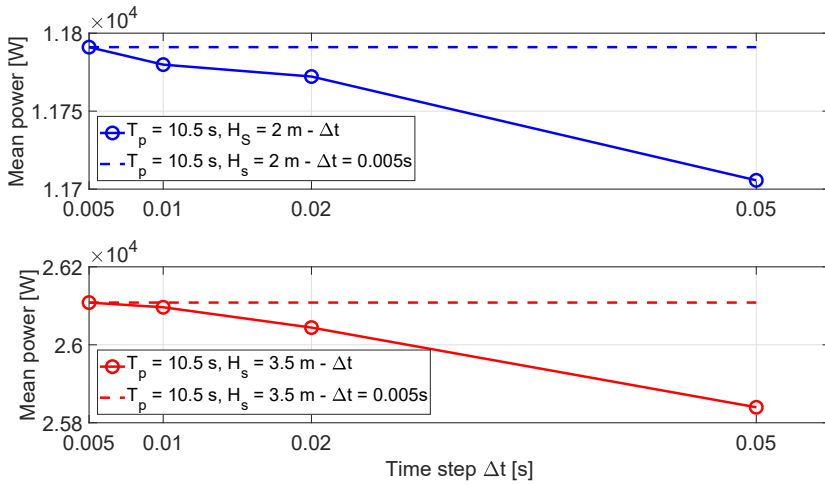
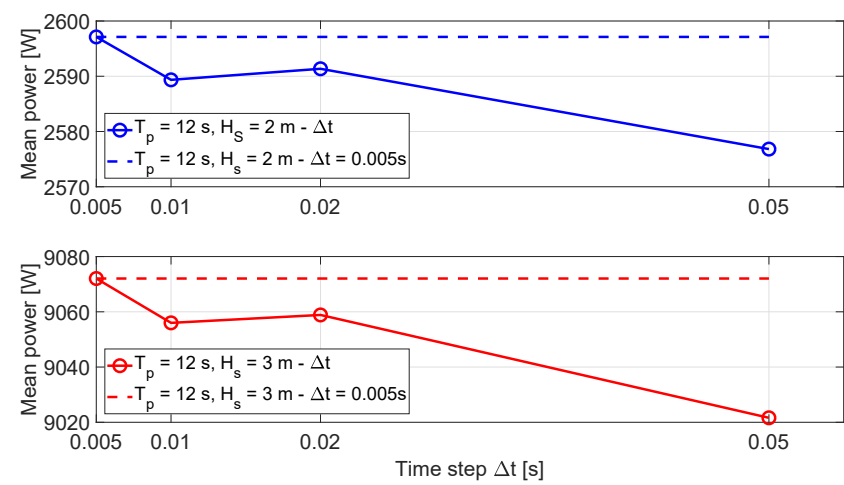
The new time-domain model is based on the system of Eq. (2.7.1); it doesn't provide any control in real-time nor the PTO saturation, and it directly accounts for radiation forces through the computation of the convolution integral. The second order explicit Runge-Kutta method is widely used for ordinary differential equations. It is a one-step method that involves two evaluations of the analysed function at each time interval; it can be seen as an extension of the Euler method, and it is also named *improved Euler method* [Quarteroni et al., 2014].

Convergence study

Once the new time-domain model is built, it is necessary to choose the appropriate time-step to be used for the simulations. A convergence study is here performed for eight representative irregular sea conditions; for the choice of the sea-states and of the control parameters used please refer to Subsection

4.2.1. The aim of this part is merely to highlight the time-step that ensures a good compromise between accuracy and computational time.

Results are presented in Fig. 2.7, in terms of mean output power from the ISWEC device. The time-steps used are ($\Delta t = 0.05s, 0.02s, 0.01s, 0.005s$); the power obtained from the numerical model for every time-step is compared with respect to the most accurate result, i.e. the one with $\Delta t = 0.005s$. Figs. 2.7a and 2.7b are as expected, with the slope of the continuous line decreasing from right to left of the graphs. Figs. 2.7c and 2.7d instead show a strange behaviour: despite the slope has still an overall acceptable trend, the error with respect to $\Delta t = 0.005s$ increases between $\Delta t = 0.02s$ and $\Delta t = 0.01s$. It is difficult to find an explanation for such a result, but it has to be kept in mind that relative differences observed are really small, lower than the 0.5%. Overall, it seems reasonable to assert that a time-step $\Delta t = 0.01s$ ensures good accuracy for all the analysed sea-states.

(a) $T_e = 8$ s, $H_s = 1.5$ m and $H_s = 2$ m(b) $T_e = 9$ s, $H_s = 2$ m and $H_s = 3$ m(c) $T_e = 8$ s, $H_s = 1.5$ m and $H_s = 2$ m(d) $T_e = 8$ s, $H_s = 1.5$ m and $H_s = 2$ mFigure 2.7: Mean absorbed power for different time steps Δt

Harmonic balance simulation framework

The following chapter represents the core of this research work, showing the numerical method used to simulate the ISWEC device. After a brief introduction the method is explained for 1-DoF, referencing to the works already available in literature. Then the method is generalized for a higher number of DoFs and it is finally applied to the ISWEC device, considering its two main degrees of freedom: one for the hull - the pitch angle - and one for the gyroscope system - the rotation about the PTO axis.

The harmonic balance (HB) method solves for the steady-state motion of a non-linear system subject to a periodic excitation signal. Although it operates in the frequency-domain, it ensures the reliable representation of non-linear effects; the harmonic-balance approach is suitable as long as the device follows a smooth trajectory. As outlined in Section 1.2.3, the dynamical equations are projected onto a Fourier basis and the linear terms are separated from the non-linear ones: while the linear terms are expressed in frequency-domain, non-linearities are given as a function of time. The system of equations is solved iteratively by a gradient-based algorithm based on the Newton's method; it makes use of explicit Jacobian calculation, that has the effect of "driving" the numerical algorithm towards the solution.

The HB approach has been widely used in electrical engineering for the simulation of strongly non-linear circuits [Kelley and Mukundan, 1993], [Nastov, 1999]. Concerning marine engineering, it has initially been used in [Spanos et al., 2002] and [Failla et al., 2003] for vibration analysis on offshore structures. The application to WECs comes from [Mérigaud and Ringwood, 2018b], where the method was termed *non-linear frequency-domain approach*. In that occasion the method was validated for two devices with 1-DoF and strong non-linearities:

- A flap-type wave energy converter in presence of quadratic viscous drag.
- A heaving sphere with non-linear restoring force and PTO, non-linear Froude-Krylov forces and quadratic viscous drag.

The approach showed convincing results for 1 DoF WECs, combining computational efficiency with high physical insight. The aim of this chapter is to formalise the HB method for 1-DoF and for multi-DoF devices; the ending section finally presents the HB simulation framework for the 2-DoF model of the ISWEC device.

3.1 The Harmonic Balance method for WECs with 1 DoF

3.1.1 Dynamical equations

The mathematical notes reported refer mainly to [Mérigaud and Ringwood, 2018b] and [Failla et al., 2003]. Let us consider a WEC with only one degree of freedom, on a linear or rotation motion. Let us then call the device displacement and its time derivatives, respectively, x , \dot{x} and \ddot{x} . A linear description of the WEC dynamics can then be performed making use of the Cummins equation [Cummins, 1962]:

$$(\mu + \mu_\infty)\ddot{x} + \int_0^\infty k_{rad}(\tau)\dot{x}(t - \tau)d\tau + s_w x - f_e - f_{PTO} = 0 \quad (3.1.1)$$

where:

- μ is the WEC inertia;
- the radiation forces are presented as the sum of an inertial term $\mu_\infty\ddot{x}$ and a convolution product between the past velocity values and the radiation impulse response function k_{rad} ;
- s_w is the hydrostatic stiffness coefficient;
- f_e is the wave excitation force;
- f_{PTO} is the force exerted by the PTO system on the device.

The Cummins equation describes the WEC motion with linear hydrodynamic interaction; some non-linear effects could be taken into account in the PTO or in the hydrodynamic interaction. Let us write a general non-linear extension of Eq. (3.1.1):

$$\mathcal{L}[x](t) + \mathcal{N}[x](t) - e(t) = 0_{\mathbb{R}} \quad (3.1.2)$$

where \mathcal{L} and \mathcal{N} represent, respectively, linear and non-linear operators, with $\mathcal{L}[x](t) \in \mathbb{R}$ and $\mathcal{N}[x](t) \in \mathbb{R}$; $e(t) \in \mathbb{R}$ is the external excitation, nominally linear wave excitation forces or moments, depending on the considered degree of freedom. The non-linear operator \mathcal{N} is such that:

$$\mathcal{N}[x](t) = g(x(t), \dot{x}(t), \ddot{x}(t)) \quad (3.1.3)$$

and it is thus a memoryless operator for a non-linear function g from $\mathbb{R} \times \mathbb{R} \times \mathbb{R}$ to \mathbb{R} . The linear operator \mathcal{L} can instead be split into a memoryless part \mathcal{L}_{ml} and a linear convolution operator \mathcal{L}_c , such that:

$$\mathcal{L}[x](t) = \mathcal{L}_{ml}[x](t) + \mathcal{L}_c[x](t) \quad (3.1.4)$$

The memoryless linear operator can be expressed as:

$$\mathcal{L}_{ml}[x](t) = m\ddot{x}(t) + c\dot{x}(t) + sx(t) \quad (3.1.5)$$

where $m \in \mathbb{R}$ is the inertia of the whole system, $c \in \mathbb{R}$ is its linear damping and $s \in \mathbb{R}$ is its linear stiffness.

The linear convolution operator \mathcal{L}_c is:

$$\mathcal{L}_c[x](t) = \int_0^\infty k(\tau)\dot{x}(t-\tau)d\tau \quad (3.1.6)$$

where $k \in \mathbb{R}$ is a radiation impulse response function; this term accounts for hydrodynamic radiation forces or moments, and corresponds to the integral in Eq. (3.1.2).

Let us clarify the terms of Eq. (3.1.2) referring to an example reported in [Mérigaud and Ringwood, 2018b], the one of the flap-type WEC with viscous drag term. The device has 1-DoF, the angular position of the flap (pitch angle). It is subject to a vortex shedding effect modelled by a quadratic viscous drag $f_v(\dot{x}) = -c_v\dot{x}|\dot{x}|$ and its PTO can be described as a simple linear damper with $f_{PTO} = -b_{PTO}\dot{x}$. Considering Eqs. (3.1.2) to (3.1.6), their terms with respect to the Cummins equation of Eq. (3.1.1) are:

- The inertial term m contains the inertia of the WEC and the inertial part of radiation forces, thus $m = \mu + \mu_\infty$.
- The linear damping of the system coincides with the one of the PTO, thus $c = b_{PTO}$.
- The linear stiffness s is the hydrostatic stiffness coefficient, thus $s = s_w$.
- The radiation impulse response function k accounts for the convolution product of radiation forces, then $k = k_{rad}$.
- Non-linearities $g(x(t), \dot{x}(t), \ddot{x}(t))$ are contained in the quadratic viscous drag term, then $g(\dot{x}(t)) = c_v\dot{x}|\dot{x}|$.
- The excitation force of waves $e(t)$ is the one on the pitch angle.

The case reported should be understood as an example and nothing more: there are several different types of PTO described by different rules, but especially non-linearities can be present in different terms.

3.1.2 The Harmonic Balance approach

Let us now look for the steady-state solution of Eq. (3.1.2), given that the WEC is excited by a signal $e(t)$ of period T , expressed as a finite sum of harmonic sinusoids:

$$e(t) = \hat{e}_0 + \sum_{k=1}^N \hat{e}_{2k-1} \cos(\omega_k t) + \hat{e}_{2k} \sin(\omega_k t) \quad (3.1.7)$$

where $\forall k \in [1; N]$, $\omega_k = k\omega_1$, $\omega_1 = \frac{2\pi}{T}$, and the amplitudes \hat{e}_{2k-1} and $\hat{e}_{2k} \in \mathbb{R}$ are obtained from the wave spectrum at frequency ω_k ; \hat{e}_0 represents the average value of the excitation. A vector is thus defined such that it identifies the excitation signal in the frequency-domain:

$$\hat{\mathbf{e}} := \begin{pmatrix} \hat{e}_0 \\ \vdots \\ \hat{e}_{2N} \end{pmatrix} \in \mathbb{R}^{2N+1} \quad (3.1.8)$$

The solution given by the harmonic balance method is an approximation, as it takes into account only the first N harmonics of the steady-state motion; the solution can be written as:

$$x(t) \approx \hat{x}_0 + \sum_{k=1}^N \hat{x}_{2k-1} \cos(\omega_k t) + \hat{x}_{2k} \sin(\omega_k t) \quad (3.1.9)$$

or, defining the unknown variables in a vector, we write:

$$\hat{\mathbf{x}} := \begin{pmatrix} \hat{x}_0 \\ \vdots \\ \hat{x}_{2N} \end{pmatrix} \in \mathbb{R}^{2N+1} \quad (3.1.10)$$

The vectors of the derivatives of the steady-state solution are indicated by $\dot{\hat{\mathbf{x}}}$ and $\ddot{\hat{\mathbf{x}}}$ and are obtained as $\dot{\hat{\mathbf{x}}} = \mathbf{\Omega}\hat{\mathbf{x}}$ and $\ddot{\hat{\mathbf{x}}} = \mathbf{\Omega}^2\hat{\mathbf{x}}$, where $\mathbf{\Omega} \in \mathbb{R}^{(2N+1) \times (2N+1)}$ is a block-diagonal matrix:

$$\mathbf{\Omega} = \begin{pmatrix} \mathbf{\Omega}_0 & & 0 \\ & \ddots & \\ 0 & & \mathbf{\Omega}_N \end{pmatrix} \quad (3.1.11)$$

where $\mathbf{\Omega}_0 = 0 \in \mathbb{R}$, and

$$\mathbf{\Omega}_k = \begin{pmatrix} 0 & \omega_k \\ -\omega_k & 0 \end{pmatrix} \mathbb{R}^{2 \times 2}, 1 \leq k \leq N \quad (3.1.12)$$

Thus, we can now introduce the harmonic balance equation rewriting Eq. (3.1.2) into a Fourier basis:

$$\mathbf{A}\hat{\mathbf{x}} + \hat{\mathbf{g}}(\hat{\mathbf{x}}) - \hat{\mathbf{e}} = \mathbf{0}_{\mathbb{R}^{(2N+1)}} \quad (3.1.13)$$

where $\hat{\mathbf{e}}$ and $\hat{\mathbf{x}}$ are defined, respectively, in Eqs. (3.1.8) and (3.1.10), while the other terms can be expressed as follows. The equations of the system defined in Eq. (3.1.13) can't be solved one by one, as the non-linear terms have introduced some interactions among different harmonics; an iterative algorithm is thus needed to find the required solution.

Linear terms

The projection of $\mathcal{L}[x]$ onto a Fourier basis results in the matrix multiplication $\mathbf{A}\hat{\mathbf{x}}$, where $\mathbf{A} \in \mathbb{R}^{(2N+1) \times (2N+1)}$ is a block diagonal matrix. Dividing the memoryless and convolution terms as in Eq. (3.1.4), the linear terms matrix can be rewritten as

$$\mathbf{A} = \mathbf{A}_{ml} + \mathbf{A}_c \quad (3.1.14)$$

The matrix multiplication $\mathbf{A}_{ml}\hat{\mathbf{x}}$ corresponds to the memoryless part \mathcal{L}_{ml} of the linear terms:

$$\mathbf{A}_{ml} = \begin{pmatrix} \mathbf{A}_{ml0} & & 0 \\ & \ddots & \\ 0 & & \mathbf{A}_{mlN} \end{pmatrix} \quad (3.1.15)$$

with $\mathbf{A}_{m/0} = s \in \mathbb{R}$, and

$$\mathbf{A}_{mlk} = \begin{pmatrix} -\omega_k^2 m + s & \omega_k c \\ -\omega_k c & -\omega_k^2 m + s \end{pmatrix} \in \mathbb{R}^{2 \times 2}, k \geq 1 \quad (3.1.16)$$

The matrix multiplication $\mathbf{A}_c \hat{\mathbf{x}}$ corresponds to the convolution integral of \mathcal{L}_c ; using Ogilvie's relation [Ogilvie, 1964], the integral simplifies into a frequency-wise multiplication which involves the frequency-domain representation of the convolution kernel k . The method uses data that are directly obtained from the BEM codes without any approximation of the radiation forces. In particular, introducing the frequency-dependent added mass and damping coefficients, respectively $m_a(\omega)$ and $b(\omega)$, and the infinite-frequency added mass m_∞ , the block-diagonal matrix \mathbf{A}_c can be written as:

$$\mathbf{A}_c = \begin{pmatrix} \mathbf{A}_{c0} & & 0 \\ & \ddots & \\ 0 & & \mathbf{A}_{cN} \end{pmatrix} \quad (3.1.17)$$

with $\mathbf{A}_{c0} = 0 \in \mathbb{R}$, and

$$\mathbf{A}_{ck} = \begin{pmatrix} -\omega_k^2 (m_a(\omega_k) - m_\infty) & \omega_k b(\omega_k) \\ -\omega_k b(\omega_k) & -\omega_k^2 (m_a(\omega_k) - m_\infty) \end{pmatrix} \in \mathbb{R}^{2 \times 2}, k \geq 1 \quad (3.1.18)$$

Non-linear terms

The non-linear terms $\mathcal{N}[x]$ of Eq. (3.1.3) are reported onto a Fourier basis with the vector

$$\hat{\mathbf{g}}(\hat{\mathbf{x}}) := \begin{pmatrix} \hat{g}_0(\hat{\mathbf{x}}) \\ \vdots \\ \hat{g}_{2N}(\hat{\mathbf{x}}) \end{pmatrix} \in \mathbb{R}^{2N+1} \quad (3.1.19)$$

where

$$\begin{aligned} \hat{\mathbf{g}}_0(\hat{\mathbf{x}}) &= \frac{1}{T} \int_0^T g(x(t), \dot{x}(t), \ddot{x}(t)) dt \\ \forall k \in [1, N] \quad \begin{cases} \hat{\mathbf{g}}_{2k-1}(\hat{\mathbf{x}}) &= \frac{2}{T} \int_0^T g(x(t), \dot{x}(t), \ddot{x}(t)) \cos(\omega_k t) dt \\ \hat{\mathbf{g}}_{2k}(\hat{\mathbf{x}}) &= \frac{2}{T} \int_0^T g(x(t), \dot{x}(t), \ddot{x}(t)) \sin(\omega_k t) dt \end{cases} \end{aligned} \quad (3.1.20)$$

while the relationship between $x(t)$ and $\hat{\mathbf{x}}$ is reported in Eq. (3.1.9). In case the non-linear terms are null, the problem simplifies into the usual frequency-domain formulation: $\mathbf{A} \hat{\mathbf{x}} - \hat{\mathbf{e}} = 0_{\mathbb{R}^{(2N+1)}}$. Within the resolution process, the non-linear terms of Eq. (3.1.13) are calculated at each iteration in the time-domain: this requires a tool capable of switching from time-domain to frequency-domain and vice-versa in an effective way. In practice, the integrals of Eq. (3.1.20) are evaluated through numerical integration using a finite number of time steps. If the integer P is the number of points in the analysed time period T , $\forall p \in [1, P]$ it is defined $t_p = p\Delta t$ where $\Delta t = T/P$. The vector of the solution in time-domain can be

written as:

$$\mathbf{x} := \begin{pmatrix} x(t_1) \\ \vdots \\ x(t_P) \end{pmatrix} \in \mathbb{R}^{P \times 1} \quad (3.1.21)$$

and the matrix Φ , which allows passing from the frequency-domain to the time-domain such that $\mathbf{x} = \Phi \hat{\mathbf{x}}$, is defined as:

$$\Phi = \begin{pmatrix} \Phi_1 & \cdots & \Phi_N & \mathbb{1}_{\mathbb{R}^{P \times 1}} \end{pmatrix} \in \mathbb{R}^{P \times (2N+1)} \quad (3.1.22)$$

where

$$\Phi_k = \begin{pmatrix} \cos(t_1 \omega_k) & \sin(t_1 \omega_k) \\ \vdots & \vdots \\ \cos(t_P \omega_k) & \sin(t_P \omega_k) \end{pmatrix} \in \mathbb{R}^{P \times 2}, \forall k \geq 1 \quad (3.1.23)$$

while the matrix for the inverse transformation $\hat{\mathbf{x}} = \Phi^{-1} \mathbf{x}$ can be written as:

$$\Phi^{-1} = \begin{pmatrix} \cos(t_1 \omega_1) & \cdots & \cos(t_P \omega_1) \\ \sin(t_1 \omega_1) & \cdots & \sin(t_P \omega_1) \\ \vdots & \vdots & \vdots \\ \cos(t_1 \omega_N) & \cdots & \cos(t_P \omega_N) \\ \sin(t_1 \omega_N) & \cdots & \sin(t_P \omega_N) \\ 1 & \cdots & 1 \end{pmatrix} \in \mathbb{R}^{(2N+1) \times P} \quad (3.1.24)$$

3.1.3 The solution algorithm

We can rewrite the system of non-linear equations describing the motion of the device in the frequency-domain as:

$$\begin{aligned} (\mathbf{A}_{mI0} + \mathbf{A}_{c0}) \hat{x}_0 + \frac{1}{T} \int_0^T g(x, \dot{x}, \ddot{x}) dt - \hat{e}_0 &= 0 \\ \text{and, } \forall k \in [1, N], & \\ [-\omega_k^2 (m + m_a(\omega_k) - m_\infty) + s] \hat{x}_{2k-1} + [\omega_k (b(\omega_k) + c)] \hat{x}_{2k} + \frac{2}{T} \int_0^T g(x, \dot{x}, \ddot{x}) \cos(\omega_k t) dt - \hat{e}_{2k-1} &= 0 \\ [\omega_k (b(\omega_k) + c)] \hat{x}_{2k-1} + [-\omega_k^2 (m + m_a(\omega_k) - m_\infty) + S] \hat{x}_{2k} + \frac{2}{T} \int_0^T g(x, \dot{x}, \ddot{x}) \sin(\omega_k t) dt - \hat{e}_{2k} &= 0 \end{aligned} \quad (3.1.25)$$

An approximation of the roots of the system of non-linear equations proposed can be solved by making use of the Newton's method [Quarteroni et al., 2014]. It is defined:

$$\mathbf{F}(\hat{\mathbf{x}}) = \mathbf{A} \hat{\mathbf{x}} + \hat{\mathbf{g}}(\hat{\mathbf{x}}) - \hat{\mathbf{e}} \quad (3.1.26)$$

that is the function for which we need to find a root. The method asks for an initial guess reasonably close to the real solution; starting from there, the function is approximated by means of its tangent in the chosen point. The crossing point of the tangent with the x-axis represents a solution more accurate than the initial guess. The process can be iterated until the relative difference between two successive solutions is sufficiently small. At the n -th step, the Newton's method uses the equation

$$\mathbf{F}(\hat{\mathbf{x}}^{(n)}) + \Delta \mathbf{F}(\hat{\mathbf{x}}^{(n)}) (\hat{\mathbf{x}}^{(n+1)} - \hat{\mathbf{x}}^{(n)}) \quad (3.1.27)$$

to determine the $(n+1)$ -th approximation of the root of Eq. (3.1.26). A simple and intuitive representation of the Newton's method for a single variable function is shown in Fig. (3.1)

Let us analyse in more detail the terms of Eq. (3.1.27). The vectors and matrixes of the $(2N + 1) \times 1$ vector $\mathbf{F}(\hat{\mathbf{x}}) = \mathbf{A}\hat{\mathbf{x}} + \hat{\mathbf{g}}(\hat{\mathbf{x}}) - \hat{\mathbf{e}}$ have already been defined previously. Rewriting its entries as in Eq. (3.1.25) we obtain:

$$F_0(\hat{\mathbf{x}}) = (\mathbf{A}_{m10} + \mathbf{A}_{c0})\hat{x}_0 + \frac{1}{T} \int_0^T g(x, \dot{x}, \ddot{x}) dt - \hat{e}_0$$

and, $\forall k \in [1, N]$,

$$F_{2k-1}(\hat{\mathbf{x}}) = [-\omega_k^2(m + m_a(\omega_k) - m_\infty) + s]\hat{x}_{2k-1} + [\omega_k(b(\omega_k) + c)]\hat{x}_{2k} + \frac{2}{T} \int_0^T g(x, \dot{x}, \ddot{x}) \cos(\omega_k t) dt - \hat{e}_{2k-1}$$

$$F_{2k}(\hat{\mathbf{x}}) = [\omega_k(b(\omega_k) + c)]\hat{x}_{2k-1} + [-\omega_k^2(m + m_a(\omega_k) - m_\infty) + m]\hat{x}_{2k} + \frac{2}{T} \int_0^T g(x, \dot{x}, \ddot{x}) \sin(\omega_k t) dt - \hat{e}_{2k}$$
(3.1.28)

The term $\Delta\mathbf{F}(\hat{\mathbf{x}})$ is a $(2N + 1) \times (2N + 1)$ Jacobian matrix whose (k, l) – *th* entry is defined as the partial derivative of the k – *th* harmonic of the objective function with respect to the l – *th* harmonic of the considered motion. Overall, the Jacobian can be written as the sum of a linear term and a non-linear term:

$$\Delta\mathbf{F}(\hat{\mathbf{x}}) = \Delta(\mathbf{A}\hat{\mathbf{x}}) + \Delta\mathbf{g}(\hat{\mathbf{x}}) = \mathbf{A} + \Delta\hat{\mathbf{g}} \quad (3.1.29)$$

where the entries of \mathbf{A} have already been defined, while the term $\Delta\hat{\mathbf{g}}$ is defined as:

$$\Delta\hat{\mathbf{g}} = \Phi^{-1}(\Phi \frac{\partial g}{\partial x} + \Phi\Omega \frac{\partial g}{\partial \dot{x}} + \Phi\Omega^2 \frac{\partial g}{\partial \ddot{x}}) \quad (3.1.30)$$

The overall solving algorithm is described in Fig. 3.2. As mentioned above, Newton's method requires a starting point: this must be sufficiently close to the solution to ensure convergence. This theme will be better analysed later on; for the time being we simply note that the linearised solution of the problem

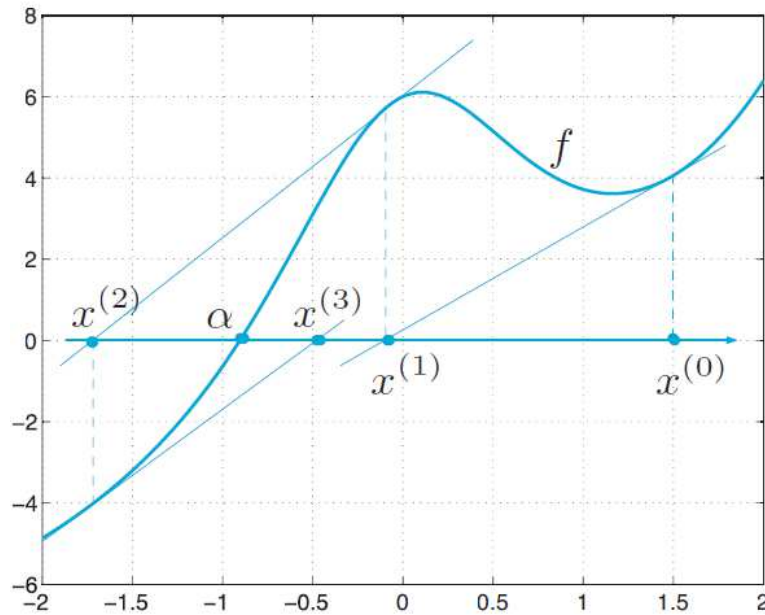


Figure 3.1: The first iterations generated by the Newton's method with initial guess for an exponential function [Quarteroni et al., 2014].

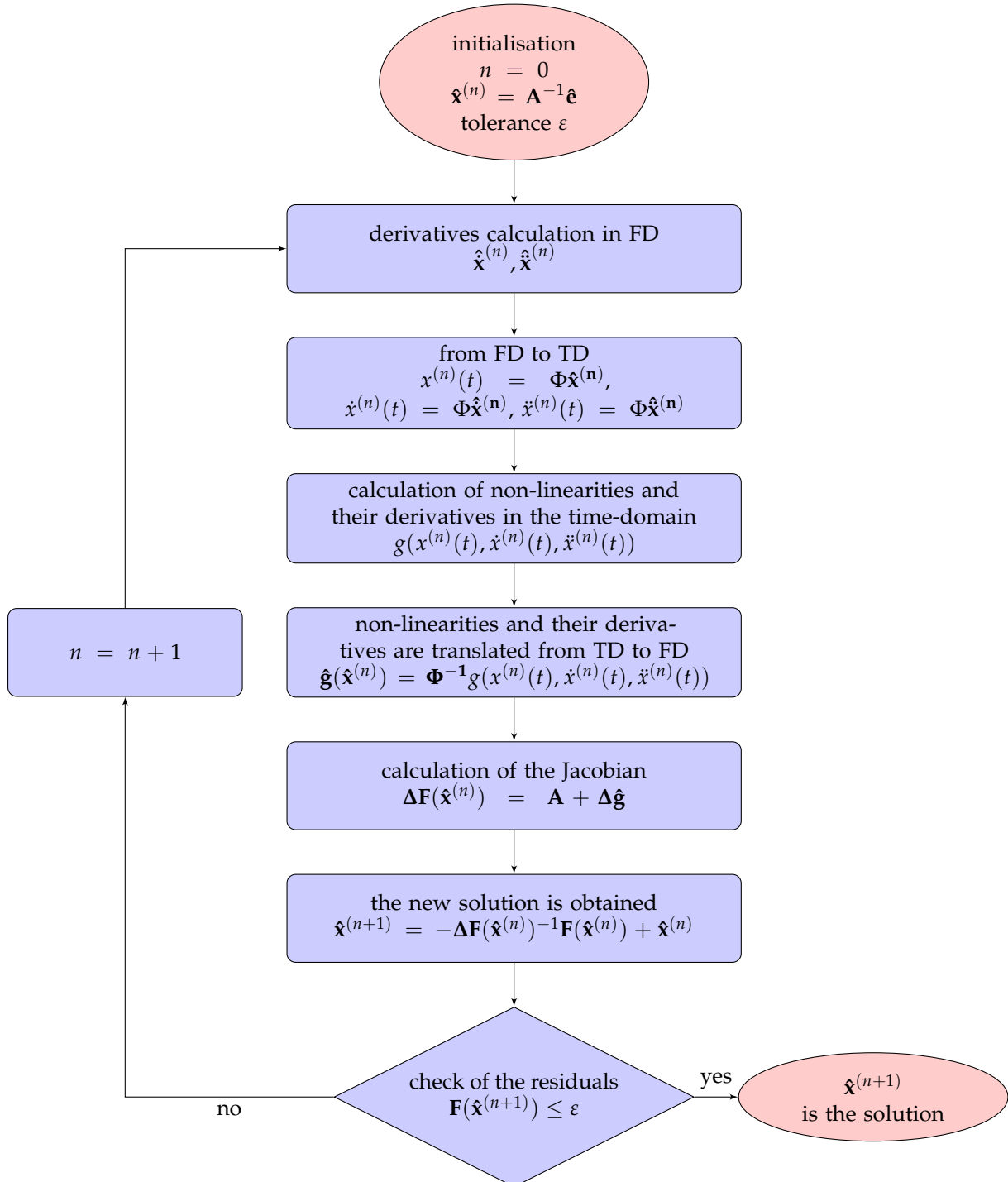


Figure 3.2: Flow diagram of the solving algorithm for Eq. (3.1.13).

can represent an effective starting point for the algorithm [Mérigaud and Ringwood, 2017]. After the initialisation, the first and second derivatives of the current solution are calculated by making use of the matrix reported in Eq. (3.1.11). The transition from the frequency-domain to the time-domain is performed by making use of the matrix in Eq. (3.1.22), applied to the current solution and its derivatives. At this point, non-linear terms - and their derivatives - are simply computed in the time-domain starting from the analytical equation of the WEC motion; they are then taken back to the frequency-domain by making use of the matrix in Eq. (3.1.24). The Jacobian $\Delta\mathbf{F}(\hat{\mathbf{x}})$ in the point identified by the current solution is computed making use of the derivatives calculated at the previous step; the new and more accurate solution is thus computed by Eq. (3.1.27). At this point the solving algorithm has to choose if the solution found is enough accurate, and whether the process should be iterated or not. The check of accuracy is performed through the residual: if the value of $\mathbf{F}(\hat{\mathbf{x}})$ for the new solution is small enough, the procedure is considered completed; otherwise, the whole process is repeated using the last solution found as starting point.

3.2 From one to multiple DoF

Starting from what has been written in the previous section, we propose the mathematical formalisation of the HB method for multi-DoF WEC models. The DoF can be hydrodynamic (heave, sway, surge for linear motion; pitch, roll, yaw for rotation), but not only: many WECs have working mechanisms with one or more internal DoF. The non-linear system describing the overall motion of the device includes an equation for each of its DoF. In case the considered DoF is on the hull, the governing equation is the Cummins' equation reported in Eq. (3.1.1) with the possible addition of one or more non-linear terms. If the DoF is within the mechanisms of the device, the equation can be any linear or non-linear dynamical equation. Moreover, every internal DoF related equation is coupled to the hull equations through some terms that recur in the system: they represent the interaction between the internal motion and the hull, which is in turn excited by incoming waves. The formalisation of the HB method for multi-DoF WEC models is similar to the one-DoF case, and may appear repetitive; however, according to the author's opinion it is important to retrace all the steps in order to ensure complete understanding of the method. Part of the work described in this chapter has been previously published in [Novo et al., 2018].

3.2.1 Dynamical equations for multi-DoF WECs

Let us define the WEC generalised coordinates and their derivatives as \mathbf{x} , $\dot{\mathbf{x}}$, $\ddot{\mathbf{x}}$: they are all vector-valued functions defined on the simulation time interval $[0, T]$ and they take values in \mathbb{R}^D , where D is the number of DoF. It is thus defined the system of equations governing the WEC motion as:

$$\mathcal{L}[\mathbf{x}](t) + \mathcal{N}[\mathbf{x}](t) - \mathbf{e}(t) = 0_{\mathbb{R}^D} \quad (3.2.1)$$

where \mathcal{L} and \mathcal{N} are, respectively, the linear and non-linear operator with $\mathcal{L}[\mathbf{x}](t) \in \mathbb{R}^D$ and $\mathcal{N}[\mathbf{x}](t) \in \mathbb{R}^D$; $\mathbf{e}(t) \in \mathbb{R}^D$ represents the external excitation signal (that is normally null in case of internal DoF). The non-linear operator is such that

$$\mathcal{N}[\mathbf{x}](t) = \mathbf{g}(\mathbf{x}(t), \dot{\mathbf{x}}(t), \ddot{\mathbf{x}}(t)) \quad (3.2.2)$$

for a non-linear function \mathbf{g} from $\mathbb{R}^D \times \mathbb{R}^D \times \mathbb{R}^D$ to \mathbb{R}^D . As for the previous case, the linear operator \mathcal{L} is split into a memoryless part, \mathcal{L}_{ml} , and a causal, linear convolution operator, \mathcal{L}_c , so that:

$$\mathcal{L} = \mathcal{L}_{ml} + \mathcal{L}_c \quad (3.2.3)$$

The memoryless operator can be expressed as:

$$\mathcal{L}_{ml}[\mathbf{x}](t) = \mathbf{M}\ddot{\mathbf{x}}(t) + \mathbf{C}\dot{\mathbf{x}}(t) + \mathbf{S}\mathbf{x}(t) \quad (3.2.4)$$

where $\mathbf{M} \in \mathbb{R}^{D \times D}$ is the inertia matrix of the system, $\mathbf{C} \in \mathbb{R}^{D \times D}$ is its linear damping matrix, and $\mathbf{S} \in \mathbb{R}^{D \times D}$ is its linear stiffness matrix. The entries of matrixes \mathbf{C} and \mathbf{S} could also be null, depending on which terms are non-linearly modelled. The convolution operator, \mathcal{L}_c , is assumed to act on the device velocity only:

$$\mathcal{L}_c[\mathbf{x}](t) = \int_0^\infty \mathbf{K}(\tau)\dot{\mathbf{x}}(t - \tau)d\tau \quad (3.2.5)$$

where $\mathbf{K} \in \mathbb{R}^{D \times D}$ is a causal, matrix-valued impulse-response function. The convolution integral of Eq. (3.2.5) represents the memory terms of the hydrodynamic radiation forces and moments [Cummins, 1962]. Its entries are null for those rows of Eq. (3.2.1) which do not express hydrodynamic interactions, thus for those components of \mathbf{x} which are not hydrodynamic DoFs. The non-zero rows and columns of $\mathbf{K}(\tau)$ form $\mathbf{K}_{rad}(\tau) \in \mathbb{R}^{D_h \times D_h}$, the radiation impulse response kernel of the system, where D_h is the number of hydrodynamic DoF.

3.2.2 The HB approach for multi-DoF WECs

As for the 1-DoF case, let us now consider the steady-state solution of Eq. (3.2.1), given that the WEC is excited by a signal $\mathbf{e}(t)$ of period T , expressed as a finite sum of harmonics sinusoids:

$$\mathbf{e}(t) = \hat{\mathbf{e}}_0 + \sum_{k=1}^N \hat{\mathbf{e}}_{2k-1} \cos(\omega_k t) + \hat{\mathbf{e}}_{2k} \sin(\omega_k t) \quad (3.2.6)$$

where $\forall k \in [1; N], \omega_k = k\omega_1, \omega_1 = \frac{2\pi}{T}$, and the amplitudes $\hat{\mathbf{e}}_{2k-1}$ and $\hat{\mathbf{e}}_{2k} \in \mathbb{R}^D$ are derived from the wave excitation spectrum at frequency ω_k . Define

$$\hat{\mathbf{e}} := \begin{pmatrix} \hat{\mathbf{e}}_0 \\ \vdots \\ \hat{\mathbf{e}}_{2N} \end{pmatrix} \in \mathbb{R}^{(2N+1)D} \quad (3.2.7)$$

The method solves for the first N harmonics of the steady-state solution \mathbf{x} , which can be written as:

$$\mathbf{x}(t) \approx \hat{\mathbf{x}}_0 + \sum_{k=1}^N \hat{\mathbf{x}}_{2k-1} \cos(\omega_k t) + \hat{\mathbf{x}}_{2k} \sin(\omega_k t) \quad (3.2.8)$$

or, defining the unknown variables in a vector, we have:

$$\hat{\mathbf{x}} := \begin{pmatrix} \hat{\mathbf{x}}_0 \\ \vdots \\ \hat{\mathbf{x}}_{2N} \end{pmatrix} \in \mathbb{R}^{(2N+1)D} \quad (3.2.9)$$

where all the variables are in the same column vector, organised in $(2N + 1)$ groups of D elements. The vectors of the solution derivatives are $\dot{\hat{\mathbf{x}}}$ and $\ddot{\hat{\mathbf{x}}}$, obtained as $\dot{\hat{\mathbf{x}}} = \mathbf{\Omega}\hat{\mathbf{x}}$ and $\ddot{\hat{\mathbf{x}}} = \mathbf{\Omega}^2\hat{\mathbf{x}}$. The matrix $\mathbf{\Omega} \in \mathbb{R}^{(2N+1)D \times (2N+1)D}$ is block-diagonal and is obtained as:

$$\mathbf{\Omega} = \begin{pmatrix} \mathbf{\Omega}_0 & & 0 \\ & \ddots & \\ 0 & & \mathbf{\Omega}_N \end{pmatrix} \quad (3.2.10)$$

where $\mathbf{\Omega}_0 = 0_{\mathbb{R}^{D \times D}}$, and

$$\mathbf{\Omega}_k = \begin{pmatrix} 0_{\mathbb{R}^{D \times D}} & \omega_k \mathbb{I}_{\mathbb{R}^{D \times D}} \\ -\omega_k \mathbb{I}_{\mathbb{R}^{D \times D}} & 0_{\mathbb{R}^{D \times D}} \end{pmatrix} \in \mathbb{R}^{2D \times 2D}, k \geq 1 \quad (3.2.11)$$

Projecting 3.2.1 onto a Fourier basis we obtain the harmonic balance equation:

$$\mathbf{A}\hat{\mathbf{x}} + \hat{\mathbf{g}}(\hat{\mathbf{x}}) - \hat{\mathbf{e}} = 0_{\mathbb{R}^{(2N+1)D}} \quad (3.2.12)$$

where $\hat{\mathbf{e}}$ and $\hat{\mathbf{x}}$ are defined, respectively, in Eqs. (3.2.7) and (3.2.9), while the other terms can be expressed as follows.

Linear terms

The projection of $\mathcal{L}[\mathbf{x}]$ onto a Fourier basis results in the matrix multiplication $\mathbf{A}\hat{\mathbf{x}}$, where $\mathbf{A} \in \mathbb{R}^{(2N+1)D \times (2N+1)D}$ is a block diagonal matrix. Separating the memoryless and convolution terms as in Eq. (3.2.3), the linear terms matrix can be rewritten as:

$$\mathbf{A} = \mathbf{A}_{ml} + \mathbf{A}_c \quad (3.2.13)$$

The matrix multiplication $\mathbf{A}_{ml}\hat{\mathbf{x}}$ corresponds to the memoryless part \mathcal{L}_{ml} of the linear terms:

$$\mathbf{A}_{ml} = \begin{pmatrix} \mathbf{A}_{ml0} & & 0 \\ & \ddots & \\ 0 & & \mathbf{A}_{mlN} \end{pmatrix} \quad (3.2.14)$$

with $\mathbf{A}_{ml0} = \mathbf{S} \in \mathbb{R}^{D \times D}$, and

$$\mathbf{A}_{mlk} = \begin{pmatrix} -\omega_k^2 \mathbf{M} + \mathbf{S} & \omega_k \mathbf{C} \\ -\omega_k \mathbf{C} & -\omega_k^2 \mathbf{M} + \mathbf{S} \end{pmatrix} \in \mathbb{R}^{2D \times 2D}, k \geq 1 \quad (3.2.15)$$

The matrix multiplication $\mathbf{A}_c \hat{\mathbf{x}}$ corresponds to the convolution integral of \mathcal{L}_c . Using Ogilvie's relation [Ogilvie, 1964], the integral simplifies into a frequency-wise multiplication which involves the frequency-domain representation of the convolution kernel \mathbf{K} . In particular, introducing the frequency-dependent added mass and damping matrixes, respectively $\mathbf{M}_a(\omega)$ and $\mathbf{B}(\omega)$, and the infinite-frequency added mass matrix \mathbf{M}_∞ , the block-diagonal matrix \mathbf{A}_c can be written as:

$$\mathbf{A}_c = \begin{pmatrix} \mathbf{A}_{c0} & & 0 \\ & \ddots & \\ 0 & & \mathbf{A}_{cN} \end{pmatrix} \quad (3.2.16)$$

with $\mathbf{A}_{c0} = 0_{\mathbb{R}^{D \times D}} \in \mathbb{R}^{D \times D}$, and

$$\mathbf{A}_{ck} = \begin{pmatrix} -\omega_k^2(\mathbf{M}_a(\omega_k) - \mathbf{M}_\infty) & \omega_k \mathbf{B}(\omega_k) \\ -\omega_k \mathbf{B}(\omega_k) & -\omega_k^2(\mathbf{M}_a(\omega_k) - \mathbf{M}_\infty) \end{pmatrix} \in \mathbb{R}^{2D \times 2D}, k \geq 1 \quad (3.2.17)$$

Non-linear terms

The non-linear terms $\mathcal{N}(\mathbf{x})$ of Eq. (3.2.2) are projected onto a Fourier basis with the vector

$$\hat{\mathbf{g}}(\hat{\mathbf{x}}) = \begin{pmatrix} \hat{\mathbf{g}}_0(\hat{\mathbf{x}}) \\ \vdots \\ \hat{\mathbf{g}}_{2N}(\hat{\mathbf{x}}) \end{pmatrix} \in \mathbb{R}^{(2N+1)D} \quad (3.2.18)$$

where

$$\begin{aligned} \hat{\mathbf{g}}_0(\hat{\mathbf{x}}) &= \frac{1}{T} \int_0^T \mathbf{g}(\mathbf{x}(t), \dot{\mathbf{x}}(t), \ddot{\mathbf{x}}(t)) dt \\ \forall k \in [1, N] &\begin{cases} \hat{\mathbf{g}}_{2k-1}(\hat{\mathbf{x}}) = \frac{2}{T} \int_0^T \mathbf{g}(\mathbf{x}(t), \dot{\mathbf{x}}(t), \ddot{\mathbf{x}}(t)) \cos(\omega_k t) dt \\ \hat{\mathbf{g}}_{2k}(\hat{\mathbf{x}}) = \frac{2}{T} \int_0^T \mathbf{g}(\mathbf{x}(t), \dot{\mathbf{x}}(t), \ddot{\mathbf{x}}(t)) \sin(\omega_k t) dt \end{cases} \end{aligned} \quad (3.2.19)$$

and where $\hat{\mathbf{x}}$ and \mathbf{x} are related as in Eq. (3.2.8).

Additional considerations

The resolution process is the same of the 1-DoF case, despite dealing with multiple DoF involves additional difficulty in building the model and requires higher computational cost. The non-linear terms written above are calculated in the time-domain; this requires a matrix Φ for passing from the frequency-domain to the time-domain such that $\mathbf{x} = \Phi \hat{\mathbf{x}}$, and vice-versa. Defined \mathbf{x} as in Eq. (3.2.9) and recalled that P is the number of studied time instants, the new version of the domain-changing matrix $\Phi \in \mathbb{R}^{P \times (2N+1)D}$ has every column of Eq. (3.1.22) repeated D times, so that $\Phi_k \in \mathbb{R}^{P \times 2D}$.

A few words should be spent on the application of the Newton's method to the multi-DoF case. With respect to the 1-DoF case, the vector

$$\mathbf{F}(\hat{\mathbf{x}}) = \mathbf{A} \hat{\mathbf{x}} + \hat{\mathbf{g}}(\hat{\mathbf{x}}) - \hat{\mathbf{e}} \quad (3.2.20)$$

is a $(2N + 1)D \times 1$ column vector defined by the matrixes from Eqs. (3.2.13) to (3.2.19). The Jacobian

matrix $\Delta\mathbf{F}(\hat{\mathbf{x}})$ has dimensions $(2N + 1)D \times (2N + 1)D$ and is still expressed as

$$\Delta\mathbf{F}(\hat{\mathbf{x}}) = \Delta(\mathbf{A}\hat{\mathbf{x}}) + \Delta\mathbf{g}(\hat{\mathbf{x}}) = \mathbf{A} + \Delta\hat{\mathbf{g}} \quad (3.2.21)$$

The Jacobian contains the derivatives of the function $\mathbf{g}(\mathbf{x}(t), \dot{\mathbf{x}}(t), \ddot{\mathbf{x}}(t))$ with respect to all the DoF:

$$\Delta\hat{\mathbf{g}} = \Phi^{-1} \left(\Phi \frac{\partial \mathbf{g}}{\partial \mathbf{x}} + \Phi \Omega \frac{\partial \mathbf{g}}{\partial \dot{\mathbf{x}}} + \Phi \Omega^2 \frac{\partial \mathbf{g}}{\partial \ddot{\mathbf{x}}} \right) \quad (3.2.22)$$

The solving procedure is the same illustrated in Fig. 3.2, where the variable $x(t)$ is substituted with the multi-DoF variable $\mathbf{x}(t)$ and so on with its derivatives and the non-linear terms.

3.3 Harmonic Balance implementation of the ISWEC model

3.3.1 Formulation of the simulation framework

The 2-DoF model presented in Section 2.5 is here implemented with the HB approach. The system of equations (2.7.1) is reported here for convenience:

$$\begin{cases} (I_{eq} + \mu_{\infty})\ddot{\delta} + s_w\delta + \int_0^t h(t - \tau)\dot{\delta}(\tau)d\tau + \beta|\dot{\delta}|\dot{\delta} - J_g\dot{\phi}\dot{\epsilon}\cos(\epsilon) - T_w = 0 \\ I_g\ddot{\epsilon} + c_{PTO}\dot{\epsilon} + k_{PTO}\epsilon + J_g\dot{\phi}\dot{\delta}\cos(\epsilon) = 0 \end{cases} \quad (3.3.1)$$

where:

- T_w is the torque induced on the floater by the waves.
- I_{eq} is the momentum of inertia of the device for pitch.
- μ_{∞} is the infinite added mass.
- $\int_0^t h(t - \tau)\dot{\delta}(\tau)d\tau$ is the convolution integral of radiation forces.
- β is a quadratic viscous damping coefficient.
- s_w is the linear hydrostatic stiffness.
- I_g is the overall gyroscope momentum of inertia around the precession. axis, J_g is the flywheel momentum of inertia about its rotating axis.
- c_{PTO} is the PTO damping coefficient and k_{PTO} is the PTO stiffness coefficient.

The first equation describes the hull motion, while the second is referred to the gyroscopic system. The pitch motion and the gyroscopic dynamics are non-linearly coupled by the $J\dot{\phi}$ terms. Eq. (3.3.1) is in the form of Eqs. (3.2.1) to (3.2.5). The WEC generalised coordinates and their derivatives are:

$$\mathbf{x}(t) = \begin{pmatrix} \delta(t) \\ \epsilon(t) \end{pmatrix}, \dot{\mathbf{x}}(t) = \begin{pmatrix} \dot{\delta}(t) \\ \dot{\epsilon}(t) \end{pmatrix}, \ddot{\mathbf{x}}(t) = \begin{pmatrix} \ddot{\delta}(t) \\ \ddot{\epsilon}(t) \end{pmatrix} \quad (3.3.2)$$

The excitation terms are non-null only for the pitch equation:

$$\mathbf{e}(t) = \begin{pmatrix} T_w(t) \\ 0 \end{pmatrix} \quad (3.3.3)$$

The terms of the memoryless linear operator \mathcal{L}_{ml} of Eq. (3.2.4) are the following:

$$\mathbf{M} = \begin{pmatrix} I_{eq} + \mu_\infty & 0 \\ 0 & I_g \end{pmatrix}, \mathbf{C} = \begin{pmatrix} 0 & 0 \\ 0 & c_{PTO} \end{pmatrix}, \mathbf{S} = \begin{pmatrix} s_w & 0 \\ 0 & k_{PTO} \end{pmatrix} \quad (3.3.4)$$

The linear convolution Kernel of \mathcal{L}_c of Eq. (3.2.5) is non-null only for the hull equation:

$$\mathbf{K}(\tau) = \begin{pmatrix} h(\tau) & 0 \\ 0 & 0 \end{pmatrix} \quad (3.3.5)$$

The non-linear terms of Eq. (3.2.2) are:

$$\mathcal{N}[\mathbf{x}] = \mathbf{g}(\mathbf{x}, \dot{\mathbf{x}}, \ddot{\mathbf{x}}) = \begin{pmatrix} \beta|\dot{\delta}|\dot{\delta} - J_g\dot{\phi}\dot{\epsilon}\cos(\epsilon) \\ J_g\dot{\phi}\dot{\delta}\cos(\epsilon) \end{pmatrix} \quad (3.3.6)$$

It is interesting to highlight that the matrixes of Eqs. (3.3.4) and (3.3.5) are 2×2 diagonal matrixes: this is due to the fact that the coupling between the two equations, i.e. the interaction between the two DoF, is all contained in the non-linear terms.

The transcription of the system of Eq. (3.3.1) into the HB problem of Eq. (3.2.12) requires the projection of the linear terms onto a Fourier basis. The entries of the $(2N + 1)2 \times (2N + 1)2$ matrix \mathbf{A}_{ml} of Eq. (3.2.14) are $\mathbf{A}_{ml0} = S \in \mathbb{R}^{2 \times 2}$ and:

$$\mathbf{A}_{mlk} = \begin{pmatrix} -\omega_k^2(I_{eq} + \mu_\infty) + s_w & 0 & 0 & 0 \\ 0 & -\omega_k^2 I_g + k_{PTO} & 0 & \omega_k c_{PTO} \\ 0 & 0 & -\omega_k^2(I_{eq} + \mu_\infty) + s_w & 0 \\ 0 & -\omega_k c_{PTO} & 0 & -\omega_k^2 I_g \end{pmatrix} \in \mathbb{R}^{4 \times 4}, k \geq 1 \quad (3.3.7)$$

Introducing the frequency-dependent added mass and damping coefficients for the pitch DoF, respectively $m_a(\omega)$ and $b(\omega)$, and the infinite-frequency added mass for the pitch, m_∞ , the entries of the $(2N + 1)2 \times (2N + 1)2$ matrix \mathbf{A}_c of Eq. (3.2.16) are $\mathbf{A}_{c0} = 0_{\mathbb{R}^{2 \times 2}}$ and:

$$\mathbf{A}_{ck} = \begin{pmatrix} -\omega_k^2(m_a(\omega_k) - \mu_\infty) & 0 & \omega_k b(\omega_k) & 0 \\ 0 & 0 & 0 & 0 \\ -\omega_k b(\omega_k) & 0 & -\omega_k^2(m_a(\omega_k) - \mu_\infty) & 0 \\ 0 & 0 & 0 & 0 \end{pmatrix} \in \mathbb{R}^{4 \times 4}, k \geq 1 \quad (3.3.8)$$

The overall matrix $\mathbf{A} = \mathbf{A}_{ml} + \mathbf{A}_c$ can thus be written as:

$$\mathbf{A} = \begin{pmatrix} \mathbf{A}_0 & & 0 \\ & \ddots & \\ 0 & & \mathbf{A}_N \end{pmatrix} \in \mathbb{R}^{(2N+1)2 \times (2N+1)2} \quad (3.3.9)$$

where the first entry is:

$$\mathbf{A}_0 = \begin{pmatrix} s_w & 0 \\ 0 & k_{PTO} \end{pmatrix} \in \mathbb{R}^{2 \times 2} \quad (3.3.10)$$

and the other entries can be written as:

$$\mathbf{A}_k = \begin{pmatrix} \mathbf{A}_k^{11} & \mathbf{A}_k^{12} \\ -\mathbf{A}_k^{12} & \mathbf{A}_k^{11} \end{pmatrix} \in \mathbb{R}^{4 \times 4}, k \geq 1 \quad (3.3.11)$$

with:

$$\begin{aligned} \mathbf{A}_k^{11} &= \begin{pmatrix} -\omega_k^2(I_{eq} + m_a(\omega_k)) + s_w & 0 \\ 0 & -\omega_k^2 I_g + k_{PTO} \end{pmatrix} \\ \mathbf{A}_k^{12} &= \begin{pmatrix} \omega_k b(\omega_k) & 0 \\ 0 & \omega_k c_{PTO} \end{pmatrix} \end{aligned} \quad (3.3.12)$$

The entries of the linear terms matrix have been completely defined. The non-linear terms are directly computed in the time-domain making use of Eq. (3.3.6), and they are translated in the frequency-domain by making use of the matrix Φ described at the end of Section 3.2.

3.3.2 Practical issues

Initialisation

The starting point $\hat{\mathbf{x}}^{(0)}$ of the root finding algorithm is important for the computational performance of the HB method and for the convergence of the algorithm itself. In the case study proposed the solution is found using the ISWEC linearised model; for the 2 considered DoF, the system of equation is:

$$\begin{cases} (I_{eq} + \mu_\infty)\ddot{\delta} + s_w \delta + \int_0^t h(t-\tau)\dot{\delta}(\tau)d\tau - J_g \dot{\phi} \dot{\varepsilon} - T_w = 0 \\ I_g \ddot{\varepsilon} + c_{PTO} \dot{\varepsilon} + k_{PTO} \varepsilon + J_g \dot{\phi} \dot{\delta} = 0 \end{cases} \quad (3.3.13)$$

where the $\cos(\varepsilon)$ terms have been substituted by 1 and the quadratic viscous drag term has been deleted. The starting point is obtained solving the system:

$$\mathbf{A}' \hat{\mathbf{x}}^{(0)} = \hat{\mathbf{e}} \quad (3.3.14)$$

where the matrix \mathbf{A}' expresses the terms of the linearised model of Eq. (3.3.13) in the frequency-domain. The linearised $J_g \dot{\phi}$ terms couple the two equations; the structure of the memoryless linear terms matrix

changes, resulting in the following overall matrix:

$$\mathbf{A}' = \begin{pmatrix} \mathbf{A}'_0 & & 0 \\ & \ddots & \\ 0 & & \mathbf{A}'_N \end{pmatrix} \in \mathbb{R}^{(2N+1)2 \times (2N+1)2} \quad (3.3.15)$$

where the first entry is:

$$\mathbf{A}'_0 = \begin{pmatrix} s_w & 0 \\ 0 & k_{PTO} \end{pmatrix} \in \mathbb{R}^{2 \times 2} \quad (3.3.16)$$

and the other entries can be written as:

$$\mathbf{A}'_k = \begin{pmatrix} \mathbf{A}'_k{}^{11} & \mathbf{A}'_k{}^{12} \\ -\mathbf{A}'_k{}^{12} & \mathbf{A}'_k{}^{11} \end{pmatrix} \in \mathbb{R}^{4 \times 4}, k \geq 1 \quad (3.3.17)$$

with:

$$\begin{aligned} \mathbf{A}'_k{}^{11} &= \begin{pmatrix} -\omega_k^2(I_{eq} + m_a(\omega_k)) + s_w & 0 \\ 0 & -\omega_k^2 I_g + k_{PTO} \end{pmatrix} \\ \mathbf{A}'_k{}^{12} &= \begin{pmatrix} \omega_k b(\omega_k) & -J_g \dot{\phi} \omega_k \\ J_g \dot{\phi} \omega_k & \omega_k c_{PTO} \end{pmatrix} \end{aligned} \quad (3.3.18)$$

The starting point of the solution algorithm for the HB simulation is nothing but the solution we would obtain using the classical frequency-domain approach.

Fundamental frequency and number of harmonics

The transposition of the non-linear terms $\hat{\mathbf{g}}(\hat{\mathbf{x}})$ from the time-domain to the frequency-domain and the computation of their Jacobian $\Delta \hat{\mathbf{g}}$ requires $(2N + 1)D$ fast Fourier transforms. The computational time increases with the problem size in $N^2 \ln(N)$ [Mérigaud and Ringwood, 2018b]. Therefore it is important to carefully choose the frequency-step and the total number of harmonics in order to limit the size of the problem, but ensuring an accurate description of the system dynamics. The fundamental frequency ω_1 is the greatest common divisor of all the frequency components contained in the input signal. It is chosen as:

$$\omega_1 = \frac{2\pi}{T} \quad (3.3.19)$$

where T is the period of the excitation signal. The frequency step is then defined as:

$$\Delta f = \frac{\omega_1}{2\pi} = \frac{1}{T} \quad (3.3.20)$$

If Δf is too small, the computational time of the HB method increases; if it is too big, the spectra of the input and output signal are poorly represented [Mérigaud and Ringwood, 2018b]. The choice of the number N of harmonics is also more complex, depending on the harmonic content of the wave excitation input and the level of non-linearity in the system dynamics. This particular issue will be discussed in detail in Sections 4.1.2 and 4.2.2 on a case-by-case basis. As a general consideration concerning the

number of harmonics and the computational time, the quadratic relationship previously shown implies that many, relatively short simulations should be preferred to long ones.

Sofisticated root-finding algorithms

The Newton's method has been proposed as root-finding algorithm for the HB simulation, but it is possible to use more sophisticated root-finding algorithms that can take advantage of explicit Jacobian computation as well. Despite those algorithms could ask for higher computational time, the greatest advantage lies in ensured convergence and lower condition number of the problem. The algorithm used in the case study proposed is the trust-region one, available in the commercial software MATLAB®. The theory behind it is not simple and is based on the search of a solution through the choice of a direction and a step-length; the choice of the following step is performed through the check of the success of the previous iteration. A complete explication of this and other similar algorithms can be found in [J. E. Dennis and Schnabel, 1996].

Numerical results and validation

This chapter describes the validation process which has been performed for the HB simulation framework of the ISWEC device. First, the validation is proposed for regular waves, with a particular view on the number of harmonics. Then, the irregular waves case is analysed: the required number of harmonics is studied and the issues concerning the algorithm convergence are explained. Finally, a possible solution to overcome convergence issues is proposed.

The validation of the HB simulation framework for the ISWEC device is here performed with respect to a time-domain model that uses a Runge-Kutta (RK) method; the RK method, as explained in Section 2.8.3, does not make any use of state-space approximations, and uses the Kernel response function for the convolution product of radiation forces. In order to have a broad and complete view on the abilities of the HB approach to represent accurately the device dynamics, it is necessary to compare its outputs in a wide range of sea states and with a realistic set of control parameters. The validation is first performed for regular waves, characterised by the presence of a unique frequency in the excitation signal, and then for irregular waves generated through a Jonswap spectrum.

4.1 Regular waves

4.1.1 Sea conditions and control parameters

The ISWEC wave energy converter has been installed for the first time off the coast of Pantelleria Island (TP, Italy). The site somehow represents the design location of the device, and data concerning the occurrence of different sea conditions have been collected. The campaign has been performed between January 2010 and January 2011, and a significant result is the scatter table of Fig. (4.1). It represents the yearly occurrence of the sea states, identified by the significant wave height H_s and the wave energy period T_e . The (H_s, T_e) conditions of the scatter diagram are "converted" into monochromatic wave signals of the type

$$\eta(t) = A \cos\left(\frac{2\pi}{T}t\right) \quad (4.1.1)$$

with period $T = T_e$ and amplitude $H = 2A$ such that the variance of the surface elevation m_0 is the same for polychromatic and monochromatic wave signals: this means finding a regular sea state energetically equivalent to the irregular one. Starting from Eqs. (1.1.52) and (1.1.85), we just find out that:

$$H = \frac{H_s}{\sqrt{2}} \quad (4.1.2)$$

Only the irregular sea states with a credible occurrence have been selected, to avoid calculations with little practical importance. The regular sea states that correspond to the brighter area of Fig. (4.1) are reported in Fig. (4.2).

As explained in Section 2.6, the main control parameters of the ISWEC device are three: the PTO stiffness coefficient k_{PTO} , the PTO damping coefficient c_{PTO} and the flywheel angular speed $\dot{\varphi}$. We're dealing with a simulation problem, thus the linear damping and linear stiffness coefficients are not modified in real time; this would be excluded from the possibilities given by the HB. In order to perform a realistic validation of the HB simulation framework, an appropriate set of parameters for every sea state should then be chosen. The parameters used in this work are those optimised in [Sirigu et al., 2016]: the cost function that has been minimised is based on the mean output power of the device, but takes also into account the physical constraints of the system (maximum PTO power; maximum PTO axis angle and its root mean square; maximum pitch angle and its root mean square; maximum PTO torque and its root mean square; maximum PTO speed). The parameters are given for the irregular sea states; they're

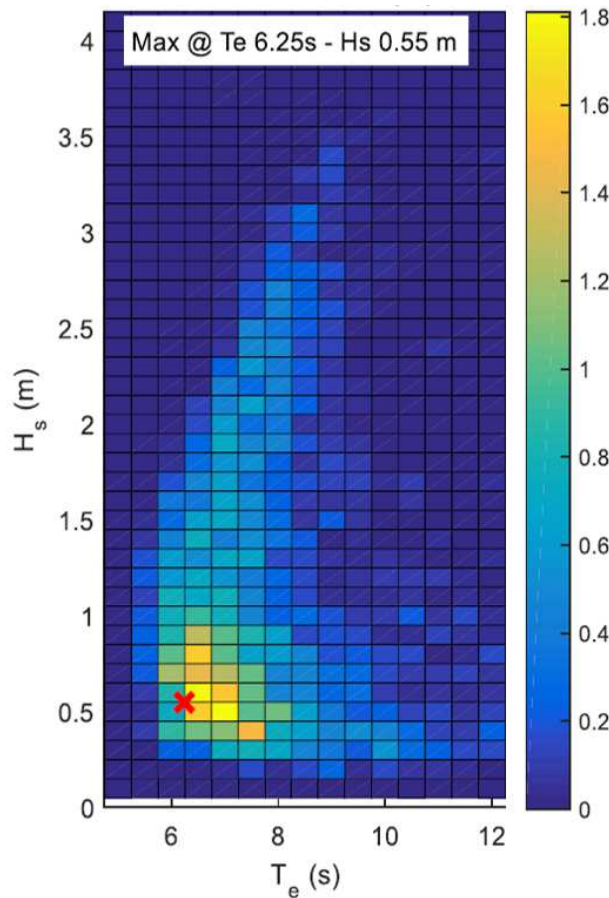


Figure 4.1: Occurrences of sea states off Pantelleria island [Pozzi et al., 2017].

H [m]	2								
	1.5								
	1								
	0.5								
	0.2								
	0.1								
		3	4	5	6	7	8	9	10
		T [s]							

Figure 4.2: Regular sea states energetically equivalent to the brighter area of Fig. (4.1).

translated to the corresponding regular sea states through the simple process previously explained.

4.1.2 Required number of harmonics: convergence study

Before performing the validation of the HB method with respect to the time-domain model, it is necessary to discuss in detail one of the issues mentioned in Section 3.3.2: the number of harmonics to be used for the simulations. This setting has a high importance on the results: as reported in [Nastov, 1999], the accuracy of HB improves exponentially with N . We're dealing with regular waves signals, thus a simulation time equal to the wave period is sufficient to completely describe the WEC motion. Moreover HB solves for the steady-state motion of dynamic systems, and thus any transient is represented. The output of a linear system subjected to a regular wave excitation would just be in the same frequency of the input signal; however, the presence of non-linearities implies that the response also cover other harmonics than the input one.

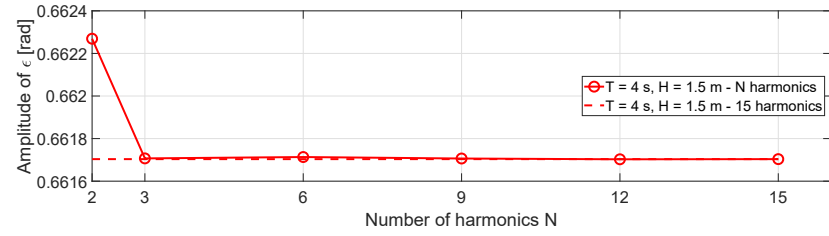
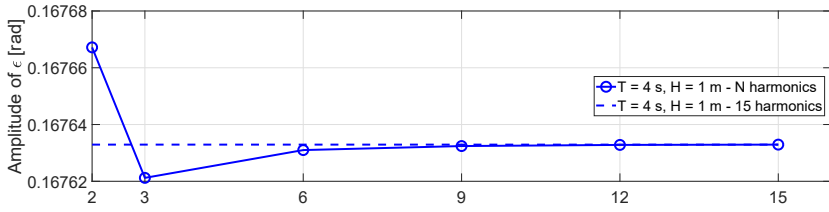
The fundamental frequency ω_1 must then be chosen as in Eq. (3.3.19), where T is just the wave period of the considered sea state. The number N of harmonics should be chosen trying to ensure high accuracy at the cheapest possible computational price. Running the HB method with different number of harmonics ($N = 2, 3, 6, 9, 12, 15$) in all the wave conditions of Fig. 4.1 leads to the following remarks:

- Higher excitation (higher H and lower T) involves more significant non-linear effects, hence requires a higher number of harmonics.
- A number of harmonics $N = 6$ ensures good results in all the cases considered; starting from that point, differences in the results are not anymore perceptible.

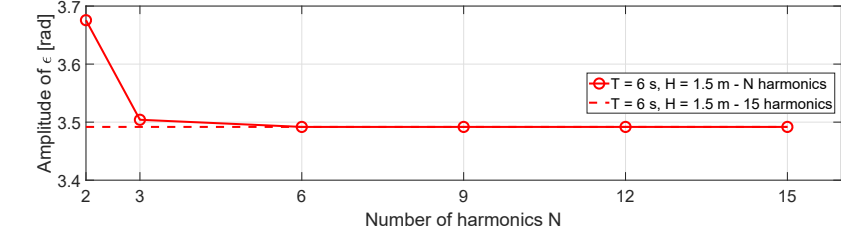
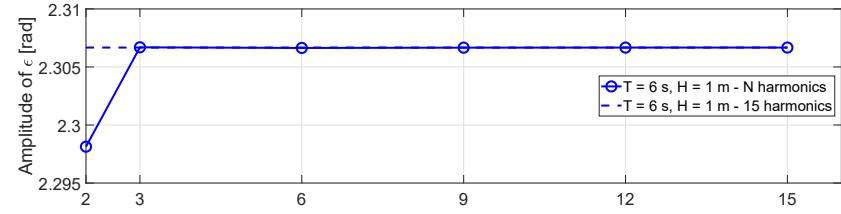
Results are reported for some of the regular sea states in Fig. 4.3, where the convergence study is performed for the rotation angle ε around the PTO axis. The yardstick for the evaluation of the accuracy with the various number of harmonics is the difference between the amplitude of ε for every value assumed by N and the same quantity with the highest number of harmonics available, that is $N = 15$.

4.1.3 Validation results

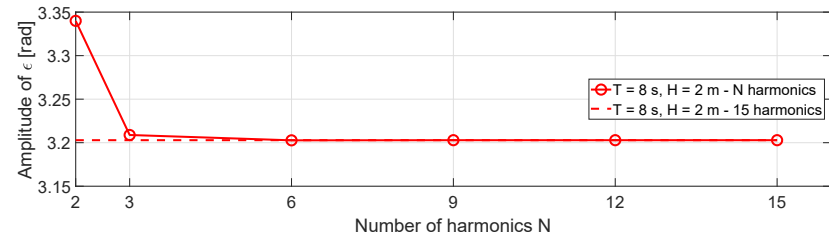
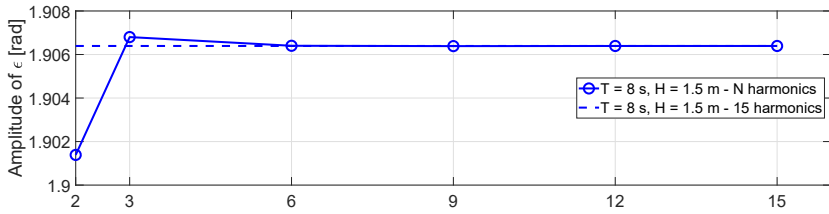
While the convergence on the number of harmonics for the HB has been performed in the previous Subsection, the simulation time-step for the RK2 method has been chosen in Section 2.8.3 in order to ensure inaccuracies lower than 1% with respect to the asymptotic values of ε amplitude. Overall, $N = 6$ (for HB) and $\Delta t = 0.01s$ (for RK2) are retained for comparison between HB and time-domain results. The



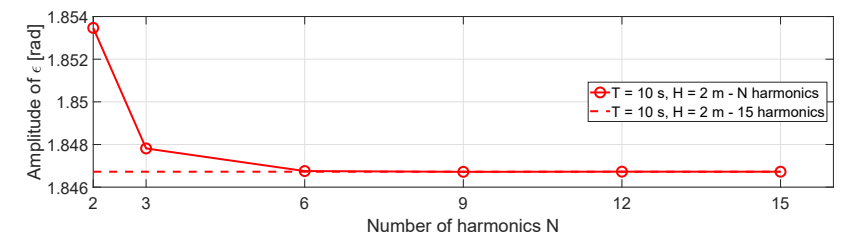
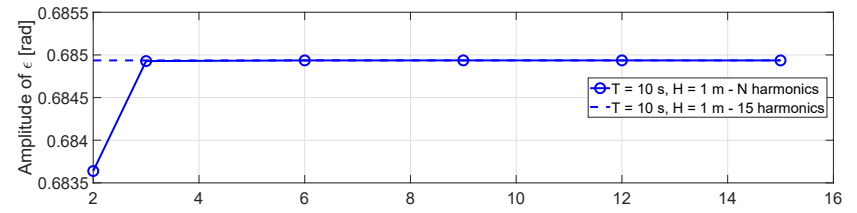
(a) $T = 4s, H = 0.2m$ and $H = 0.5m$



(b) $T = 6s, H = 1m$ and $H = 1.5m$



(c) $T = 8s, H = 1.5m$ and $H = 2m$



(d) $T = 10s, H = 1m$ and $H = 2m$

Figure 4.3: Peak-to-peak trough amplitude of the rotation angle about the PTO axis for different number of harmonics N

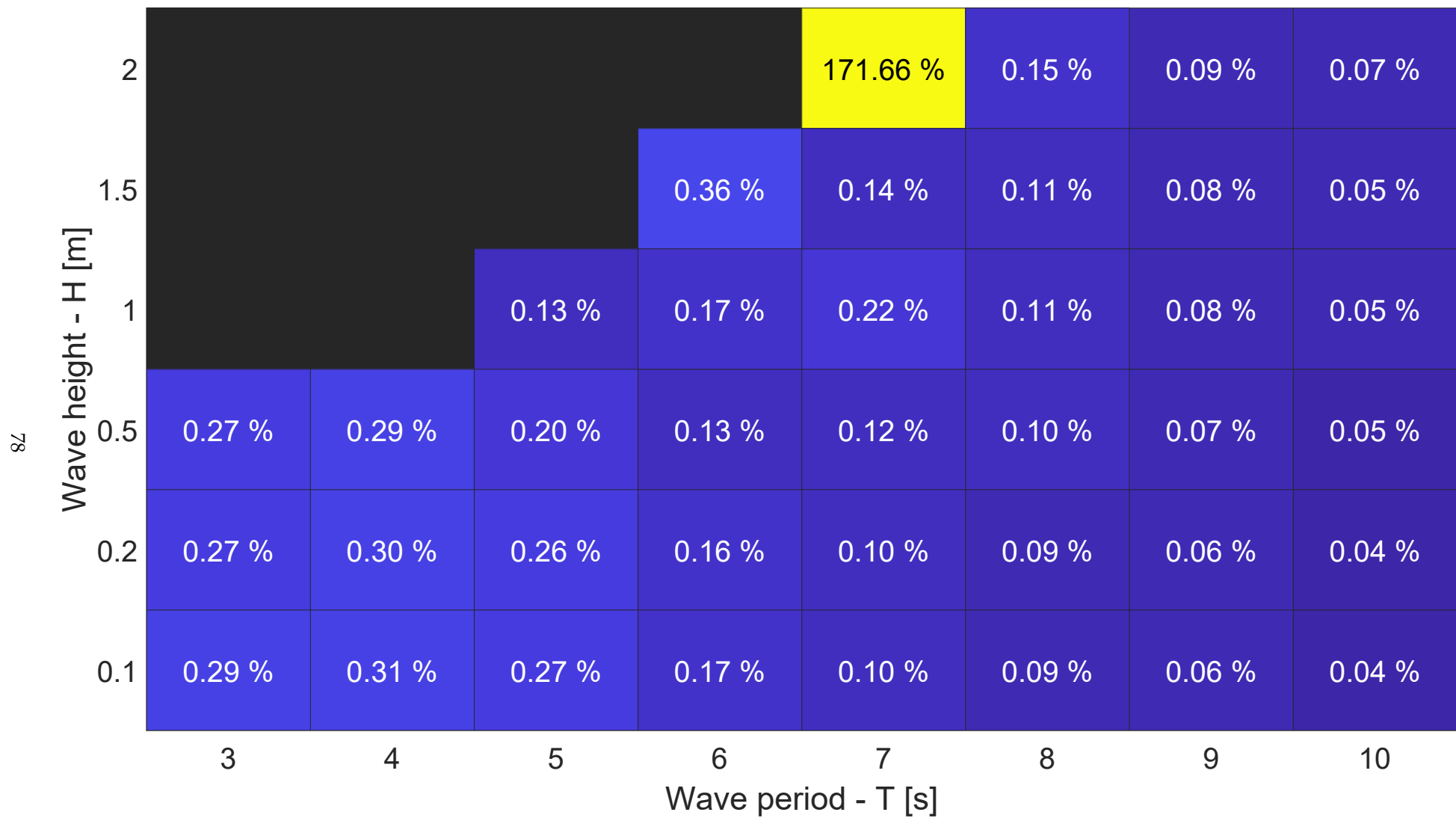


Figure 4.4: $e_{rms}(\%)$ between HB and RK2 solutions for ε , in a range of regular sea states representative of Pantelleria island

distance between the two methods is estimated in terms of root-mean-square difference in % between the two trajectories, given as:

$$e_{rms} = \sqrt{\frac{\int_{t=0}^T (x_{RK2}(t) - x_{HB}(t))^2 dt}{\int_{t=0}^T x_{RK2}^2(t) dt}} \times 100 \quad (4.1.3)$$

where x_{HB} (resp. $x_{RK2}(t)$) is any of the system variables obtained with HB (resp. RK2). For RK2 the steady-state has to be isolated from the transient, because HB solves for the steady-state response. The system variable which has been chosen for being compared is the rotation angle about the PTO axis ε , that is strictly related to the power production.

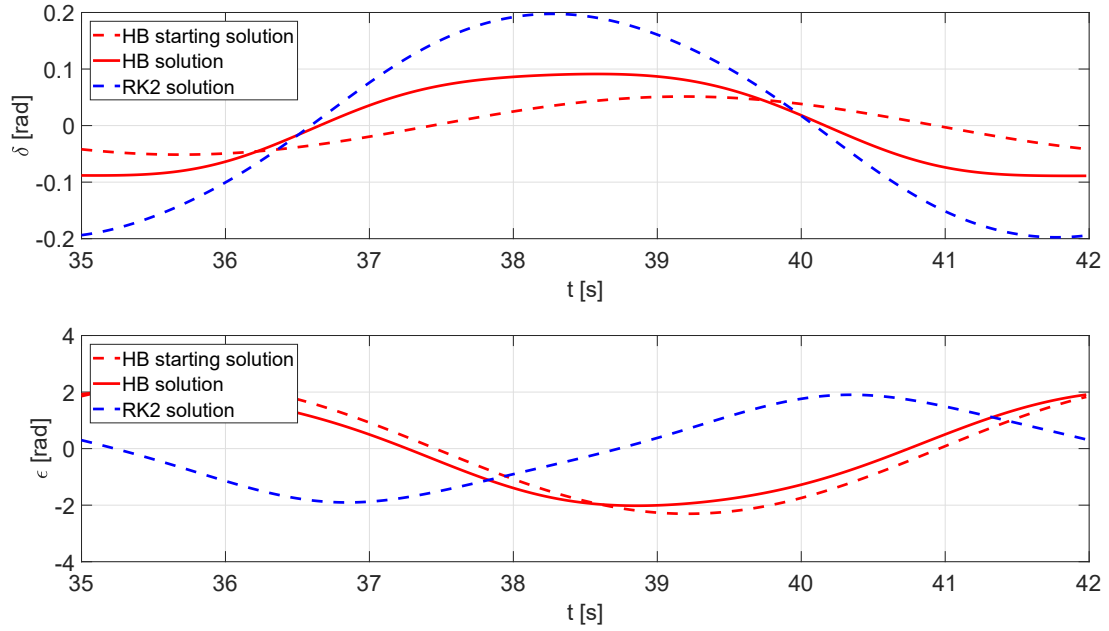
Fig. 4.4 represents the complete validation of HB in the considered set of regular waves conditions. It can be seen that the HB and RK2 results coincide almost everywhere: except for the pair ($T = 7s$, $H = 2m$), the e_{rms} of the ε angle is always lower than 0.4%. Despite differences are really low, almost imperceptible, it is interesting to point out that a general trend is the increase of the e_{rms} with the decrease of the wave period T , that corresponds to an increase in the energy content of waves.

4.1.4 Sensitivity to the algorithm starting point and multiple solutions

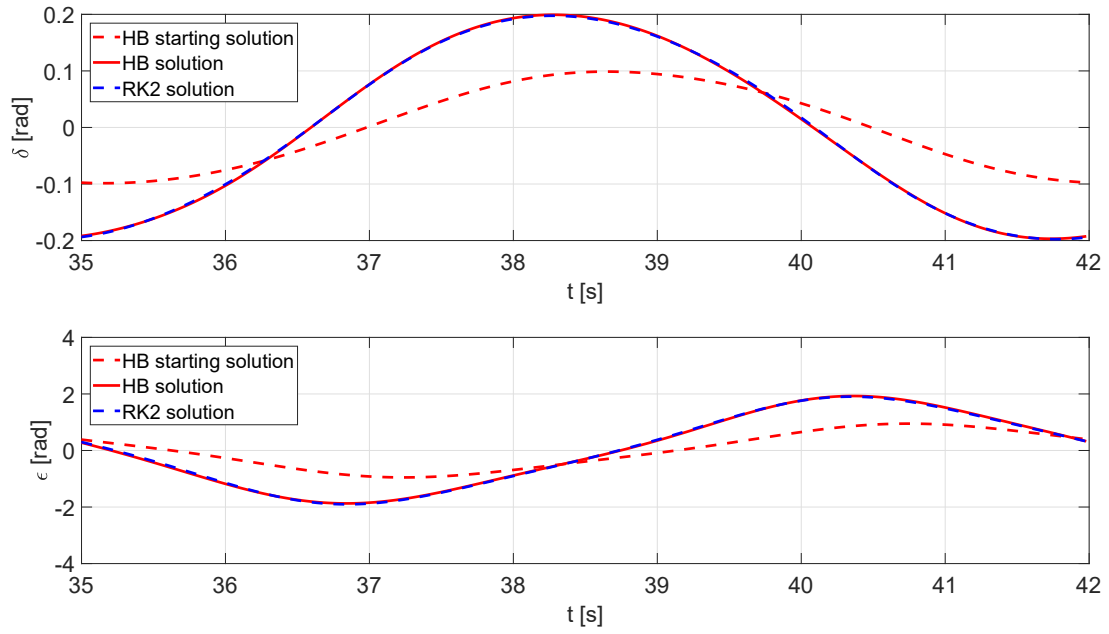
Further investigation is needed for the sea state ($T = 7s$, $H = 2m$). The result showed in Fig. 4.4 is due to the non-convergence of the solving algorithm for that input wave and the corresponding set of control parameters. Though we can't find a solution for a number of harmonics $N = 6$, the algorithm converges for $N \leq 4$. The resulting solution of HB is completely different than that obtained through RK2 (see Fig. 4.5a). In order to shed light on this aspect, another starting solution for HB is investigated: a shifted and scaled version of the RK2 solution is used as starting point \hat{x}^0 for the HB root-finding algorithm. The procedure may seem to the reader a useless trick, but it is extremely useful to understand the link between starting algorithm and convergence. The result obtained is significant, as the algorithm converged to the same solution of the RK2 time-domain integration (see Fig. 4.5b). The results of Fig. 4.5 are interesting and give us important information about the HB method:

- The approximate problem of Eq. 3.2.20 ($Ax+g$) can have multiple solutions, some of which may not have any physical meaning.
- HB results can be sensitive to the starting point of the algorithm.

It is important to realise that we now have to deal with two different problems: the convergence of the algorithm, that can't be ensured but can simply be detected, and the possibility of converging to non-physical solutions. The former issue will be better addressed in Subsection 4.2.4, while for the latter few words are spent here. The possibility for HB to converge to a non-physical solution is related to the approximation given by the finite number of harmonics considered in the problem; a sufficiently high number of harmonics can overcome this issue - despite convergence is not ensured. This clearly represents a limit for the HB method; however, in order to highlight possible solutions without physical significance it is important to compare the output of the given sea state with those of adjacent sea states (e.g. δ and ε amplitudes, net power).

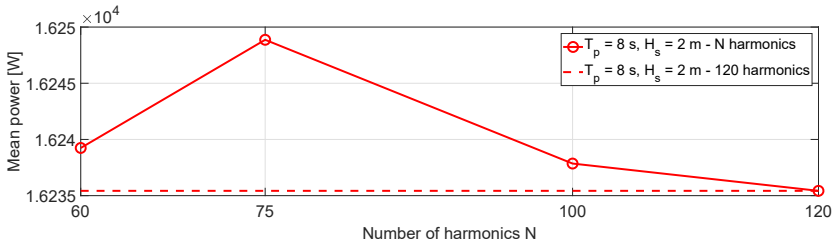
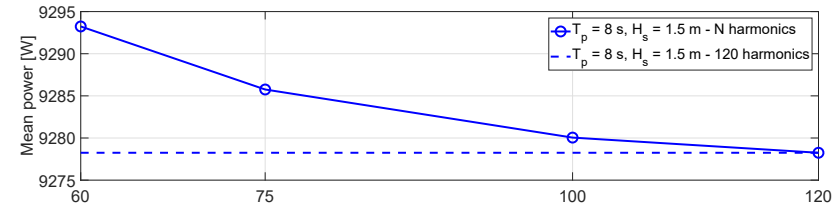


(a) HB starting from the solution of the linearised model.

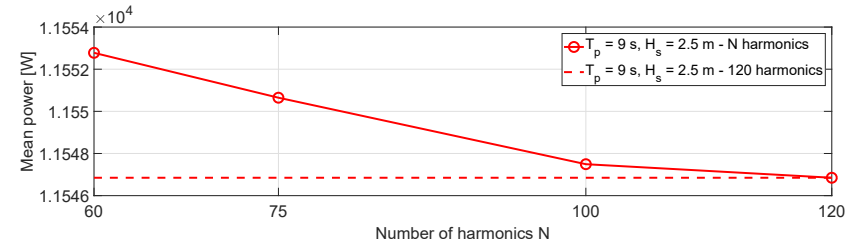
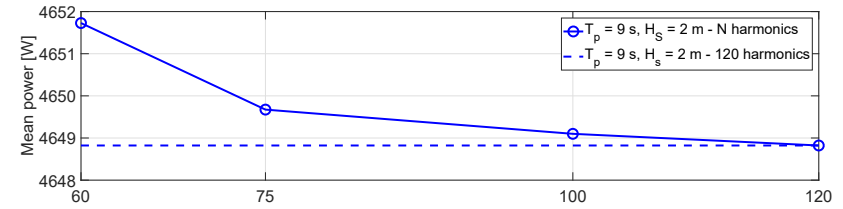


(b) HB starting from an initial solution closer to the RK2 solution.

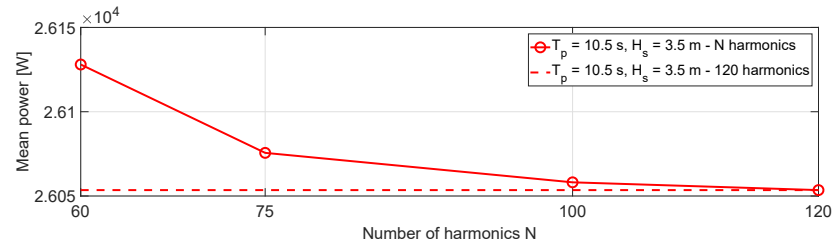
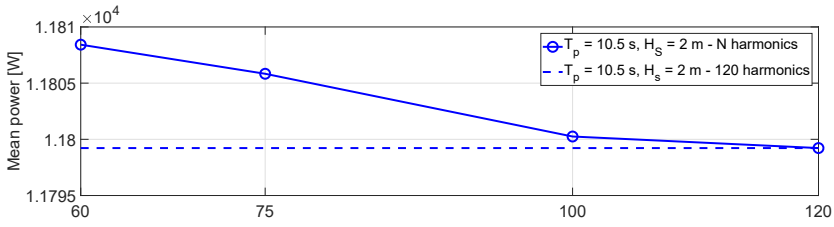
Figure 4.5: $T = 7s$ and $H = 2m$ - comparison between results obtained from RK2 and HB ($N = 4$) from two different initial solutions.



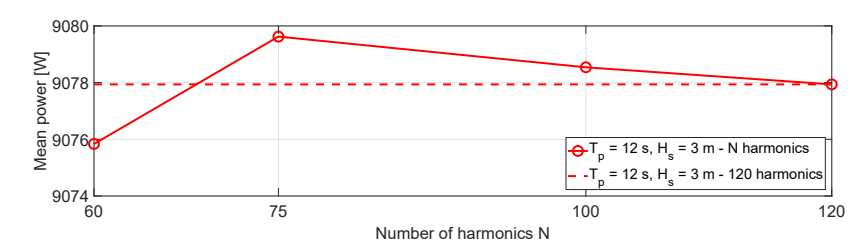
(a) $T_e = 8s, H_s = 1.5m$ and $H_s = 2m$



(b) $T_e = 9s, H_s = 2m$ and $H_s = 2.5m$



(c) $T_e = 10.5s, H_s = 2m$ and $H_s = 3.5m$



(d) $T_e = 12s, H_s = 2m$ and $H_s = 3m$

Figure 4.7: Mean absorbed power for different number of harmonics N

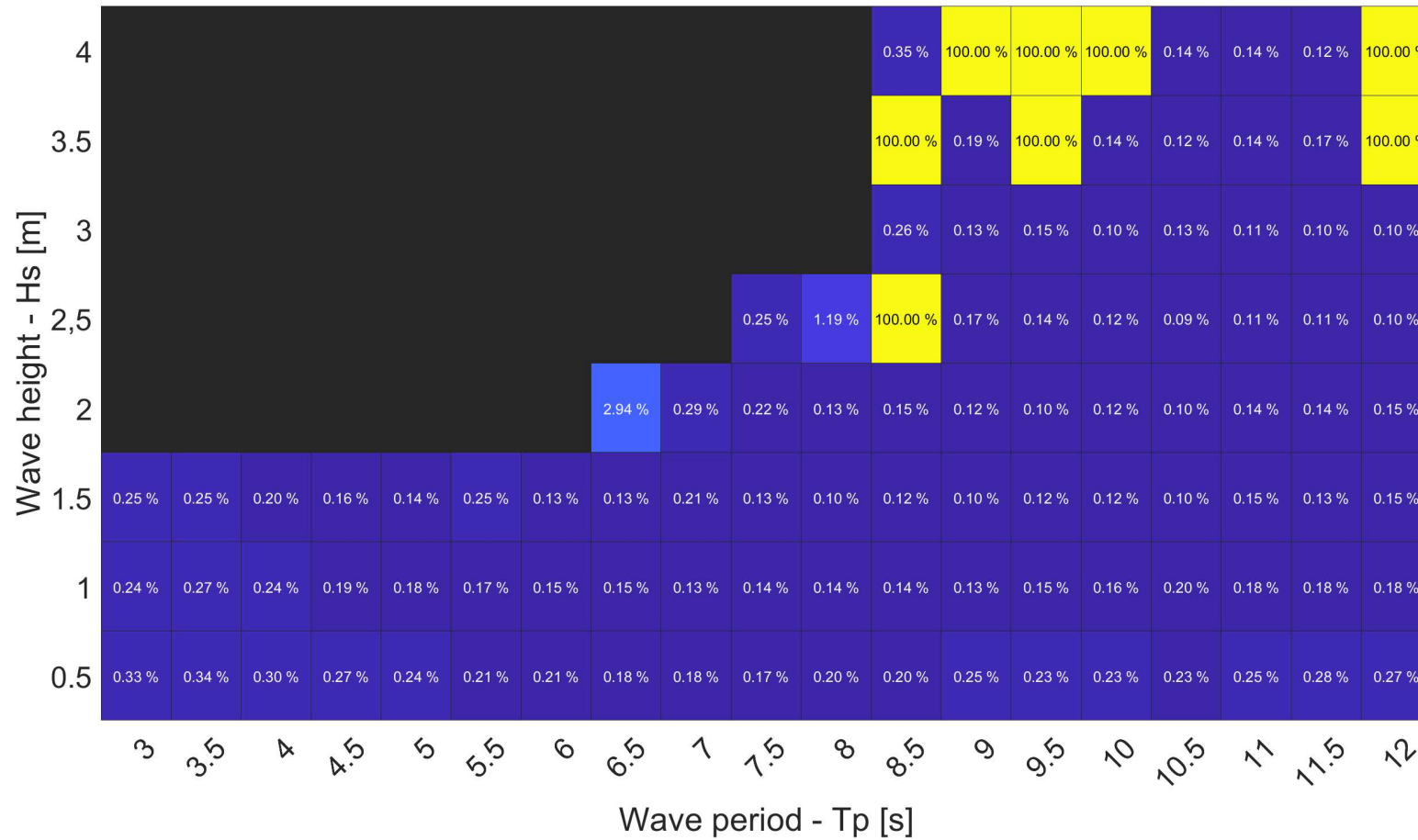


Figure 4.8: $e_{rms}(\%)$ between HB and RK2 solutions for ε , in a range of irregular sea states representative of Pantelleria island. Cells with $e_{rms}(\%)$ equal to 100% are those where the HB algorithm does not converge.

of the HB approach. However, in 10 of the 103 analysed sea-states the algorithm did not converge; those sea-states are in general particularly energetic. It should be reminded that the control parameters, optimised with a linearised model, play an important role in the system dynamics, and thus in the possibility for the algorithm to converge. The sea-states where HB was not able to offer a proper result are analysed in the following Subsection. Otherwise, it seems difficult to find an overall trend in the differences between the HB and the RK2 methods.

4.2.4 Algorithm convergence: ongoing issues and possible solutions

This Subsection aims at analysing the issues related to the sea-states that did not converge; in particular, some solutions will be presented to overcome a problem that could negatively compromise the application of the HB method to WECs. In two cases, namely ($T_p = 6.5s$, $H_s = 2m$) and ($T_p = 8s$, $H_s = 2.5m$), a higher number of harmonics ($N = 120$) has to be used to converge to an accurate solution. The main drawback of this change in the settings of the HB simulations is a substantial increase of the computational time: as explained in Section 3.3.2, the computational time increases with the problem size in $N^2 \ln(N)$. In the 8 sea-states whose cells are coloured in yellow, the increase of the number of harmonics did not lead to convergence of the method.

Since the yellow cells are located in the most energetic part of the scatter table, where non-linearities assume greater importance, it can be deduced that the source of issues lies in the initial solution obtained by the linearised model. It is proposed in Fig. 4.9 a procedure that can enhance the convergence of the algorithm by a more appropriate choice of initial solution.

The above method is illustrated in Fig. 4.10 for the sea state ($T_p = 8.5s$, $H_s = 2.5m$), where it successfully led to the convergence towards a solution really similar to that of RK2. Looking at the

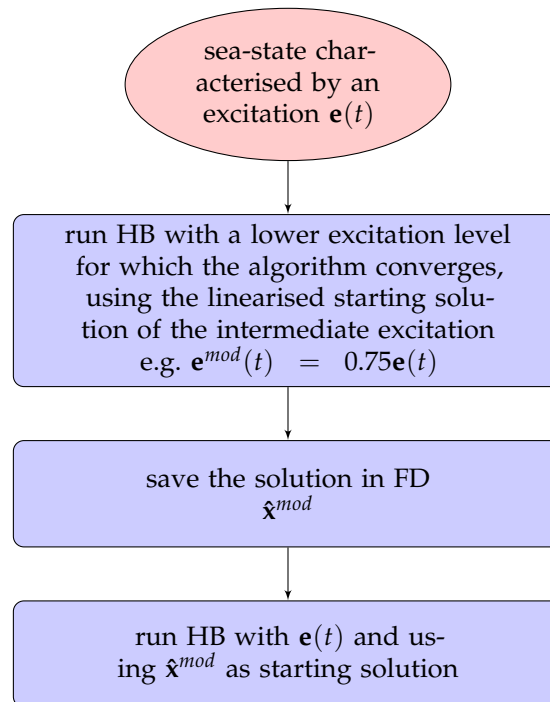


Figure 4.9: Procedure proposed for enhancing the convergence of HB.

results in time, it is observable how a few particularly energetic waves (mainly between $t = 70$ s and $t = 80$ s) make HB not converging with the nominal excitation level; also, observing the black-dashed line, the red line and the blue line, it can be observed how the procedure proposed overcomes the problem dealing with increasingly higher non-linearities. The procedure can also be iterated in order to deal step by step with the most important non-linearities and extend the range of cases where the HB method converges.

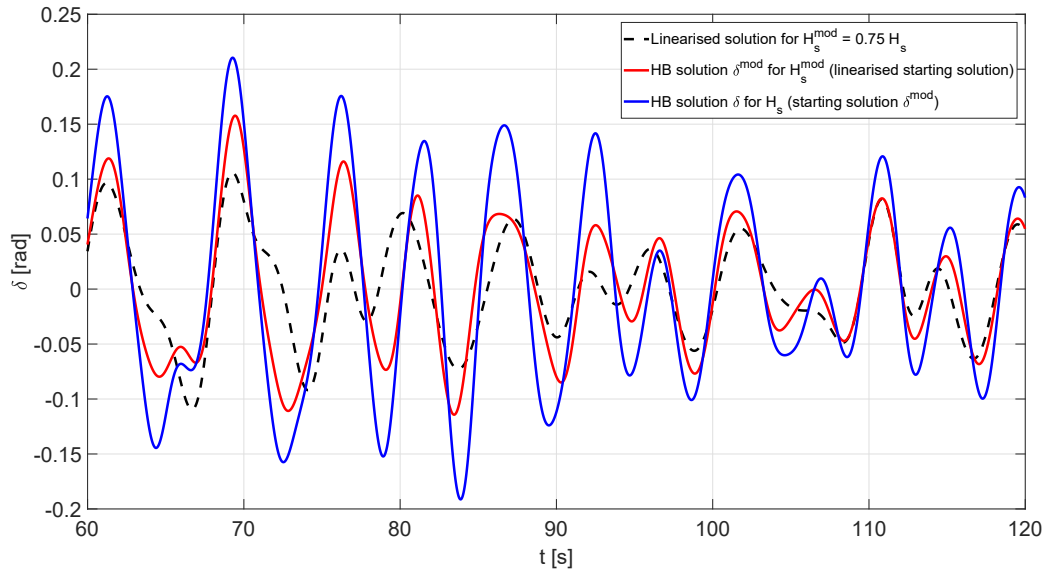


Figure 4.10: ($T_p = 8.5$ s, $H_s = 2.5$ m): linearised solution for $\mathbf{e}^{mod}(t) = 0.75\mathbf{e}(t)$, and HB non-linear solution $\delta^{mod}(t)$; $\delta^{mod}(t)$ is then used as initial solution to obtain $\delta(t)$

The last chapter takes stock of the work done so far. After a brief summary, the dissertation is exposed and explained through what has been acquired in the previous chapters. The main pros and cons of the HB approach are discussed trying to give a comprehensive view of the methodology characteristics. Finally, starting from the work performed and the obstacles encountered, some opportunities for future research work are outlined, together with some recommendations.

Before discussing the conclusions, let us run through the contents of this master's thesis work. The Introduction tried to explain the main reasons and motivations for the research project performed. Chapter 1 contained some fundamental elements for the study of the WECs: it ranged from the formalisation of the theory behind the modelling of sea waves to the state of the art of the technology and the policies for its development. In Chapter 2 it was submitted an analysis of the ISWEC device strictly aimed at the comprehension of the work subsequently described. In Chapter 3 the formalism for HB implementation was exposed trying to follow increasing levels of difficulty: a general 1-DoF WEC, a general multi-DoF WEC and, finally, the 2-DoF model of the ISWEC device. Chapter 4 contained all the acquired numerical results and an analysis of the issues encountered within the work done.

It seems reasonable to argue that the HB approach has proved to be successfully applicable to 2 DoF WECs characterised by strong non-linearities, in particular to the pitch-DoF model of the ISWEC device. However, some problems have been encountered along the study: finding a solid solution to these problems is essential for further development and dissemination of the HB methodology. The following paragraphs will analyse the pros and the cons showed by HB.

5.1 Pros and cons of the HB approach

The numerical results showed the suitability of HB to simulate the behaviour of a 2-DoF WEC with strong non-linearities in regular and irregular waves. Issues related to computation time have not been specifically investigated, as it seemed preferable to focus on convergence issues. However, it is possible to state that HB ensures gains of between one and two orders of magnitude with respect to time-domain

models. Moreover, the exponential convergence towards the exact steady-state solution is a valuable feature of the approach: it allows with little additional effort to significantly increase the accuracy of the results. Furthermore, the method deals finely and effectively with radiation forces, ensuring their accurate description without any particular computational effort.

Finding solutions for the only steady-state motion of a WEC can have advantages and drawbacks depending on the application. It permits to save computation time and avoid the description of the transient, which sometimes can represent a burden in simulations. However, the study of the transient may be deemed necessary if there is an interest in analysing the behaviour of the system under particular conditions, as after a rare and extremely powerful wave. For this reason the steady-state and transient study are both important; HB can be considered an effective solution for the former.

If HB overcomes the limitation of the classical frequency-domain approach for what concerns the description of non-linearities, it still has some limitations. No real-time control can be simulated, and this can be penalising in the context of WECs, often designed to seek resonance condition; this also implies the impossibility of taking into account PTO saturations and other constraints. Moreover, several convergence issues have been encountered along the simulations performed. It has been highlighted the strong sensitivity of the method to the algorithm starting point; in a particular condition the algorithm converged to the real solution either to a solution with no physical meaning depending on the starting condition given as input. The existence of non-physical solution was related to the approximation introduced by the finite number of harmonics in the Fourier basis description; it has been demonstrated that this phenomenon is less likely to happen when a sufficiently high number of harmonics is used. Besides, the irregular waves case showed several powerful sea conditions where the solving algorithm didn't converge at all: in those cases the solution of a *neighbouring problem*, also obtained with HB, can improve the reliability of the method.

5.2 Opportunities and recommendation for future research

According to the author's opinion, the first issue to sort out concerns precisely the convergence of HB in all the possible sea-states and with a large range of control parameters. Some solutions have been proposed here, but they have not been systematically studied in all their nuances and for all the sea-states. In addition, it should be taken into account the scanning of other solving algorithms than those contained in the Matlab *fsolve* function.

Refining the tuning of control parameters might be the main goal of the HB simulation framework developed for the ISWEC device. This would ensure a more accurate representation of non-linear effects in the WEC dynamics, and slightly different values for the optimal parameters are expected to be found. Another relevant application would be carrying a detailed power assessment of the device; the perils of the power matrix approach have already been highlighted in [Mérigaud and Ringwood, 2018a], and the computational efficiency of HB could permit a greater accuracy of the results. It should be remembered that an estimation of power production through the HB simulation framework would need continuous wave signals for the period under study. Interval data would instead introduce some statistical analysis and could not fully exploit the potential of the HB approach. Overall, depending on the required application, one or more DoF could be added to the model; this would represent a challenging target and would require another complete validation process.

Bibliography

- G. B. Airy. Tides and waves. 1841. (Cited at page 4)
- G. Bracco. Iswec: A gyroscopic wave energy converter, 2010. (Cited at page 34)
- B. Count and D. Evans. The influence of projecting sidewalls on the hydrodynamic performance of wave-energy devices. *Journal of Fluid Mechanics*, 145:361–376, 1984. (Cited at page 24)
- W. Cummins. The impulse response function and ship motion. *Schiffstechnik*, (9):101–109, 1962. (Cited at pages 30, 45, 58 e 66)
- J. Davidson, S. Giorgi, and J. Ringwood. Linear parametric hydrodynamic models based on numerical wave tank experiments. *Proceedings EWTEC 2013*, 2013. (Cited at page 32)
- J. Davidson, S. Giorgi, and J. V. Ringwood. Numerical wave tank identification of nonlinear discrete time hydrodynamic models. *Renewable Energies Offshore*, page 279, 2015. (Cited at page 32)
- O. Edenhofer, R. Pichs-Madruga, Y. Sokona, K. Seyboth, S. Kadner, T. Zwickel, P. Eickemeier, G. Hansen, S. Schlömer, C. von Stechow, et al. *Renewable energy sources and climate change mitigation: Special report of the intergovernmental panel on climate change*. Cambridge University Press, 2011. (Cited at page 2)
- European Commission. A roadmap for moving to a competitive low carbon economy in 2050, 2011. (Cited at page 1)
- G. Failla, P. Spanos, and M. Di Paola. Response power spectrum of multi-degree-of-freedom nonlinear systems by a Galerkin technique. *Journal of Applied Mechanics*, 70(5):708–714, 2003. (Cited at pages 57 e 58)
- A. Falcão. Wave energy utilization: A review of the technologies. *Renewable and Sustainable Energy Reviews*, 14(3):899–918, apr 2010. doi: 10.1016/j.rser.2009.11.003. (Cited at pages 2, 20, 22, 24, 25, 26, 27 e 28)
- M. Folley. *Numerical Modelling of Wave Energy Converters*. Academic Press, 2016. (Cited at pages 28, 29, 30, 31 e 32)
- M. Folley and T. Whittaker. Spectral modelling of wave energy converters. *Coastal Engineering*, 57(10): 892–897, 2010. (Cited at pages 31 e 33)

- T. S. Garrison. *Oceanography: an invitation to marine science*. Cengage Learning, 2015. (Cited at pages 3 e 4)
- K. Hasselmann, T. Barnett, E. Bouws, H. Carlson, D. Cartwright, K. Enke, J. Ewing, H. Gienapp, D. Hasselmann, P. Kruseman, et al. Measurements of wind-wave growth and swell decay during the Joint North Sea Wave Project (JONSWAP), 1973. (Cited at page 17)
- J. Henriques, L. Gato, J. Lemos, R. Gomes, and A. Falcão. Peak-power control of a grid-integrated oscillating water column wave energy converter. *Energy*, 109:378–390, 2016. (Cited at page 25)
- B. Holmes. Ocean energy: Development and evaluation protocol—part 1: Wave power. *HMRC—Marine Institute*, pages 1–25, 2003. (Cited at page 36)
- L. H. Holthuijsen. *Waves in oceanic and coastal waters*. Cambridge university press, 2010. (Cited at page 17)
- IEA. *World Energy Outlook 2017*. IEA, nov 2017. doi: 10.1787/weo-2017-en. (Cited at page 1)
- J. J. E. Dennis and R. B. Schnabel. *Numerical Methods for Unconstrained Optimization and Nonlinear Equations*. 1996. (Cited at page 73)
- C. Kelley and L. Mukundan. Convergence analysis for the harmonic balance method. *Nonlinear Analysis: Theory, Methods & Applications*, 20(4):365–380, 1993. (Cited at page 57)
- W. Koo and M.-H. Kim. Nonlinear time-domain simulation of a land-based oscillating water column. *Journal of waterway, port, coastal, and ocean engineering*, 136(5):276–285, 2010. (Cited at page 32)
- H. Krogstad and O. Arntsen. *Linear wave theory*. Norwegian University of Science and Technology, Trondheim, 2000. (Cited at pages 5, 6, 7, 8, 12, 14, 17 e 18)
- L. Letournel, P. Ferrant, A. Babarit, G. Ducrozet, J. C. Harris, M. Benoit, and E. Dombre. Comparison of fully nonlinear and weakly nonlinear potential flow solvers for the study of wave energy converters undergoing large amplitude motions. In *ASME 2014 33rd International Conference on Ocean, Offshore and Arctic Engineering*, pages V09BT09A002–V09BT09A002. American Society of Mechanical Engineers, 2014. (Cited at page 32)
- S. Leyva. The geophile pages, 2000. URL <http://geophile.net>. (Cited at page 3)
- L. Ljung. *System Identification: Theory for the User*. Prentice Hall, 1998. ISBN 978-0136566953. (Cited at page 32)
- P. A. Lynn. *Electricity from wave and tide: An introduction to marine energy*. John Wiley & Sons, 2013. (Cited at pages 20 e 22)
- M. E. McCormick. *Ocean wave energy conversion*. Courier Corporation, 2013. (Cited at page 22)
- D. L. Meadows, E. I. Goldsmith, and P. Meadow. *Limits to growth*, volume 381. CBC, 1972. (Cited at page 22)
- A. Mérigaud and J. V. Ringwood. Non-linear frequency-domain wec simulation: Numerical case studies and practical issues. In *Proceedings of the 11th European Wave and Tidal Energy Conference, Cork, Ireland*, 2017. (Cited at page 65)

- A. Mérigaud and J. V. Ringwood. Power production assessment for wave energy converters: Overcoming the perils of the power matrix. *Proceedings of the Institution of Mechanical Engineers, Part M: Journal of Engineering for the Maritime Environment*, 232(1):50–70, 2018a. (Cited at pages 32 e 87)
- A. Mérigaud and J. V. Ringwood. A nonlinear frequency-domain approach for numerical simulation of wave energy converters. *IEEE Transactions on Sustainable Energy*, 9(1):86–94, 2018b. (Cited at pages 31, 32, 57, 58, 59 e 72)
- G. Mørk, S. Barstow, A. Kabuth, and M. T. Pontes. Assessing the global wave energy potential. In *Proc. of 29th International Conference on Ocean, Offshore and Arctic Engineering, ASME, paper*, volume 20473, 2010. (Cited at pages 19, 20 e 21)
- O. J. Nastov. *Spectral methods for circuit analysis*. PhD thesis, Massachusetts Institute of Technology, 1999. (Cited at pages 57 e 76)
- J. N. Newman. *Marine hydrodynamics*. MIT press, 1977. (Cited at pages 13 e 45)
- R. Novo. A preliminary study about methods for harvesting energy from marine resources, 2015. (Cited at page 20)
- R. Novo, A. Mérigaud, G. Bracco, S. Sirigu, G. Mattiazzo, and J. V. Ringwood. Non-linear simulation of a wave energy converter with multiple degrees of freedom using a harmonic balance method. 2018. (Cited at page 65)
- OEF. Ocean energy strategic roadmap 2016, building ocean energy for europe, 2016. (Cited at page 22)
- OES. Ocean energy systems, annual report 2016, 2016. (Cited at page 23)
- T. Ogilvie. Recent progress toward the understanding and prediction of ship motions. In *Sixth Symposium on Naval Hydrodynamics*, 1964. (Cited at pages 48, 61 e 68)
- OpenLearn. Openlearn, 2018. URL <http://www.open.edu/openlearn/>. (Cited at page 25)
- S. Parmeggiani, J. Kofoed, and E. Friis-Madsen. Experimental study related to the mooring design for the 1.5 MW wave dragon WEC demonstrator at DanWEC. *Energies*, 6(12):1863–1886, apr 2013. doi: 10.3390/en6041863. (Cited at page 28)
- M. Penalba, G. Giorgi, and J. V. Ringwood. Mathematical modelling of wave energy converters: A review of nonlinear approaches. *Renewable and Sustainable Energy Reviews*, 78:1188–1207, oct 2017. doi: 10.1016/j.rser.2016.11.137. (Cited at pages 29, 31, 32 e 49)
- T. Pérez and T. I. Fossen. Time-vs. frequency-domain identification of parametric radiation force models for marine structures at zero speed. *Modeling, Identification and Control*, 29(1):1, 2008. (Cited at pages 44, 45 e 49)
- N. Pozzi, A. Castino, G. Vissio, B. Passione, S. A. Sirigu, G. Bracco, and G. Mattiazzo. Experimental evaluation of different hydrodynamic modelling techniques applied to the iswec. 2017. (Cited at page 75)

- A. Quarteroni, F. Saleri, and P. Gervasio. *Scientific Computing with MATLAB and Octave (Texts in Computational Science and Engineering)*. Springer, 2014. ISBN 978-3-642-45366-3. (Cited at pages 54, 62 e 63)
- M. Rafferò. Design of wave energy converter - a case of applicaiton: Iswec, 2014. (Cited at pages 5, 18, 19, 37, 38, 39, 42, 44, 45, 46, 49 e 50)
- REN21. *Renewables 2017 Global Status Report*. 2017. (Cited at page 23)
- S. A. Sirigu. Iswec: a design tool, 2015. (Cited at page 52)
- S. A. Sirigu, G. Vissio, G. Bracco, E. Giorcelli, B. Passione, M. Rafferò, and G. Mattiazzo. Iswec design tool. *International Journal of Marine Energy*, 15:201–213, 2016. (Cited at pages 52, 75 e 81)
- Ø. Smogeli, T. Perez, T. Fossen, and A. Sørensen. The marine systems simulator state-space model representation for dynamically positioned surface vessels. In *International Maritime Association of the Mediterranean IMAM Conference, Lisbon, Portugal*, 2005. (Cited at page 49)
- P. Spanos, M. Di Paola, and G. Failla. A Galerkin approach for power spectrum determination of nonlinear oscillators. *Meccanica*, 37(1-2):51–65, 2002. (Cited at page 57)
- M. Takao and T. Setoguchi. Air turbines for wave energy conversion. *International Journal of Rotating Machinery*, 2012:1–10, 2012. doi: 10.1155/2012/717398. (Cited at page 26)
- A. Uihlein and D. Magagna. Wave and tidal current energy—a review of the current state of research beyond technology. *Renewable and Sustainable Energy Reviews*, 58:1070–1081, 2016. (Cited at page 1)
- United Nations. Paris agreement, 2015. (Cited at page 1)
- United Nations. World population prospects: The 2017 revision, key findings and advance tables, 2017. (Cited at page 1)
- USACE. *Coastal Engineering Manual*. US Army Corps of Engineers, 2002. (Cited at page 4)
- G. Vissio. Iswec towards the sea, 2017. (Cited at pages 34, 35, 36, 37, 38, 39, 45, 47, 49, 51, 53 e 54)
- R. Waters, M. Stålberg, O. Danielsson, O. Svensson, S. Gustafsson, E. Strömstedt, M. Eriksson, J. Sundberg, and M. Leijon. Experimental results from sea trials of an offshore wave energy system. *Applied Physics Letters*, 90(3):034105, 2007. (Cited at pages 26 e 27)
- Wind Europe. The european offshore wind industry, key trends and statistics 2016, 2017. (Cited at page 1)
- WMO. *Guide to wave analysis and forecasting*. Secretariat of the World Meteorological Organization, 1998. ISBN 92-63-12702-6. (Cited at pages 3, 10 e 14)